SAND2018-13019R

THREE-DIMENSIONAL TRACKING OF HIGH-SPEED TUMBLING PROJECTILES USING STROBOSCOPIC IMAGING

By

Daniel James Bixler

Submitted in Partial Fulfillment
of the Requirements for the

Master of Mechanical Engineering
Specialization in *Explosives Engineering*

New Mexico Institute of Mining and Technology
Department of Mechanical Engineering

Socorro, New Mexico
May, 2019

Sandia National Laboratories is a multimission laboratory managed and operated by National Technology & Engineering Solutions of Sandia, LLC, a wholly owned subsidiary of Honeywell International Inc., for the U.S. Department of Energy's National Nuclear Security Administration under contract DE-NA0003525.

ABSTRACT

Creating images of high-speed projectiles has been a topic of interest for almost a century. Historically, ballistics ranges have used air-gap flash photography or high-speed video cameras to capture this type of data. Air-gap flash photography provides a single image at each camera station. Using modern high-speed imagers provides accurate data but is cost prohibitive for a long-distance range. This paper presents a camera system capable of capturing the three-dimensional data of high speed projectiles over a long distance. The system uses relatively low-cost cameras which are set up in a stereo vision configuration and uses high-speed strobe lights to create multi exposure images. Each pulse of light captures the position of the projectile as it passes the camera. For each position captured in the image, the three-dimensional position of the projectile is found using triangulation geometry. The linear velocity of the projectile is calculated by combining the position of the projectile with timing data. Two test series were conducted. The first test series compares different cameras and backdrops for the camera system. The second test series captured position data for two different shapes of high-speed tumbling projectiles.

Keywords: Stereo Vision, Multi Exposure Image, High Speed Imaging

ACKNOWLEDGEMENTS

I would like to thank Tim Miller for his support and guidance on this project, sharing his knowledge, and providing encouragement along the way. Thanks to Peter Yeh for his mentorship and encouragement, Rus Payne and the staff at the BLT range for letting me use their facility and running the tests, Steve Attaway and Mark Anderson for funding this project, and Chantel Taylor and Jim Schellinger for helping set up the camera stations and for their help during testing. Finally, I'd like to thank my wife Chelsey and daughter Claire for their unwavering support during this project.

Sandia National Laboratories is a multimission laboratory managed and operated by National Technology & Engineering Solutions of Sandia, LLC, a wholly owned subsidiary of Honeywell International Inc., for the U.S. Department of Energy's National Nuclear Security Administration under contract DE-NA0003525.

TABLE OF CONTENTS

Page

LIST OF TABLES v

LIST OF FIGURES vi

LIST OF ABBREVIATIONS AND SYMBOLS x

Chapter 1 Introduction 12

Chapter 2 Previous Work and Literatrure Research 14

- 2.1 Previous Work 14
- 2.2 Imaging Fundamentals 18
- 2.3 Stroboscopic Imaging 23
- 2.4 Stereo Vision Camera System 25

Chapter 3 Experimental Setup 29

- 3.1 Testing Facility 29
- 3.2 Test Series 1 31
  - 3.2.1 Camera Stations and Backdrops 32
  - 3.2.2 Lighting 33
  - 3.2.3 Timing and Triggering 34
  - 3.2.4 Image Acquisition 36
  - 3.2.5 Calibration 36
  - 3.2.6 Projectiles 38
- 3.3 Test Series 2 38
  - 3.3.1 Camera Stations 38
  - 3.3.2 Backdrops 41
  - 3.3.3 Lighting 41
  - 3.3.4 Timing and Triggering 43
  - 3.3.5 Image Acquisition 46
  - 3.3.6 Calibration 47
  - 3.3.7 Camera Station Registration 48
  - 3.3.8 Projectiles 52

Chapter 4 Data Analysis 54

    - 4.1.1 Timing Data 54
    - 4.1.2 Camera Station Registration 56
    - 4.1.3 Image Processing 58
    - 4.1.4 Projectile Tracking 60
- Chapter 5 Results and Discussion 65
  - 5.1 Test Series 1 65
    - 5.1.1 List of Projectiles 65
    - 5.1.2 Camera Selection 67
    - 5.1.3 Backdrop Selection 69
  - 5.2 Test Series 2 74
    - 5.2.1 List of Projectiles 74
    - 5.2.2 Error 75
    - 5.2.3 45° Cylindrical Wedge Results 79
    - 5.2.4 Rectangular Brick Results 83
- Chapter 6 Conclusion and recommendations 90
- REFERENCES 91
- APPENDIX A: Sample python CODE 93
- APPENDIX B: Images from test series 1 95
- APPENDIX C: Images from test series 2 100

LIST OF TABLES

Table Page

Table 1: Test Series 1 Camera Station Configuration 34

Table 2: Test Series 2 Camera Station Configuration 43

Table 3: Test Series 1 List of Projectiles 66

Table 4: Test Series 2 List of Projectiles 74

Table 5: Test Series 2, Shot 27, Cylindrical Wedge Data 82

Table 6: Test Series 2, Shot 34, Rectangular Brick Data 87

Table 7: Test Series 2, Shot 35, Rectangular Brick Data 88

Table 8: Test Series 2, Shot 37, Rectangular Brick Data 89

LIST OF FIGURES

Figure Page

Figure 1: Field of View Diagram 20

Figure 2: Depth of Field Illustration [16] 23

Figure 3: Epipolar Geometry [27] 26

Figure 4: Original Calibration Image 28

Figure 5: Calibration Image in VIC-3D....28

Figure 6: Gun Stand and Chronograph Inside the Firing Range....30

Figure 7: Personnel Facility in BLT 31

Figure 8: Equipment Configuration for Test Series 1 31

Figure 9: Camera Station 1 for Test Series 1 32

Figure 10: Camera Station 2 for Test Series 1 33

Figure 11: Calibration Image Upper Camera....37

Figure 12: Calibration Image Lower Camera 37

Figure 13: Equipment Configuration for Test Series 2 38

Figure 14: Camera Stations Mounted along the BLT 39

Figure 15: Vela One Camera Station....40

Figure 16: Constellation 120E Camera Station....41

Figure 17: Double IR Receiver Mounted to Ceiling 45

Figure 18: Double IR Transmitter Mounted to Floor....45

Figure 19: IR Sensors in BLT Tube 46

Figure 20: Camera Station 1, Upper Camera Calibration....47

Figure 21: Camera Station 1, Lower Camera Calibration 48

Figure 22: DIC Tube Mounted to X-Beam Frame 49
Figure 23: DIC Tube in Front of Camera Station 7..50
Figure 24: DIC Tube Upper Camera View 51
Figure 25: DIC Tube Lower Camera View 51
Figure 26: Ultem Wedge Projectile 52
Figure 27: Ultem Brick in 12 Gauge Shell 53
Figure 28: Speckle Pattern Analysis of DIC Tube 57
Figure 29: Camera Stations in Global Coordinate System 58
Figure 30: Camera Station 1, Lower Camera, Original Data Image 59
Figure 31: Camera Station 1, Lower Camera, Subtracted Image...................................60
Figure 32: Cylindrical Wedge Projectile Markers in VIC-3D 61
Figure 33: Rectangular Brick Projectile Markers in VIC-3D 62
Figure 34: Low Resolution Image Markers in VIC-3D..63
Figure 35: Shot 29 in Spatial Analyzer..64
Figure 36: Camera Station 1, GS3-U3-28S5M-C, Shot 30 68
Figure 37: Camera Station 1, GS3-U3-32S4M-C, Shot 30 68
Figure 38: Camera Station 2, Lower GX-FW-60S6M-C, Shot 30..................................69
Figure 39: Camera Station 2, Upper GX-FW-60S6M-C, Shot 30 69
Figure 40: Camera Station 2, Black Canvas and Reflective Screen................................70
Figure 41: Camera Station 1, Flat Black Canvas Backdrop 71
Figure 42: Camera Station 1, Flat White Canvas Backdrop 73
Figure 43: Camera Station 2, Flat Black and White Canvas Backdrop 73
Figure 44: Image Subtraction, Camera Station 5, Lower Camera 76
Figure 45: Camera Station 7, Correction in XY plane 78

Figure 46: Camera Station 7, Correction in XZ Plane 78

Figure 47: 45° Cylindrical Wedge Velocity Vs. Time 80

Figure 48: 45° Cylindrical Wedge Position X Vs. Time 80

Figure 49: 45° Cylindrical Wedge Position Y Vs. Time 81

Figure 50: 45° Cylindrical Wedge Position Z Vs. Time 81

Figure 51: Rectangular Brick Velocity Vs. Time 85

Figure 52: Rectangular Brick Position X Vs. Time 85

Figure 53: Rectangular Brick Position Y Vs. Time 86

Figure 54: Rectangular Brick Position Z Vs. Time...86

Figure 55: Test Series 1, Camera Station 1, Upper Camera, Copper 0.308 Projectile......96

Figure 56: Test Series 1, Camera Station 1, Lower Camera, Copper 0.308 Projectile 96

Figure 57: Test Series 1, Camera Station 2, Upper Camera, Copper 0.308 Projectile......97

Figure 58: Test Series 1, Camera Station 2, Lower Camera, Copper 0.308 Projectile 97

Figure 59: Test Series 1, Camera Station 1, Upper Camera, Ultem Projectile.................98

Figure 60: Test Series 1, Camera Station 1, Lower Camera, Ultem Projectile 98

Figure 61: Test Series 2, Camera Station 1, Lower Camera, Ultem Projectile 99

Figure 62: Test Series 2, Camera Station 1, Upper Camera, Ultem Projectile.................99

Figure 63: Shot 29, Cylindrical Wedge, Camera Station 1...101

Figure 64: Shot 29, Cylindrical Wedge, Camera Station 2...102

Figure 65: Shot 29, Cylindrical Wedge, Camera Station 3...103

Figure 66: Shot 29, Cylindrical Wedge, Camera Station 4...104

Figure 67: Shot 29, Cylindrical Wedge, Camera Station 5...105

Figure 68: Shot 29, Cylindrical Wedge, Camera Station 6...106

Figure 69: Shot 29, Cylindrical Wedge, Camera Station 7...107

Figure 70: Shot 33, Rectangular Wedge, Camera Station 1 108

Figure 71: Shot 33, Rectangular Wedge, Camera Station 2 109

Figure 72: Shot 33, Rectangular Wedge, Camera Station 3 110

Figure 73: Shot 33, Rectangular Wedge, Camera Station 4 111

Figure 74: Shot 33, Rectangular Wedge, Camera Station 5 112

Figure 75: Shot 33, Rectangular Wedge, Camera Station 6 113

Figure 76: Shot 33, Rectangular Wedge, Camera Station 7 114

LIST OF ABBREVIATIONS AND SYMBOLS

3D	Three-Dimensional
AEF	Aerodynamics Experimental Facility
APR	Aerophysics Range
ARL	Army Research Laboratory
BLT	Ballistic Launch Tube
BRL	Ballistic Research Laboratory
CFA	Color Filter Array
COB	Computer on Board
DIC	Digital Image Correlation
DOF	Degree of Freedom
FOV	Field of View
HBR	Hyperballistics Range
PBR	Pressurized Ballistics Range
POF	Plane of Focus
QE	Quantum Efficiency
SDK	Software Development Kit
TEF	Transonic Experimental Facility
TM	Telemetry

NOTE: APPROVAL PAGE WILL NEED TO BE MANUALLY INSERTED HERE

CHAPTER 1 INTRODUCTION

Creating images that capture the high-speed motion of projectiles for analysis has been studied beginning early in the 20th Century [1]. These studies mainly focus on munitions, but the trajectory of an explosively driven fragment is of interest for both military applications as well as safety applications for the civilian sector. Currently, fragment trajectory modeling assumes an average drag coefficient based on the geometry of the fragment [2]; however, the drag depends on the fragment's orientation in flight. For example, a flat square plate fragment that rotates about the axis perpendicular to the square will have a small average drag coefficient. Conversely, the same fragment rotating about an axis that is planar to the square will experience a higher average drag coefficient.

To more accurately model these fragments, a 6 Degree of Freedom (6 DOF) solver has been developed at Sandia National Laboratories to model a fragment's trajectory based on its orientation. The 6 DOF solver uses hydrodynamic modeling software to find the forces on the fragment based on the geometry and orientation, the roll, pitch, and yaw, of the fragment. The initial velocity and orientation of the fragment are input into the solver, and the solver models the trajectory of the fragment. Some fragments that settle into an aerodynamically ideal orientation will experience low drag coefficients and will tumble in a similar manner to a Frisbee. Thus, these fragments will fly farther than the average in this model. Alternatively, fragments that end up tumbling in non-ideal orientations will have much higher drag coefficients and therefore travel less distance than the average.

To validate the results from the 6 DOF software, experimental data is needed for comparison. The use of high-speed video cameras could capture the trajectory of the projectile. Images of the projectile over a long distance would be needed to validate the model, which would mean the use of high-speed imagers would be cost prohibitive. The goal of this research was to develop a low-cost camera system and processing methods that can be used to capture three-dimensional position data of tumbling projectiles. Since data is needed over a long distance, multiple camera systems will be needed along the length of the test range and integrated with each other to create a global time system and a global coordinate system.

CHAPTER 2 PREVIOUS WORK AND LITERATRURE RESEARCH

2.1 Previous Work

Ballistic ranges have been in use since the late 1910s to find the forces acting on projectiles. The first experiments were done using yaw-cards to find the yaw, the angle between the axis of the shell and the direction of motion of its center of gravity, of 3-inch shells from a rifled gun. These experiments were carried out by Fowler et al at a range in the United Kingdom. The range was less than 600 feet in length, and the yaw cards were made from millboard pistol targets. The yaw cards were placed approximately perpendicular to the path of the shell. After the shell was fired, the yaw-cards could be collected and analyzed to find the change in yaw of the shell over the distance of the range. The center of mass of the shell could also be found at each yaw card [3]. This technique, while effective for its purposes, was time consuming in set up for each test and in data analysis. It also lacked the ability to find the position of the shell with respect to time since the time the shell struck each yaw card was not recorded.

While yaw cards were used at ballistic ranges for many years, it was known that the yaw cards applied external forces to the projectile when the projectile penetrated through the card. Robert McCoy ran a series of tests at the Ballistic Research Laboratory (BRL) to determine the effect yaw cards have on the projectile [4]. He compared the yaw of four different projectiles when fired through yaw cards to projectiles in free flight where the yaw was measured using non-contact techniques. The difference in yaw between these two types of tests was approximately 2%. He also found that yaw cards are shown to destabilize projectiles that are spin-stabilized.

The use of yaw cards should be able to provide the pitch angle as well, but the roll angle can only be measured if the projectile has fins and is stable flight. Another issue with yaw cards are that yaw angles are easily obtained for slender shapes but difficult with bluff shapes [5]. Due to the limitations in yaw cards, the downtime between shots to change out the yaw cards, and the potential errors introduced from the forces applied to the projectile from the yaw cards, yaw cards were not considered for use in this project.

An alternative solution for measurements is non-contact measurements. The first large-scale non-contact ballistic range to produce data on projectiles in free flight was the Aerodynamic Range at the US Army Aberdeen Proving Grounds in 1943 [7]. Two facilities were constructed at Aberdeen Proving Grounds and are still active today: The Aerodynamics Experimental Facility (AEF) and the Transonic Experimental Facility (TEF).

The AEF has a range length of 285 ft and originally used 50 spark stations over the length of the range. Each spark station is made up of a sensor, a spark box, and a camera. The sensor was used to trigger the spark box and the camera when the projectile passes through the sensor. The spark box is an air-gap flash that provides lighting less than 1 μs in duration. Photographic plates are placed at each station and used to record the shadow of the projectile. The cameras at this facility originally used film media to record data. The time intervals between spark discharges is electronically recorded. The testing facility is mainly for smaller munitions, but projectiles with fin spans up to 60 mm have been launched at this range [1].

The TEF has a range length of 1,000 ft but does not have spark stations along the full length of the range. This range uses the same type of spark station as the AEF; however, the test section area for the projectiles is 22 ft by 22 ft, which is much larger than the AEF. The TEF was used for larger projectiles such as 60-mm mortars or artillery shells.

Since its inception, several reports on various tests and attempts to modernize the spark range have been published by the Army Research Laboratory (ARL). Davis reports on different ground-based free-flight measurement systems and onboard free-flight measurement systems used at the AEF and TEF in 2009 [8]. Similar spark stations to the ones Nelson described were still used, but IR sensors were used to trigger the spark stations. Each station used orthogonal shadowgraph cameras to capture data, and the air-gap flash were still used for lighting. Other ground-based systems include fixed head radar technology that can be used to track the projectile which will provide a velocity history. Another technology is tracking radar which will provide the trajectory arc of the projectile.

In addition to the ground-based equipment, telemetry (TM) equipment was also added to the projectiles. High g-qualified microelectronic sensor can be added to projectiles for data acquisition during the flight of the projectile. Sensors are added to the projectile, and they require a power supply and the telemetry components needed to transmit any measurements taken. Additionally, a TM ground station is needed at the range to receive the measurements taken. The biggest challenge in using onboard measurement systems is attaching the system to the projectile without changing the aerodynamic properties. This problem is especially true for smaller projectiles since inserting electronics inside the projectile might not be feasible and attaching electronics to the outside would change aerodynamic properties.

Another significant upgrade to the AEF and TEF was documented by Ranawake in 2015 when the many of the systems were automated and digitized [9]. The most interesting automation was the use of gigabit ethernet cameras instead of the use of film to decrease the amount of down time between shots. When film was used, the film was loaded into each station with the lights off in the range. After the shot was fired, the film had to be retrieved and developed in a dark room. By changing the cameras to network cameras, the data could be collected by a computer system after each shot was complete. A program was created using a Software Development Kit (SDK) that connected a computer to the camera, configured the camera settings such as exposure time and trigger mode, and then downloaded the image from the camera to the computer after the shot was complete. Having the images in digital form eliminated the process of digitizing film for image processing.

Other ballistic test ranges were operated at the Naval Ordnance Laboratory at White Oak [6]. Three test ranges were operated there: the Hyperballistics Range (HBR), the Pressurized Ballistics Range (PBR), and the Aerophysics Range (APR). The HBR and PBR both used dual-plane spark shadowgraph stations where the shadowgraph stations were orthogonal to each other. The APR used four single-plane rotating-mirror camera stations to gather images.

The previously mentioned ballistics ranges are all geared towards testing military munitions and only generate a single image at each station. For rapidly rotating projectiles, complete rotations may occur between stations. Many other hypersonic ballistic ranges are used worldwide and are documented by Seiler and Igra [7], and these ranges test munitions or are used for missile or space programs. High-speed video cameras were used at all the ranges mentioned in his report.

Another method of tracking projectiles was outlined by Theobalt, Albrecht, Haber, Magnor, and Seidel [10]. One objective of their experiment was to track motion sequences over a distance using low cost equipment. Their experiment involved throwing a baseball and capturing a single multi-exposure image of it using a strobe light. A single camera station was set up to capture the image of the baseball in flight with the baseball traveling away from the camera. By using cameras set up in stereo vision, the 3D position of the ball could be found with respect to the camera station at each strobe pulse. Colored symbols painted onto the baseball to serve as optical markers. The colored markers were visible in the data collected and could be found using contour finding algorithms in OpenCV. By tracking these markers, the rotation axis and spin frequency could be found. While the size and velocity of baseball differs greatly from the velocity of a fragment, this technique seemed promising for a low-cost alternative to high-speed video.

2.2 Imaging Fundamentals

A digital camera is a well-known device that captures light with an image sensor to create a digital image. The image produced is dependent on the image sensor, monochrome versus Bayer filter, exposure time, focal length of the lens, aperture of the lens, and the amount of light in the scene. For low light or high-speed applications, having the camera receive the highest amount of signal is critical to producing good images.

The image sensor is a sensor that converts incoming light into an electric charge based on the sensors Quantum Efficiency (QE) [11]. The QE is the percentage of electrons generated compared with the number of photons of light that have hit the sensor. The sensor is divided into areas called pixels, and the electrons are stored in the pixel. The number of electrons that can be stored in each pixel is called the saturation capacity, and if the pixel receives more electrons that the saturation capacity, no additional electrons will be stored. Once the light collection is completed for a given period, the charge of each pixel is measured, and this measurement is called the signal. The camera then converts the signal for each pixel to a digital value. For monochrome cameras, each pixel is assigned an 8-bit integer where the value 0 appears as black, and the value 255 appears as white. All values in between are various shades of gray where higher values are a lighter shade of gray. The formula to calculate the signal without respect to time, is based on the area of the pixel, the quantum efficiency of the image sensor, and the density of incoming light measured in photons/μm^2 [11].

$$Signal = Light\ Density * Area\ of\ Pixel * QE \tag{1}$$

By increasing the exposure time of the image sensor, the sensor will have a longer period to collect photons on each pixel and therefore a higher signal. The exposure time can be controlled two different ways. The first, most common way, is to control the shutter speed of the camera. The shutter will remain open for a set period for the sensor to collect light, then it will close and block incoming light. The other method is to place a camera with an open shutter in a dark environment and control the length of time a light source can produce light. This is the technique used for stroboscopic imaging. In this technique, the exposure time is dependent on the length the strobe light pulses for.

To create a color image, a Color Filter Array (CFA) is added between the image sensor and the incoming light. While different camera manufacturers may use different filters, the Bayer Filter is used in most digital image sensors. The Bayer Filter uses an array of red, green, and blue light filters to allow certain colors of light onto specific areas of the image sensor [12]. By aligning the filter with the pixels on the image sensor, each pixel will only receive red, green, or blue light. To construct the image, demosaicing algorithms are used to interpolate pixel values for missing color information [13]. The Bayer Filter typically has a pattern with 50% green light filters, 25% red light filters, and 25% blue light filters. By using filters in front of the image sensor, approximately 75% of light is blocked from entering the sensor [14].

The next component of the digital camera is the lens, and the lens focuses light from light sources onto the image sensor. The Field of View (FOV) of the image is dependent on the size of the image sensor and the focal length of the lens. Figure 1 shows a top view of a lens focusing light onto an image sensor. The image sensor is located on the left of the image. In the figure, w is the width of the imager, f is the focal length of the lens, D is the distance from the lens to the scene of interest, and FOV_H is the horizontal FOV of the imager at the scene of interest. For the vertical FOV, the width of the sensor should be replaced by h, the height of the sensor.

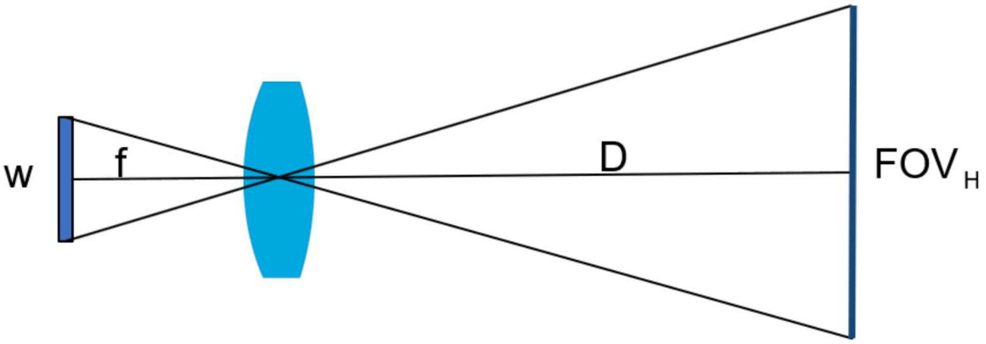

Figure 1: Field of View Diagram

To find the horizontal FOV, use the following formula:

$$FOV_H = \frac{w * D}{f} \tag{2}$$

The resolution on target is a measure of distance per pixel at the scene of interest a distance D from the lens. The resolution on target is dependent on the resolution of the image sensor and the calculated FOV. The number of horizontal pixels, pix_{horz}, is used with the horizontal FOV, and the number of vertical pixels (pix_{vert}) is used with the vertical FOV. The resolution on target can be calculated using the following formula:

$$Resolution\ on\ Target = \frac{FOV_H}{pix_{horz}} \tag{3}$$

The last component of the lens is the f-number which is determined by the focal length of the lens and the size of the aperture [15]. The f-number is found using the following formula where f is the focal length and d is the size of the aperture:

$$Fnumber = \frac{f}{d} \tag{4}$$

Smaller f-number values allow more light through the lens, and larger f-number values allow less light into the image sensor. The amount of light that is let in through is dependent on the area of the aperture, which in turn is dependent on the squared value of the radius. By increasing or decreasing the radius by a factor of 2, the amount of light will be increased or decreased by a factor of 4.

When a lens is focused, there is a plane orthogonal to the image sensor and some distance from the imager called the Plane of Focus (POF). For an object located on this plane, the light emitting from a point on that object will enter the lens and be focused into a single point on the image sensor. For objects outside this plane, a single point on the object will be focused onto the sensor as a circle with a radius *r.* If the radius of the circle projected onto the image sensor is larger than the size of a pixel, the object will appear out of focus. The depth of field is the distance from the POF that objects still appear in focus on the image sensor [15]. Figure 2 shows an example of objects outside the POF and the circles created on the imager. In the top half of the figure, the image sensor is located at point 5, point 1 is a point located farther away from the camera than the POF, point 2 is a point located on the POF, and point 3 is a point located closer to the camera than the POF. The size of the circle each point projects on the image sensor is shown to the right. In the lower half of the figure, an aperture has been introduced and is allowing in a quarter of the light through to the sensor. The circles created by each point appear smaller on the image sensor which will make them appear more in focus. By increasing or decreasing the f-number of the lens, the depth of field will decrease or increase respectively.

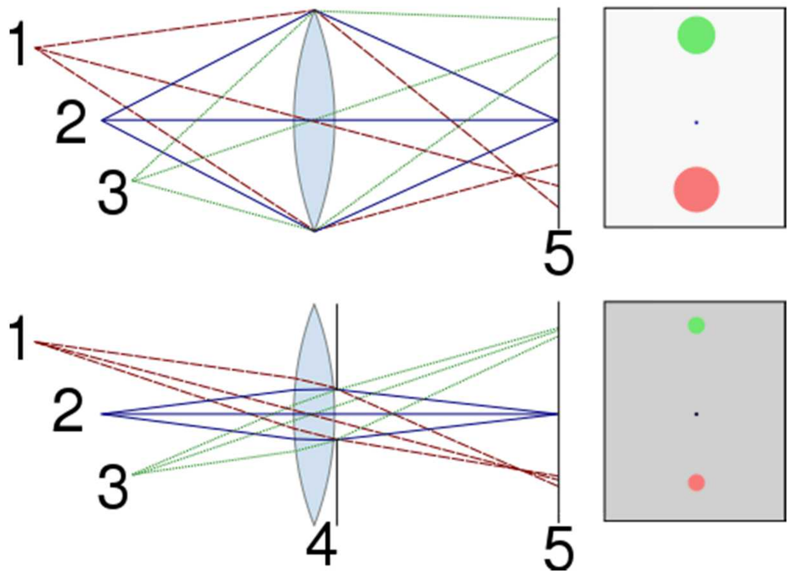

Figure 2: Depth of Field Illustration [16]

The ideal f-number for a camera will be set to provide the maximum possible light into the sensor while providing a large enough DOF for any object in the region of interest to appear in focus. This will produce the highest signal for the image sensor while ensuring objects in a region of interest remain in focus.

2.3 Stroboscopic Imaging

Stroboscopic imaging is an imaging technique where a short pulse or multiple short pulses of light are used to provide light for the image. This form of imaging is often used on vibrating or rotating objects to find the frequency of the vibration or rotation [17]. It has also been used in other areas of research to find the velocity and acceleration of moving objects [18], or studying material properties [19]. One concern for stroboscopic imaging of rotating objects is using the wrong frequency for the strobe light and aliasing the moving object [20] [21]. Aliasing will occur if the sampling of the system is less than half of the frequency of the moving object. In this case, the observed frequency of the rotating object will be different than its actual frequency [21]. To avoid aliasing, the frequency of the strobe light must be set to a value that is twice as high as the frequency of the rotating object.

The equipment needed to take a stroboscopic image includes a camera, strobe light, and a moving object. The camera is set up with either an open shutter or a long exposure time such that the strobe light can flash multiple pulses of light before the shutter closes. With an open shutter, the number of strobe light pulses must be controlled from the strobe light. If the camera shutter opening is synchronized with the strobe light, the frequency of the strobe light and the shutter time will determine the number of strobe light pulses in each image.

Stroboscopic images with linearly moving objects are typically taken in a dark environment with a dark backdrop [22]. The dark environment prevents any extraneous light sources hitting the image sensor and overexposing the image. Since the object is moving, each strobe light will illuminate the object once in each position while stationary objects in the background will be illuminated in that position multiple times. Having a dark backdrop ensures that the background of the image remains dark and does not overexpose portions of the image.

The final element of stroboscopic imaging is the ability to freeze motion of the object for each strobe pulse. If the strobe light has a pulse length that is too long, the moving object in the image will appear blurry. To avoid blur, the exposure time must be less than the time it takes for an object to move across one pixel [14]. To calculate the maximum pulse length of the strobe light, the values for velocity, v, of the object and resolution on target are needed. The maximum time of the pulse, t_{pulse}, can be calculated using the following formula:

$$t_{pulse} < \frac{Resolution\ on\ Target * 1\ pixel}{v} \tag{5}$$

2.4 Stereo Vision Camera System

A stereo vision camera system is a system comprising of two cameras and is designed to find three-dimensional (3D) information from images. A single camera performs a perspective projection which transforms a 3D point onto a 2D image and loses the third dimension in the transformation [23]. By adding another camera to the system, the third dimension of the point can be found. Figure 3 shows an example of this where the left camera cannot tell the depth of the object X. As shown in the figure, the points X_1, X_2, or X_3 would be projected onto the same pixel of the image sensor.

If a second camera is added to the system, the FOV for the second camera will see the points X, X_1, X_2, and X_3 on different pixels. To relate the cameras to each other, a line is drawn between the center of each camera called the baseline [23]. The point of intersection of the baseline and the image plane is called the epipole [24][25]. A line is formed on the second camera that contains the epipole and the points X, X_1, X_2, and X_3 projected onto the image, and this line is called the epipolar line [25][26]. For an object X projecting on the left camera pixel X_L, the object X will project onto the right camera along the epipolar line. Likewise, an epipolar line is created on the left camera for pixels on the right camera.

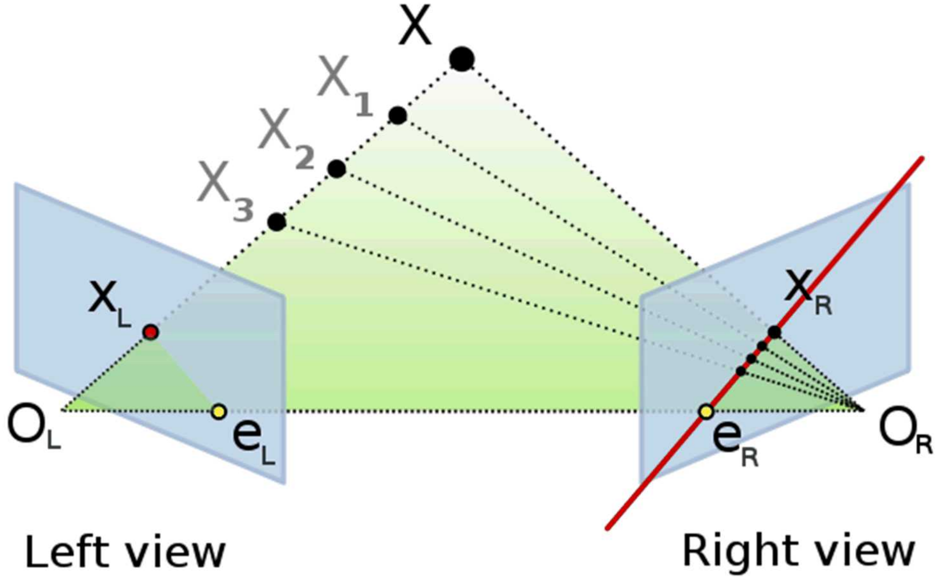

Figure 3: Epipolar Geometry [27]

For 3D data to be found from the stereo vision system, the system must first be calibrated. The goal of calibrating the system is to find the intrinsic properties of each camera, and the extrinsic pose of the cameras. Finding the intrinsic properties of each camera can occur simultaneously with the calibration of the extrinsic pose of the camera with a known calibration target [28].

The intrinsic matrix for a camera is defined by the following matrix [29]:

$$K = \begin{pmatrix} f_x & s & x_0 \\ 0 & f_y & y_0 \\ 0 & 0 & 1 \end{pmatrix} \tag{6}$$

The focal length f_x and f_y should both be equal to the focal length of the lens and is the distance between the image plane and the camera center [24]. These two values should be equal, but they may differ in practice due to distortions in the lens, errors in calibration, or flaws on the image sensor. The axis skew s is shear distortion in the projected image. In most cases, the sensor is not skewed, and this value is set to zero. The variables x_0 and y_0 are the optical center or principal point typically located at the center of the image.

The extrinsic properties of the camera system are defined by the Fundamental Matrix F, and it is the algebraic representation of the epipolar geometry [23]. It is a 3x3 matrix and relates the same points between the images produced by the stereo vision system. For this paper, the Fundamental Matrix and intrinsic matrix for each camera were found using the Correlated Solutions' software VIC-3D.

To calibrate the stereo vision system in this software, a series of images is simultaneously taken by both cameras in the stereo pair as a calibration board is held in front of the cameras. The calibration board has an array of black circles on a white background where the distance between circles is known. Three of the black circles contain a smaller white circle in the center, and these three points are placed in an "L" shape. These points are used in the image recognition to help ensure each circle is matched with the correct circle in the second camera view. The calibration board is rotated and moved around to ensure it covers the entire FOV of each camera. These images are then loaded into the software, and it examines each pair of images to find each point of the calibration board in the first camera image and its corresponding point on image from the second camera image. The distance between each circle is input into the software. It then calculates the intrinsic and extrinsic properties of the camera system. Figure 4 shows a calibration image. Figure 5 shows the same image in VIC-3D. Each circle found in the software is shown with a teal circle, and the three black circles with an inner white circle are shown with blue, pink, and yellow circles. Once the calibration is complete and the intrinsic and extrinsic properties are known, the camera system can find the XYZ position of objects in the FOV of both cameras.

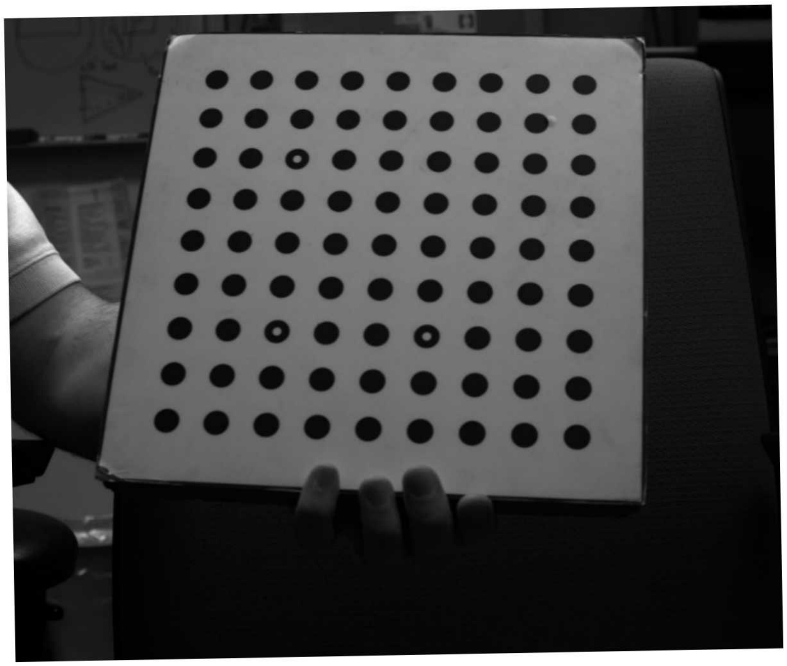

Figure 4: Original Calibration Image

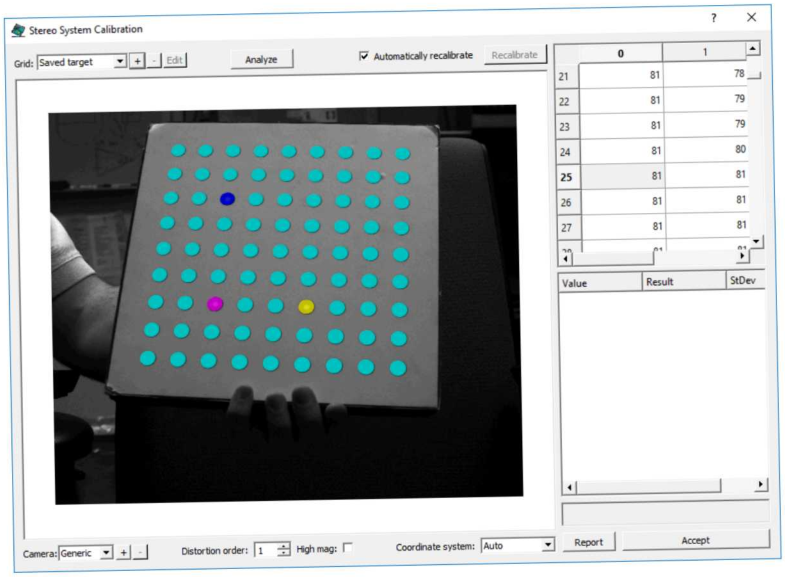

Grid: Saved target

☑ Automatically recalibrate

	0	1
21	81	78
22	81	79
23	81	79
24	81	80
25	81	81
26	81	81
27	81	81

Camera: Generic

Distortion order: 1

High mag: ☐

Coordinate system: Auto

Figure 5: Calibration Image in VIC-3D

CHAPTER 3 EXPERIMENTAL SETUP

Two test series were conducted to validate the stroboscopic stereo-vision camera stations. The goal of the first test series was to select the best camera, the best backdrop, and to ensure the strobe light produced sufficient light to see the projectile. This test also validated the timing equipment and IR sensors used as input triggers. Three different cameras and backdrops were used to gather results, and then a comparison was made to select the best equipment to use. The goal of the second test series was to capture the three-dimensional trajectory of a tumbling projectile. Capturing the flight of the projectile was accomplished using seven stroboscopic camera stations over the length of the testing facility. Two different types of projectiles were launched, and they were launched from a non-rifled barrel to maximize the likelihood of tumbling.

3.1 Testing Facility

Both tests were conducted at the Ballistic Launch Tube (BLT) facility at Sandia National Laboratories. The BLT facility consists of a firing range and personnel facility. The firing range was made from a steel tube with a metal shipping container on the up-range side and a small room on the downrange end of the tube.

The shipping container was connected to the personnel facility and held a mounted gun as well as a chronograph. The gun barrel was mounted on a steel frame, could be remotely activated, and different sizes or types of gun barrels could be used depending on the test. The chronograph was made up of two IR sensors spaced 2 feet apart, and it was used to record the velocity of each shot fired. Black plastic was used to cover the front and back of the chronograph to ensure it was triggered from the projectile and not from the muzzle flash. The small room downrange held a bullet trap and a large steel plate as a secondary bullet stop, and it was connected to the personnel facility. The total length of the firing range was approximately 76 feet.

Figure 6: Gun Stand and Chronograph Inside the Firing Range

The personnel facility was made up of two shipping containers and located to the side of the firing range. It held the equipment to remotely activate the gun and the display for the chronograph. It also held a loading workbench which was used to load a custom amount of black powder into each round. For safety purposes, all personnel were restricted to this facility during testing.

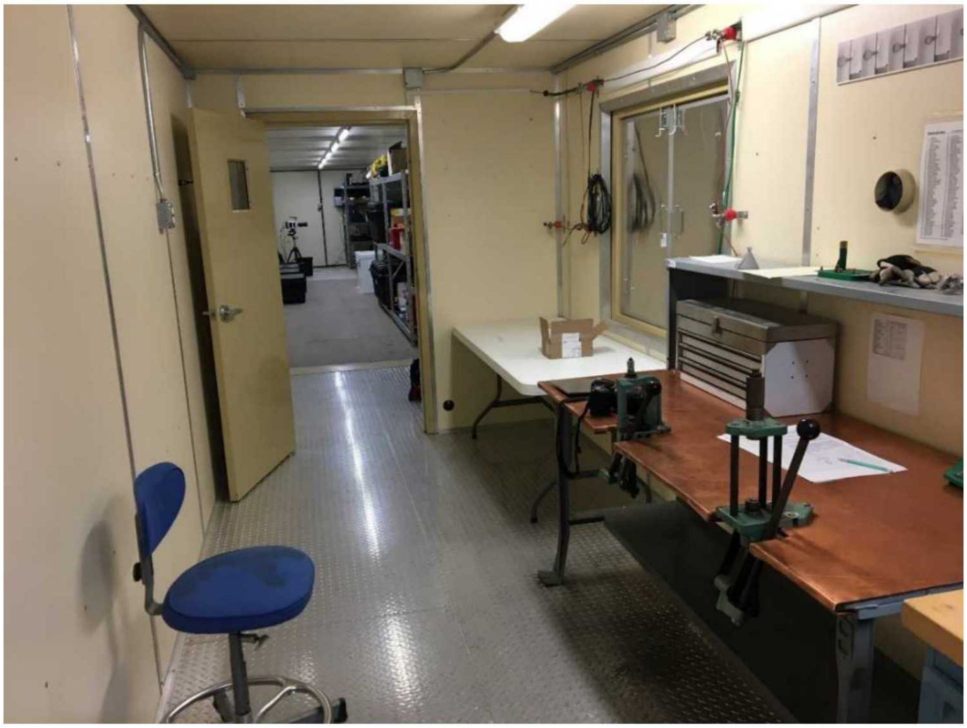

Figure 7: Personnel Facility in BLT

3.2 Test Series 1

For the first test series, a total of two stroboscopic camera stations were set up as shown in Figure 8.

Figure 8: Equipment Configuration for Test Series 1

3.2.1 Camera Stations and Backdrops

The first camera station was mounted using a tripod and 80/20 aluminum framing, and it was located approximately 2 feet downrange of the gun barrel and approximately 2.5 feet from the path of the projectile. The camera station used two different Point Grey USB Grasshopper cameras in a stereo vision configuration. The model numbers of the cameras were: GS3-U3-28S5M-C and GS3-U3-32S4M-C. A flat black canvas backdrop was used for the first eight tests, and then a flat white canvas backdrop was used for the remainder of the testing.

Figure 9: Camera Station 1 for Test Series 1

The second camera station was located inside the tube of the BLT, and it was positioned approximately 30 feet from gun barrel and approximately 3 feet from the path of the projectile. It was mounted using 80/20 aluminum framing to a piece of angle iron welded on the side of the steel tube. This camera station used two of the same model Point

Grey Firewire cameras in a stereo vision configuration. The model number of the camera was the GX-FW-60S6M-C. A piece of plexiglass was placed on either side of the camera station to protect it from the projectile. For the first eight tests, a flat black canvas backdrop and a white reflective screen were used. The backdrops were positioned to take up approximately half the field of view of the cameras. The black backdrop was positioned on the up-range side, and the reflective screen was positioned on the downrange side of the camera's view. After the first eight tests, a flat white canvas backdrop was used instead of the reflective screen. The camera model, lens size, and mm/pixel of each camera is shown in Table 1.

Figure 10: Camera Station 2 for Test Series 1

3.2.2 Lighting

Each camera station was equipped with a Vela One strobe light. This strobe light has an array of 9 Computer on Board (COB) LEDs that pulse simultaneously, and it could pulse between one and six times per series. The pulse length could be varied between 500 ns and 5 µs, and the time between pulses was adjustable from 10 µs to 250 µs. After a series of pulses, there was a minimum of 1 ms before another series of pulses can occur. The Vela One had a 10 µs delay before the first strobe flashes after receiving a trigger. The number of pulses, length of the pulses, and the time between pulses for each camera station are shown in Table 1.

Table 1: Test Series 1 Camera Station Configuration

Camera Station	Camera Model	Lens Size	mm/pixel	Number of Pulses	Pulse Length	Time Between Pulses
1	GS3-U3-28S5M-C	8mm	0.519	6	500 ns	50 µs
	GS3-U3-32S4M-C	8mm	0.394			
2	GX-FW-60S6M-C	6mm	0.691	6	500 ns	80 µs

3.2.3 Timing and Triggering

On the camera stations, Both the cameras and the strobe light needed to be triggered. The trigger for the cameras would cause the camera to open its shutter for a preprogramed amount of time, and the trigger for the strobe light would cause the strobe light to begin pulsing. Once the camera received the trigger, the shutter would open in less than 10 µs. Since there was a 10 µs delay from when the Vela One received the trigger before it began pulsing, all the devices could be triggered using the same signal.

The first camera station was located up-range of the IR sensors, so this station was triggered using the same signal that fired the gun plus some delay. Finding the correct time involved trial and error, but the best result was the signal from the gun plus 4.5 ms. Occasionally, this camera station would miss the projectile since there was some variation on the time between the trigger to fire the bullet and when the bullet would eject from the barrel.

The second station was triggered using the Labsmith LC880 Programmable Experiment Controller. The Labsmith was capable of outputting a trigger on a dynamically delayed pulse. For this type of pulse, the Labsmith takes the time difference between two input triggers and scales the output trigger according the following formula:

$$t_{output} = \left(t_{input1} - t_{input2}\right) * 2^{n} + t_{input2} + t_{delay} \tag{7}$$

In this formula, t_{output} is the time of the output trigger, t_{input1} is the time of the first input trigger, t_{input2} is the time of the second input trigger, n is a user defined whole number between -4 and 4, and t_{delay} is a user defined positive or negative number used to increase or decrease the delay. In this application, the input triggers happen when the projectile passes through each IR sensor in the chronograph. This allows the output triggers to be dependent on the velocity of the projectile for each test and provides precise timing regardless of differences in projectile velocity between tests.

Two Oehler Model 57 Photoelectric Screens were placed 2 feet apart to make up the chronograph, and these screens provided t_{input1} and t_{input2} when the projectile passed through. By assuming a constant velocity of the projectile and knowing the distance from the camera station to chronograph, the values of n and t_{delay} could be calculated using the following formulas:

$$R \ = d - (d_{chrono} * 2^n) \tag{8}$$

For this formula, d is the distance between the second sensor of the chronograph and the camera station, and d_{chrono} is the distance between the sensors of the chronograph. To get the most accurate time, the value of R should be as close to 0 as possible by changing the variable n. Once R is calculated, t_{delay} can be calculated using the following formula where υ is the velocity of the projectile:

$$t_{delay} \ = \frac{R}{\upsilon} \tag{9}$$

3.2.4 Image Acquisition

Images were acquired using Point Grey Fly Capture 2 software. The software was set up to save an image each time a camera received a trigger, and the cameras were programmed to open the shutter for 500 µs on each trigger. This length of time the shutter was opened allowed all six pulses of light to flash before the shutter closed. Leaving the shutter open longer would have no benefit and could allow extraneous light sources into the sensor

3.2.5 Calibration

Each camera station was calibrated using a 9 x 9 dotted calibration board with the dots spaced 24.4 mm apart. Calibration of both camera stations was done each day to minimize error in the data. The images were input into VIC-3D Digital Image Correlation software to correlate the cameras and complete the camera station calibration. Example calibration images are shown in Figure 11 and Figure 12 below.

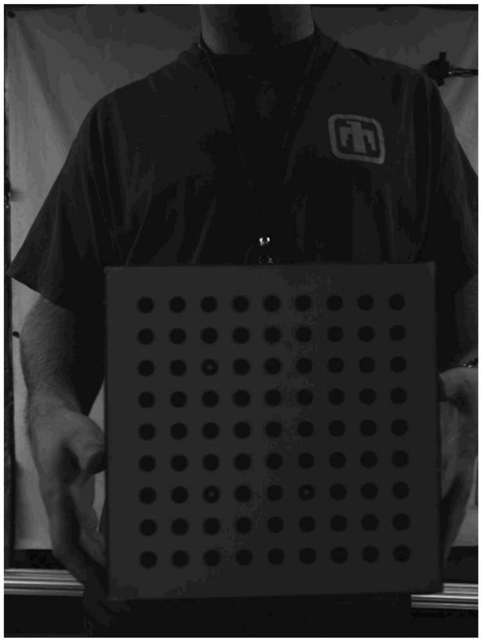

Figure 11: Calibration Image Upper Camera

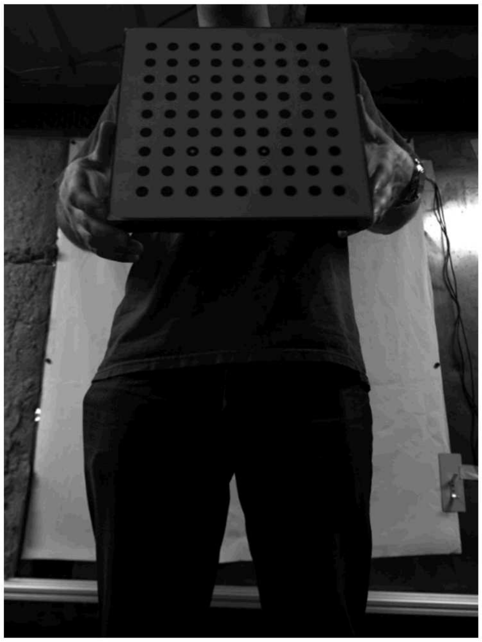

Figure 12: Calibration Image Lower Camera

3.2.6 Projectiles

Two different types of projectiles were fired during Test Series 1. The first projectile was a 0.308 caliper copper round fired from a rifled barrel. Each bullet weighed 110 grains and was loaded with black powder by the BLT staff. The other projectile was made from Ultem plastic and had dimensions of 7.62 x 39 mm. These rounds weighed 11.5 grains and were also custom loaded by the BLT staff. A total of 13 Ultem plastic rounds were fired, and a total of 31 copper 0.308 rounds were fired.

3.3 Test Series 2

For the second test series, a total of seven stroboscopic camera stations were set up as shown in Figure 13.

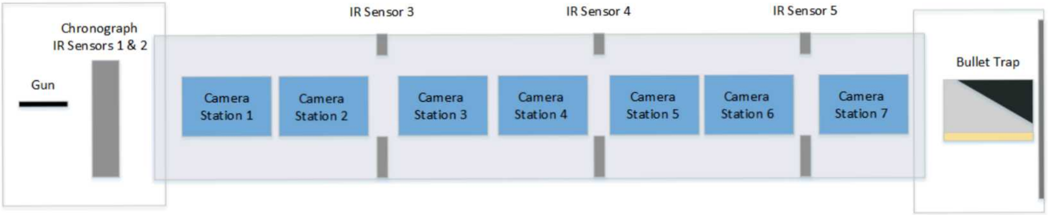

Figure 13: Equipment Configuration for Test Series 2

3.3.1 Camera Stations

The camera stations were mounted to the side of the BLT tube using 80/20 aluminum framing. Angle iron was welded to the side of the BLT to serve as an anchor point for the framing. A long section of the framing was then bolted to the angle iron to hold the frame for each camera station. Each camera station was mounted to the framing on the side of the tube and the triggering and communication cables were run along the frame running along the tube. A plexiglass shield was placed on the up-range side of each camera station to protect it from any projectiles. Figure 14 shows the camera stations mounted to the side of the BLT.

Figure 14: Camera Stations Mounted along the BLT

Two different camera stations were used for this Test Series due to the limited quantity of the Vela One strobe lights that were available for purchase. The camera station that used the Vela One had cameras mounted to the top and bottom of the Vela One. The cameras were located 19 inches apart which gave an angle of approximately 40° between the cameras. The Vela One camera station is shown in Figure 15.

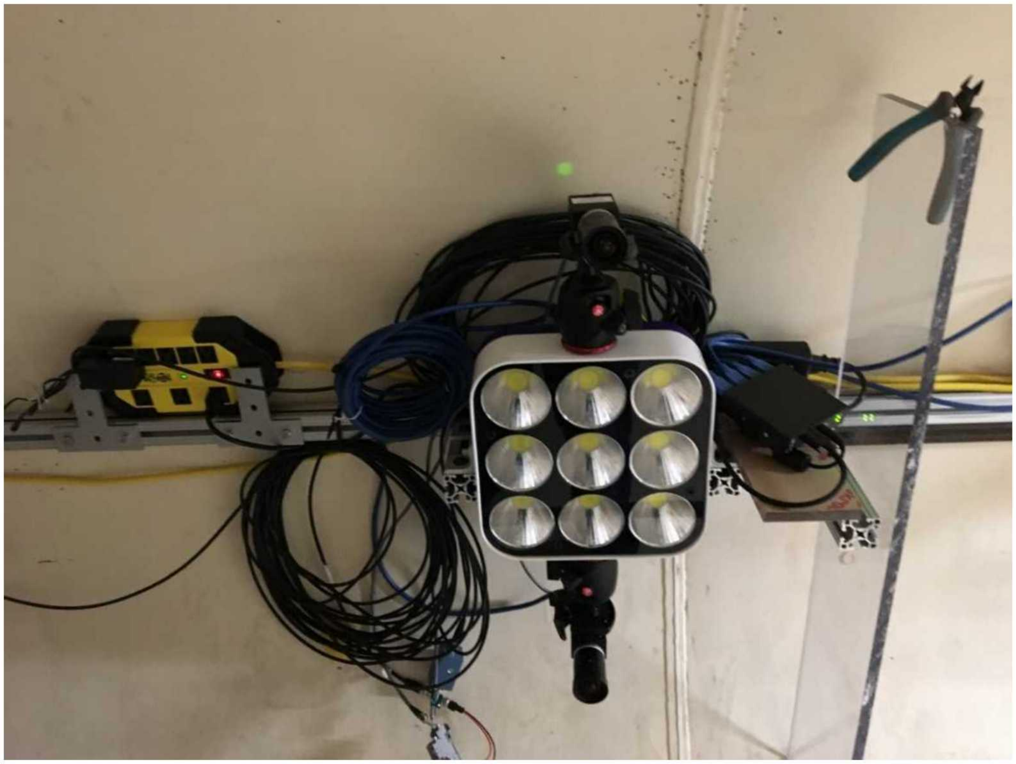

Figure 15: Vela One Camera Station

The other camera stations used two Constellation 120E strobe lights which were mounted to the frame running along the side of the tube. The strobe lights were placed 18 inches apart with the cameras centered in the middle, and the lights were synchronized to strobe simultaneously. The cameras were placed 16.5 inches apart to create a 30° between them. The Constellation camera station is shown in Figure 16. The equipment used at each camera station is shown in Table 2.

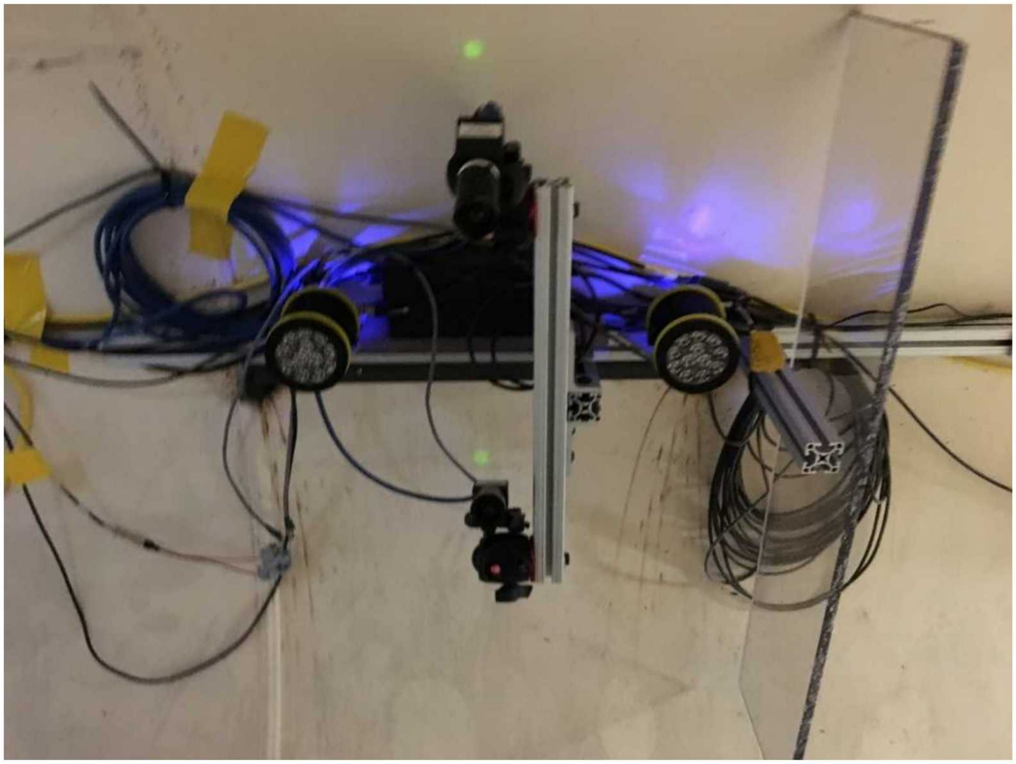

Figure 16: Constellation 120E Camera Station

3.3.2 *Backdrops*

A piece of flat white canvas was placed along the side of the tube opposite the camera stations to serve as a backdrop. The canvas was held up using rubber coated neodymium magnets.

3.3.3 *Lighting*

Four of the seven camera stations used the Vela One strobe light that was used in Test Series 1, and the other three camera stations used the Constellation 120E. The amount of pulses, length of pulses, and time between pulses are shown in Table 2. Camera station 3 was intentionally set to have a smaller time between pulses than the other camera stations to ensure the projectile was not rotating at a higher frequency than the sampling rate of the other camera stations.

The Constellation 120E produced approximately 1/10th of the lumen output compared to the Vela One. To increase the signal received by the camera at these camera stations, the cameras were binned to ¼ resolution which increased the light per pixel by a factor of 4. The binning process was done using Point Grey FlyCap Software. With the lower resolution, the light could be pulsed for twice as long without the image blurring, so the pulse time was increased from 500 ns to 1 μs. Combined, these changes increased the light per pixel by a factor of 8 but reduced the resolution on target.

The Constellation strobe light had a narrower beam angle than the Vela One, so two Constellations were used at each camera station to maximize the amount of light along the horizontal FOV. Even with two strobe lights, these camera stations illuminated less area compared to the Vela camera stations.

The Constellation strobe lights had a warm up period where initial light pulses did not produce as much light as subsequent light pulses. By running these strobe lights continuously using a square wave produced by a signal generator, the light pulses during the test would provide the maximum light; however, by running the strobe lights on a different signal than the camera trigger, the exact timing of each strobe pulse could not be found. The strobe light, pulse length, and the time between pulses for each camera station is shown in Table 2.

Table 2: Test Series 2 Camera Station Configuration

Camera Station	Camera Model	Lens Size	Mm/pixel	Strobe Light	Pulses	Pulse Length	Time Between Pulses
1	GS3-U3-28S5M-C	6mm	0.577	Vela One	6	500 ns	136 µs
2	GS3-U3-28S5M-C	6mm	1.153	Constellation 120E	6	1 µs	100 µs
3	GS3-U3-28S5M-C	6mm	0.577	Vela One	5	500 ns	52 µs
4	GS3-U3-28S5M-C	6mm	1.153	Constellation 120E	6	1 µs	100 µs
5	GS3-U3-28S5M-C	6mm	0.577	Vela One	6	500 ns	100 µs
6	GS3-U3-28S5M-C	6mm	1.153	Constellation 120E	6	1 µs	100 µs
7	GS3-U3-28S5M-C	6mm	0.577	Vela One	6	500 ns	117 µs

3.3.4 Timing and Triggering

Triggering of all the camera stations was accomplished using the Labsmith LC880 Programmable Experiment Controller and Oehler Model 57 Photoelectric Screens (IR sensor). The input triggers from IR sensors 1, 2, 3, and 4 were recorded using Tektronix DPO4104B oscilloscope, and the input trigger from IR sensor 5 was not recorded due to limited channels on the oscilloscope. The output trigger to fire the gun and the input triggers from IR sensors 1 and 2 were recorded on a separate oscilloscope operated by BLT site personnel.

Since the velocity of the projectiles was expected to decrease significantly during flight, additional IR sensors were needed farther down the tube of the BLT. The first two IR sensors were placed approximately 4 feet from the end of the gun barrel, and they were spaced 2 feet apart to act as the chronograph. Camera stations 1 and 2 were placed near the chronograph so that a dynamically delayed pulse was used for a trigger. A single IR sensor was placed approximately 2 feet up-range from camera station 3. To reduce the chance of the IR sensors get hit by the projectile, the IR transmitter was mounted on the floor of the tube, and the IR receiver was mounted to the ceiling of the tube. Both sensors were held in place using rubber coated neodymium magnets. The third IR sensor was used to trigger camera stations 3 and 4 using a delayed pulse.

IR sensor 4 was mounted 2 feet up-range of camera station 5, and IR sensor 5 was mounted 2 feet up-range of camera station 7. The projectile was expected to deviate farther from the axis of the barrel the farther it traveled down range, so wider IR sensors were needed to ensure the projectile was detected as it passed. Two of the IR sensors were connected to each other to make a single IR sensor. Both sensors were mounted using rubber coated neodymium magnets. IR sensor 4 was used to trigger camera stations 5 and 6, and IR sensor 5 was used to trigger camera station 7 using delayed pulses. Figure 17 and Figure 18 show the double wide IR transmitter and receiver mounted to the floor and ceiling of the BLT tube. Figure 19 shows all three IR sensors mounted in the BLT tube in front of the camera stations.

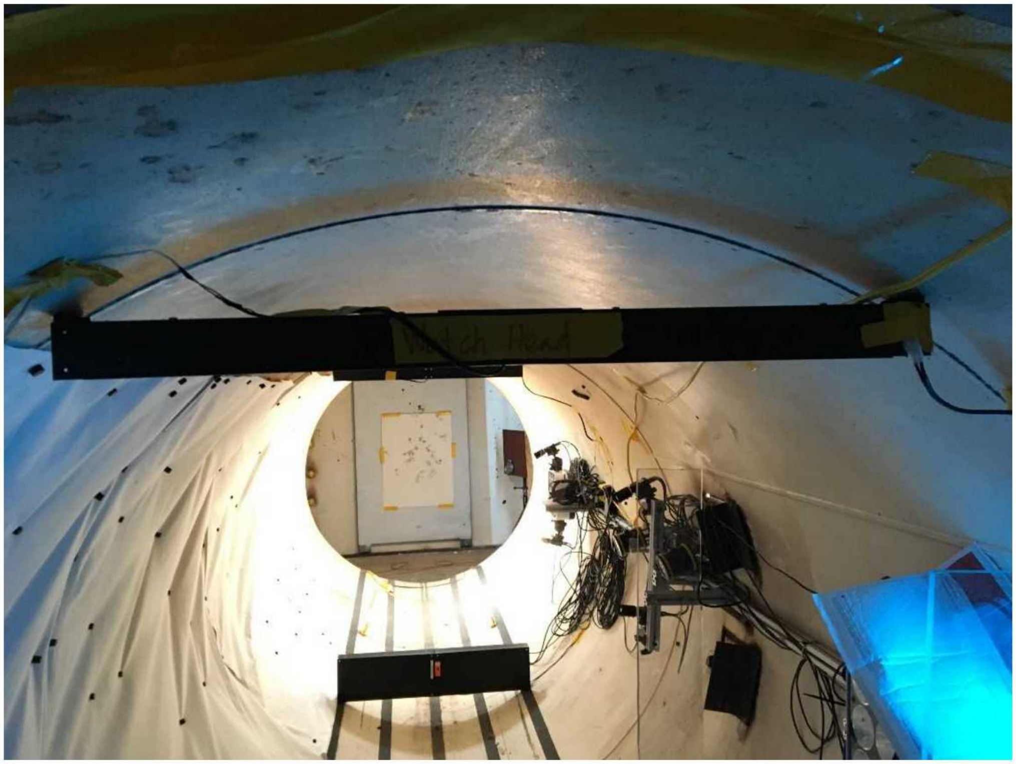

Figure 17: Double IR Receiver Mounted to Ceiling

Figure 18: Double IR Transmitter Mounted to Floor

Figure 19: IR Sensors in BLT Tube

During the initial ring out shots, the strobe lights triggered the downrange IR sensors instead of the projectile. Black fabric was placed in front of each IR sensor located in the BLT tube. A circular hole was cut into the fabric, so the projectile would be less likely to strike the black fabric; however, the curtains were torn down on some shots and had to be set back up. The fabric was held in place using rubber coated neodymium magnets.

3.3.5 Image Acquisition

Images were acquired using Point Grey Fly Capture 2 software. The software was configured to save an image each time a camera received a trigger. For the camera stations using the Vela One strobe light, the cameras were programmed to have an open shutter for 800 µs. For the cameras stations using the Constellation 120E, the cameras were binned to ¼ resolution and programmed to have an open shutter for 650 µs.

3.3.6 Calibration

Each camera station was calibrated using a 9 x 9 dotted calibration board with the dots spaced 24.4 mm apart. Calibration of all seven camera stations was only done one time due to time constraints. The calibration images were taken before any data images were collected. The calibration images were run through VIC-3D Digital Image Correlation software to correlate the cameras and complete the camera station calibration. Example calibration images are shown Figure 20 and Figure 21.

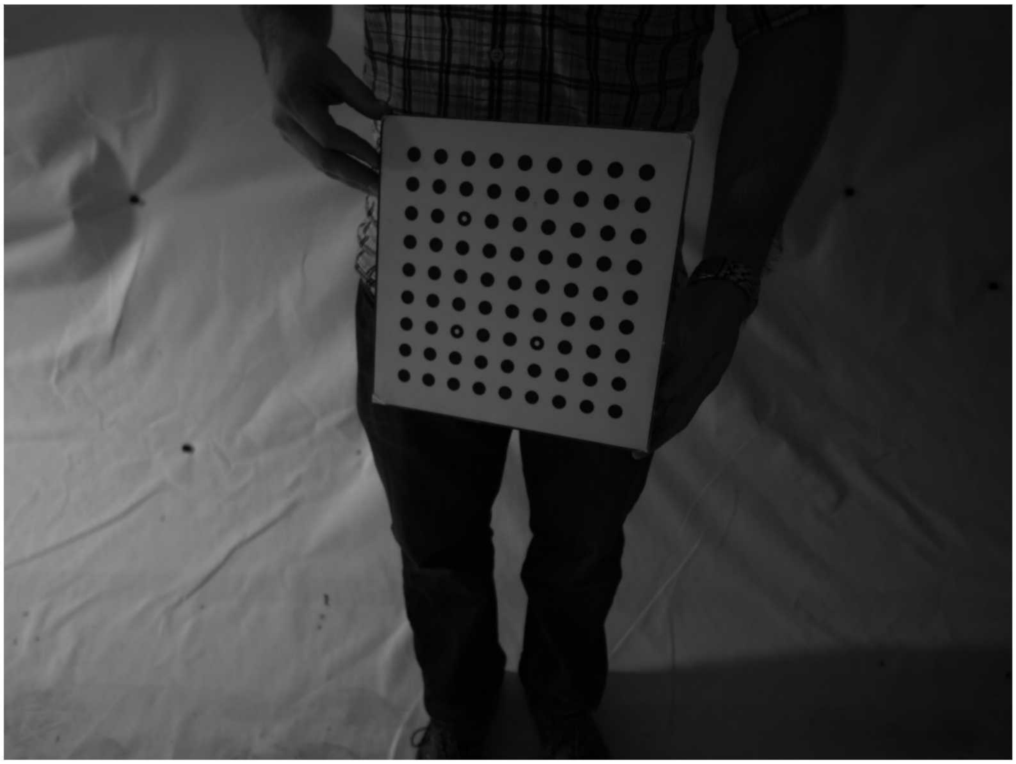

Figure 20: Camera Station 1, Upper Camera Calibration

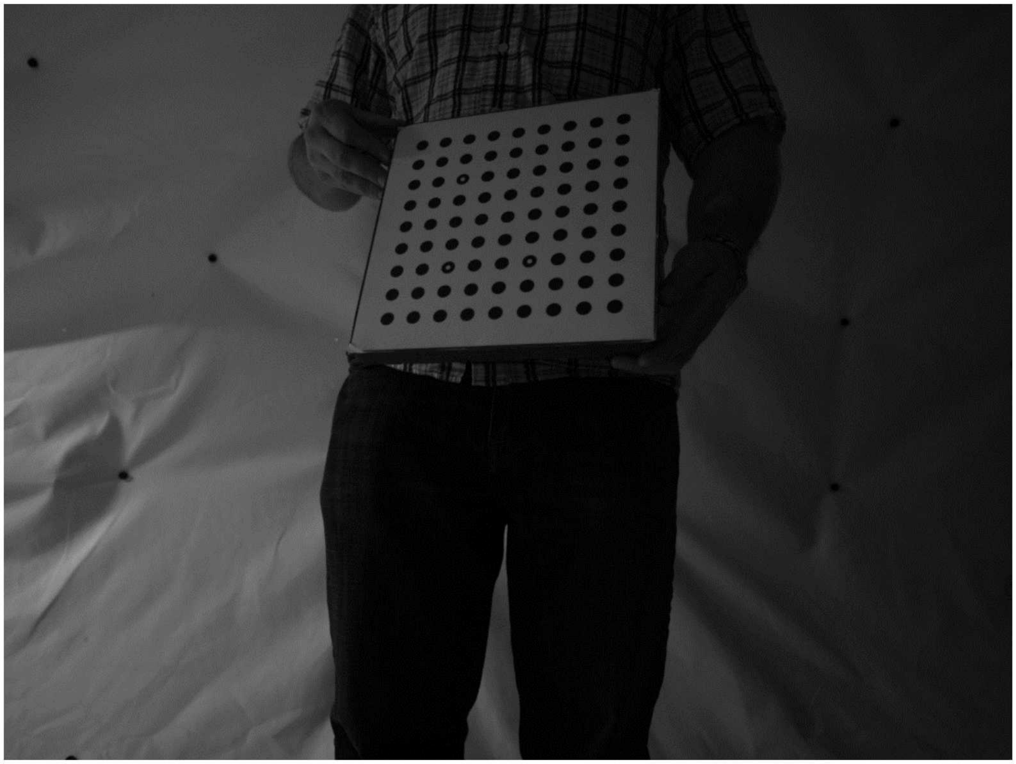

Figure 21: Camera Station 1, Lower Camera Calibration

3.3.7 Camera Station Registration

To combine the position data of the projectile from each camera station, each camera station needed to be registered into a global coordinate system. The gun was also registered into the global coordinate system to compare the position of the projectile to the expected trajectory for a rifled bullet. To accomplish this, a survey of the facility was done using an API coordinate tracking machine and a spherically mounted retroreflector (SMR). The frame of the gun, the gun barrel itself, and the inner surface of the BLT tube were all surveyed. The three-dimensional points were recorded into New River Kinematics' Spatial Analyzer software.

To register each camera station, a DIC tube was used that had a speckle pattern on the side, three calibration markers placed on top of the speckle pattern, and mounting locations for the SMR located at each end of the DIC tube. A hole was drilled in each end cap of the tube along the axis of the tube. The DIC was mounted to an aluminum X-Beam frame with adjustable feet. A laser level was mounted to the X-Beam frame so that the laser would shine through the holes that were drilled in the tube. A model of the DIC tube was made in Spatial Analyzer that included each SMR mounting location and each calibration marker location. The DIC tube, laser level, X-Beam frame, and the SMR mounting locations are shown below in Figure 22.

Figure 22: DIC Tube Mounted to X-Beam Frame

Before the DIC tube was used, a bore laser was placed in the gun barrel. A mark was made and end of the range where the bore laser hit the end plate. The DIC tube was placed in front of each camera station with the speckle pattern and calibration markers facing the cameras. First, the DIC tube was aligned with the axis of the gun barrel using the laser level. To do this, a laser was shot up-range and through the DIC tube downrange. The DIC tube was adjusted until the laser hit the gun barrel and the mark on the end plate at the end of the range. The DIC tube was then leveled by adjusting the feet of the frame and using the laser level as a reference point. After this, small adjustments were then needed to ensure the DIC tube was still aligned correctly with the gun barrel and mark at the end of the range. After the tube was properly aligned, images from each camera at the camera station were taken. The DIC tube was surveyed by placing the SMR on each mount, and the data was recorded in Spatial Analyzer. Figure 23 shows the DIC tube in front of camera station 7. Figure 24 and Figure 25 show the upper and lower camera views of the DIC tube in front of a camera station.

Figure 23: DIC Tube in Front of Camera Station 7

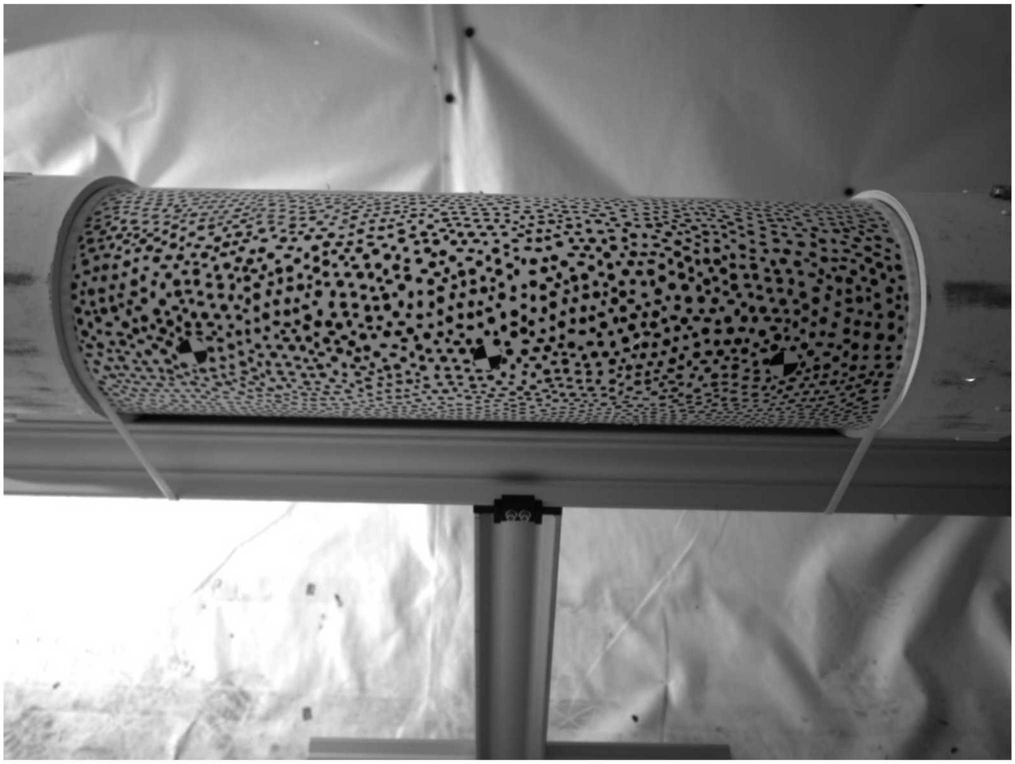

Figure 24: DIC Tube Upper Camera View

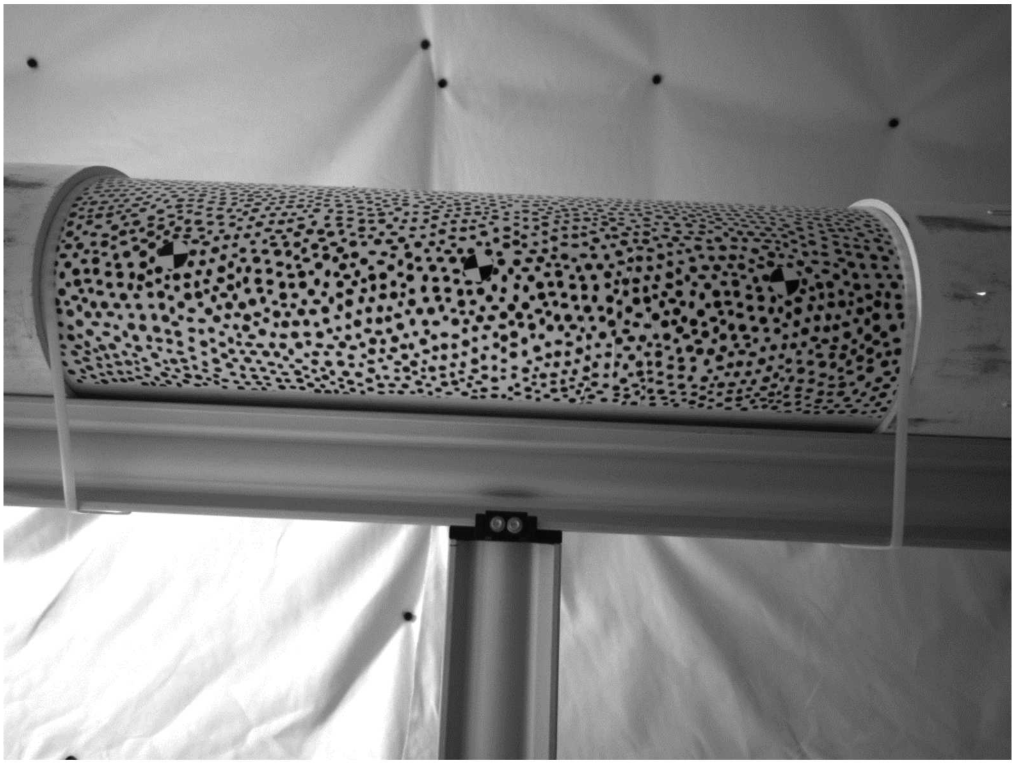

Figure 25: DIC Tube Lower Camera View

3.3.8 Projectiles

Three different projectiles were fired during Test Series 2. All three types of projectiles were custom loaded by the BLT staff to have an intended initial velocity of 3,000 ft/s or 914.4 m/s. The first projectile was 0.308-inch rounds fired from a rifled barrel. These shots were used as ring out shots to verify the camera stations, strobe lights, IR sensors, and triggering systems were working correctly. The next projectile was made of Ultem plastic and was fired from an un-rifled 12-gauge barrel using a gas block in the shell. It was made from a 0.725-inch diameter cylinder, had height of 1 inch, and a 45° cut off the top to form a wedge shape. The Ultem plastic wedge is shown in Figure 26.

Figure 26: Ultem Wedge Projectile

The last projectile was also made from Ultem plastic and fired from an un-rifled 12-gauge barrel with a white shotgun wad. It was a rectangular brick measuring 0.52 inch by 0.48 inches by 1 inch. The Ultem rectangular brick is shown inside a 12-gauge shell in Figure 27.

Figure 27: Ultem Brick in 12 Gauge Shell

CHAPTER 4 DATA ANALYSIS

Combining all aspects of this experiment required multiple different data analysis steps. The first step was combining the timing information to find when each pulse of light occurred for each test shot. The next step was to register each camera station into a global coordinate system. After this, image subtraction algorithms were done on each image, and then the position of the projectile could be found using VIC-3D. The position data could then be converted from the camera station coordinate system into the global coordinate system. The final step was combining the global position data with the timing data for the results.

4.1.1 Timing Data

The goal of the data analysis for the timing data was to combine the timing data recorded on both oscilloscopes and then find the time when each pulse of light was emitted in the images. The first step was to get the recorded data from each oscilloscope in the same time step. One of the oscilloscopes had a recording rate of 1 GHz while the other had a recording rate of 1MHz. Python code was written and used to shrink the 1 GHz data down to the 1 MHz timestep. Both sets of timing data were manually combined in Microsoft Excel by matching the spike in voltage recorded when the projectile passed through the first IR sensor. Since the second IR sensor was recorded by both oscilloscopes as well, the spike in voltage recorded from the second sensor was used to verify that the timing information was combined correctly. The output trigger to fire the gun was set at time 0, and then the time that the voltage spiked for each IR sensor was recorded.

The time each output trigger occurred could then be calculated. The first two camera stations used dynamically delayed pulses and could be calculated using formula (7). Camera stations 3 through 6 were triggered using a delayed pulse, so the output trigger time could be calculated using the following formula:

$$t_{output} = t_{input} + t_{delay} \tag{10}$$

Camera station 7 was triggered by IR sensor 5 which was not recorded. The timing for this camera station was estimated by calculating the velocity of the projectile in the images from camera station 6 and 7 and averaging them. Using this velocity and the distance between the camera stations, the time it took for the projectile to travel between the camera stations could be calculated. This worked for approximating the times, but the timing results from camera station 7 have significantly higher error than the other stations.

The final step was to calculate when each pulse of light occurred in each image. To do this, the output trigger for the strobe light needed to be combined with the strobe light data located in Table 2. For the camera stations using the Vela One strobe light, the first pulse of light occurred 10 μs after the output trigger. The subsequent timing of each pulse of light is found by adding the time between pulses to the previous pulse time. For the camera stations using the Constellation 120E, the exact time the camera shutter opened could be found, but the exact time each pulse of light occurred could not. In the experiment, the strobe light had to be continuously run off a signal generator and was not synchronized with the camera shutter opening; therefore, there is an uncertainty of 100 μs for the timing on these camera stations. The first pulse was assumed to have happened when the camera shutter opened.

4.1.2 Camera Station Registration

The first step to registering the camera in a global coordinate system was to define the global coordinate system. This system is defined using a Cartesian Coordinate system where the origin is located at the end of the gun barrel. The x-axis is the same as the axis of the gun barrel where positive values of x are downrange of the gun barrel. From the perspective looking down the barrel of the gun, the y-axis is the vertical axis where positive values of y are located above the gun barrel. The z-axis is the horizontal axis where positive values of z are to the right of the gun barrel, and negative values are to the left. Creating the global coordinate system was done in Spatial Analyzer by using the point surveyed at the end of the barrel as the origin. The points surveyed along the gun barrel were used to create a line, and that line was used as the x-axis. A vertical survey was taken that defined the y-axis, and the coordinate system was created using these two axes and the origin at the tip of the gun barrel.

The model of the DIC tube was added at each location it was surveyed, which added the DIC tube's frame of reference into the global coordinate system. To add the DIC tube, the SMR mounting locations in the model were matched with the locations from the survey. The coordinate system of the DIC tube had an axis running along the cylinder, and another axis through the center calibration marker on the tube. The origin of this coordinate system was located at the center of the tube.

The next step was to take the camera's coordinate system for each camera station and relate it to the DIC tube's coordinate system. To do this, the speckle pattern was analyzed using VIC-3D to create an array of points along the surface of the DIC tube. The location of each calibration marker was also found. The array of points and location of the calibration markers was relative to the camera coordinate system. The analysis of the speckle pattern is shown in Figure 28.

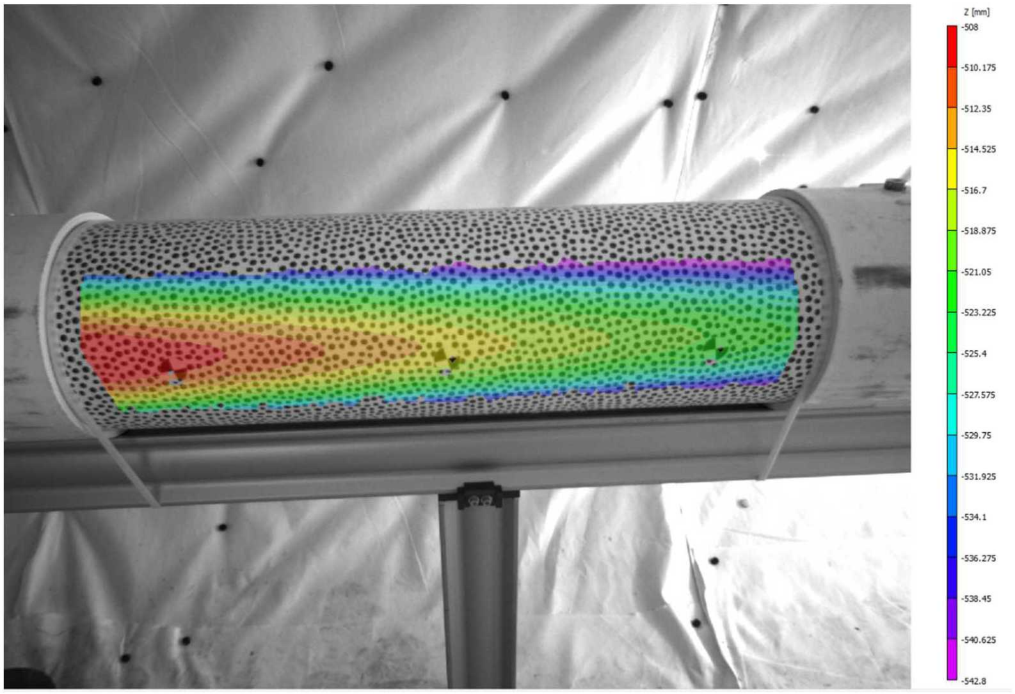

Figure 28: Speckle Pattern Analysis of DIC Tube

The array of points generated from the speckle pattern was input into Spatial Analyzer, and the center calibration marker was also added. Using the array of points, a cylinder was created, and then a centerline of the cylinder was added. The center calibration marker point was then projected onto the centerline of the cylinder. A new coordinate system frame was created using the point along the centerline of the cylinder as the origin, the centerline as the x-axis, and the line going from the origin to the center calibration marker as the z-axis. This newly created frame of reference is the same as the coordinate system of the DIC tube. The camera coordinate system could then be brought into the

Spatial Analyzer model by matching the DIC tube's frame of reference from each model. Figure 29 shows all the camera stations brought into the global frame of reference.

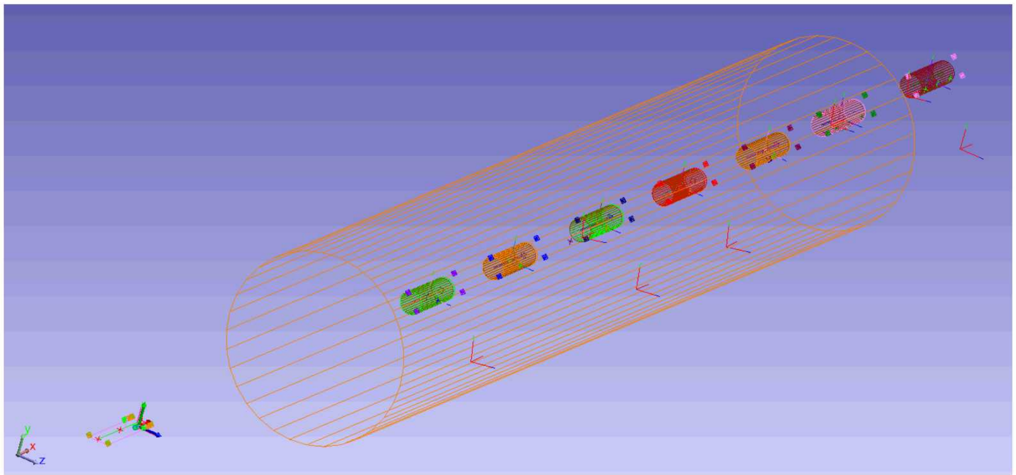

Figure 29: Camera Stations in Global Coordinate System

4.1.3 Image Processing

The images gathered during testing had a low contrast between the projectile and the background. To see the projectile in the image more clearly, an image subtraction algorithm was used. A simple algorithm subtracts the background of the image from the data image which results in changes to the image being the only thing left. A better image subtraction algorithm will highlight any changes in the image, so the following algorithm was used [30].

$$C(i,j) = \frac{((A(i,j) - B(i,j))^2}{\frac{A(i,j)+B(i,j)}{2} + 1} \tag{11}$$

In this equation, A(i,j) is the normalized matrix of your data image, B(i,j) is the normalized matrix of the background image, and C(i,j) is the processed image. Regions with no change between the data image and the background image will remain black, small changes will be highlighted, and large changes will appear white. The data processing was done using Python. Example code for the image subtraction is shown in APPENDIX A.

While running this process, it was found that the images had a high level of noise. A simple and effective approach was to take multiple background images and average them together. Random hotspots due to noise were darkened by averaging across multiple images. By reducing the noise in the background image, there were smaller changes on average between the noisy data image and the averaged background. The result was the final subtracted image had less noise. Figure 30 and Figure 31 show a data image before and after image subtraction.

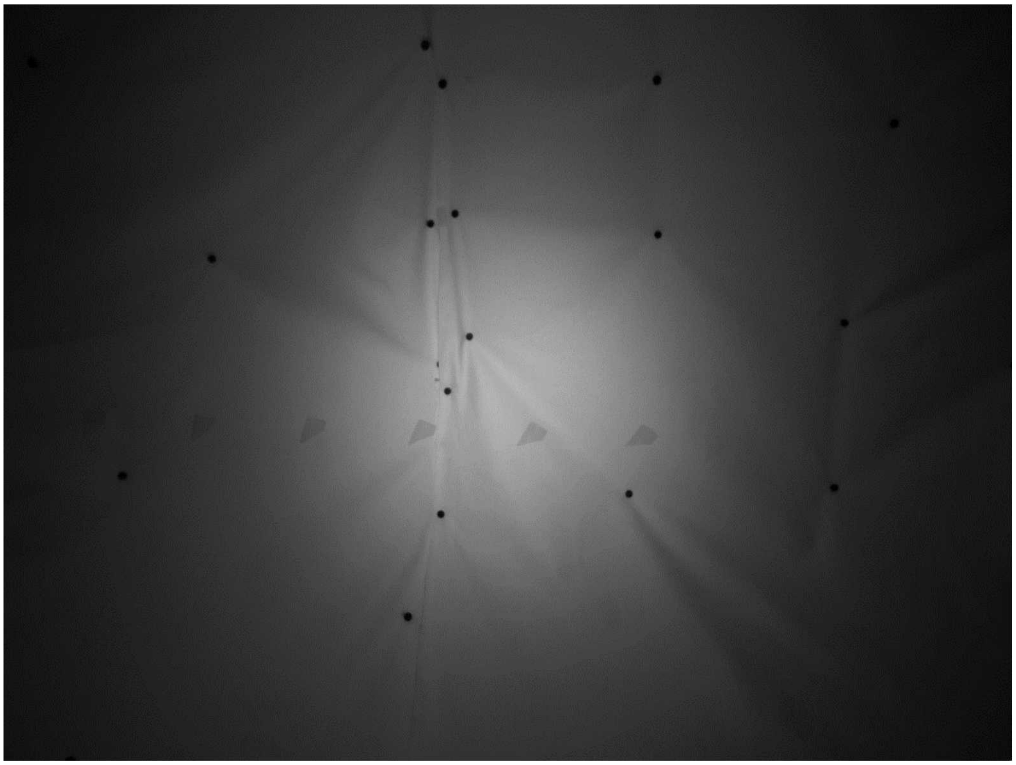

Figure 30: Camera Station 1, Lower Camera, Original Data Image

Figure 31: Camera Station 1, Lower Camera, Subtracted Image

4.1.4 Projectile Tracking

Tracking the projectile was done using VIC-3D. The processed images for the upper and lower camera stations were loaded into the software, and then markers were added on each fragment position to find the XYZ location of the projectile for each pulse of the strobe light. For the cylindrical wedge projectile shape, there was only one unique point of the projectile that could be marked as the same point for each position of the projectile in the image; that point was the tip of the wedge. Since the same points could not be chosen for ever position of the projectile, three easily identifiable points were chosen and averaged to find the approximate centroid of the projectile. An example of placing markers on the cylindrical wedge projectile is shown in Figure 32.

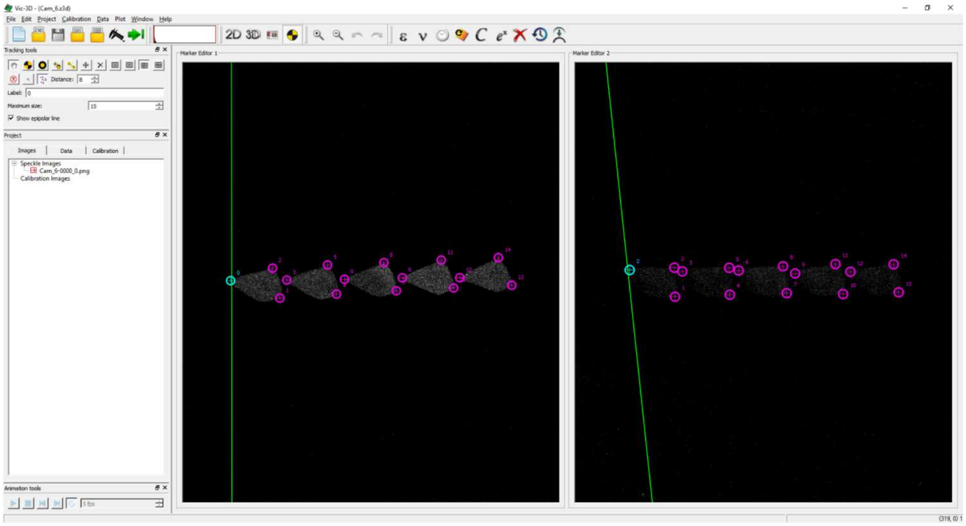

Distance: 8
Label: 0
Maximum size: 15
☑ Show epipolar line

Figure 32: Cylindrical Wedge Projectile Markers in VIC-3D

For the rectangular projectile, corners of the block were identified in the image at each camera station, but the same corner of the rectangular block could not be selected between different camera stations. Four points on the corners of the projectile were selected for each position of the projectile in the image. By selecting pairs of points that were on opposite corners, the true centroid of the projectile was found for each position. An example of placing markers on the rectangular brick projectile is shown in Figure 33.

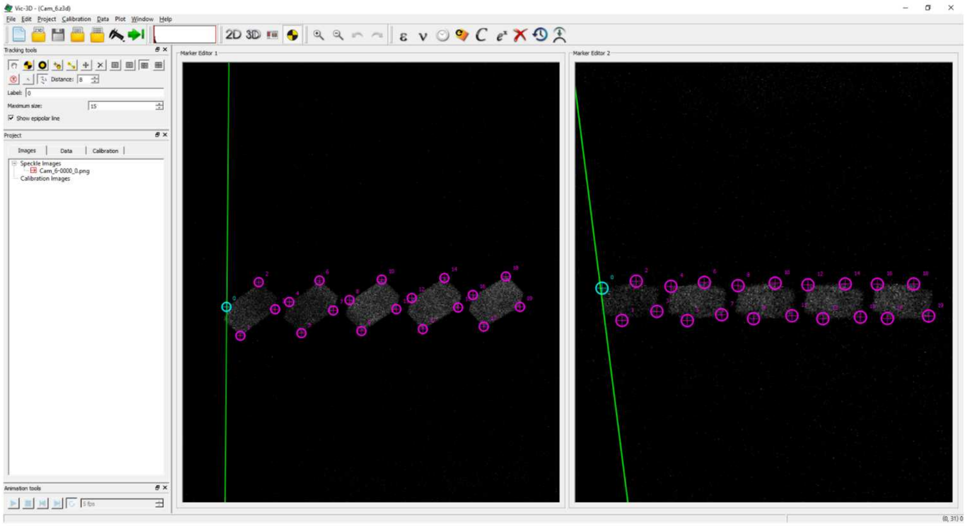

Distance: 8
Label: 0
Maximum size: 15
☑ Show epipolar line

Figure 33: Rectangular Brick Projectile Markers in VIC-3D

For some images from the camera stations using the Constellation 120E, there was not high enough resolution or contrast in the image to easily identify three points for the cylindrical wedge or four corners on the rectangular brick. For these images, only one point was selected for each position of the projectile, and the point was selected at the center of the projectile. The position data found using this technique carries a higher error than calculating the centroid of the projectile. An example of placing markers using this technique is shown in Figure 34.

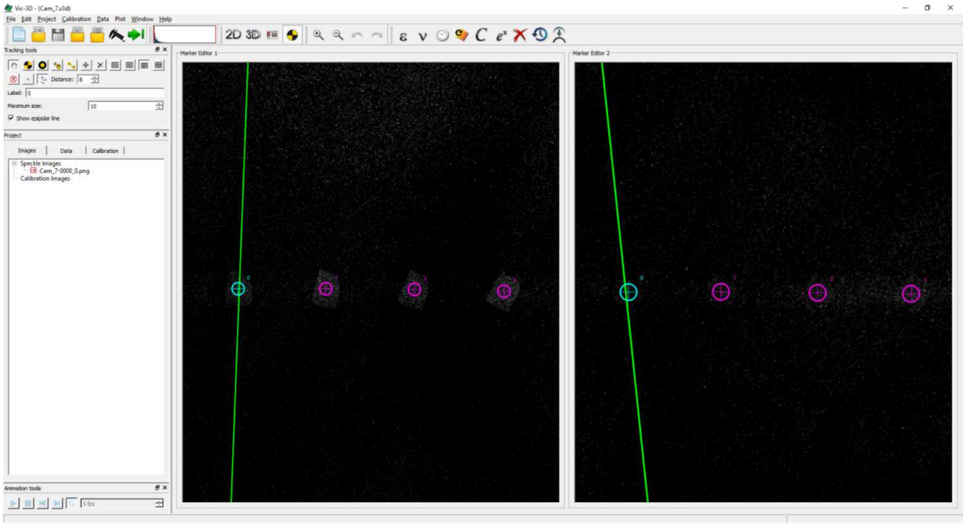

Distance: 8

Label: 0

Maximum size: 15

☑ Show epipolar line

Figure 34: Low Resolution Image Markers in VIC-3D

After the markers were placed, the XYZ position of each marker was exported from VIC-3D to an Excel file where the centroid of each position was calculated. The XYZ positions found were in the camera station's coordinate system. The projectile's positions were input into Spatial Analyzer to convert them from the camera coordinate system into the global coordinate system. Once in the global coordinate system, the position data could be combined with the timing data for the final results. Figure 35 shows the position data of shot 29 in Spatial Analyzer with camera station 1 set as the active frame of reference. The white points represent the centroid of the projectile calculated by the data images, and the cylinder represent the location of the DIC tube during the survey. Camera station 1 is shown on the left, and camera station 2 is shown on the right of the image.

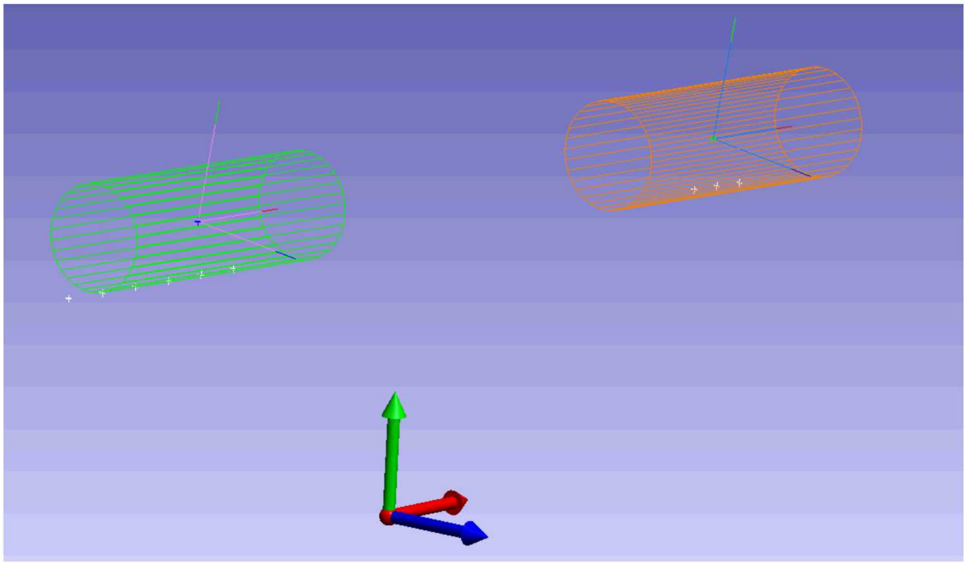

Figure 35: Shot 29 in Spatial Analyzer

CHAPTER 5 RESULTS AND DISCUSSION

The results presented are separated by test series. The results from Test Series 1 focus on comparisons between the different cameras and the different backdrops used in the testing. The results from test series 2 presents the position data found from two different types of projectiles.

5.1 Test Series 1

The results from Test Series 1 include the list of projectiles, the results and discussion for the camera selection, and the results and discussion on the backdrop selection. Additional data images from Test Series 1 can be found in APPENDIX B.

5.1.1 List of Projectiles

The list of projectiles fired is below in Table 3. The velocity shown in the list is the velocity found at the chronograph. The recorded mass is the mass of the projectile in grains. Note that for shots 17-23 no data was collected. This is due to the change to a new type of projectile which was the Ultem plastic projectile. For these shots, different amounts of black powder were used to try to achieve an initial velocity of approximately 3,000 ft/s or 914.4 m/s. After running multiple tests, the velocity of the projectile still had a wide range of initial velocities, so testing resumed using 0.308 after the 28th test.

Table 3: Test Series 1 List of Projectiles

Shot #	Projectile	Chronograph (m/s)	Mass (grains)
1	.308 copper	no data	110.0
2	.308 copper	949.76	110.0
3	.308 copper	945.49	110.0
4	.308 copper	948.23	110.0
5	.308 copper	935.43	110.0
6	.308 copper	943.97	110.0
7	.308 copper	951.28	110.0
8	.308 copper	945.49	110.0
9	.308 copper	951.28	110.0
10	.308 copper	932.38	110.0
11	.308 copper	942.44	110.0
12	.308 copper	949.76	110.0
13	.308 copper	941.22	110.0
14	.308 copper	941.22	110.0
15	.308 copper	938.17	110.0
16	7.62x39mm Ultem	706.53	11.5
17-23	7.62x39mm Ultem	no data	11.5
24	7.62x39mm Ultem	854.35	11.5
25	7.62x39mm Ultem	814.73	11.5
26	7.62x39mm Ultem	812.6	11.5
27	7.62x39mm Ultem	762.91	11.5
28	7.62x39mm Ultem	907.69	11.5

29	.308 copper	938.17	110.0
30	.308 copper	948.23	110.0
31	.308 copper	942.44	110.0
32	.308 copper	908.91	110.0
33	.308 copper	926.9	110.0
34	.308 copper	932.38	110.0
35	.308 copper	929.64	110.0
36	.308 copper	928.12	110.0
37	.308 copper	932.38	110.0
38	.308 copper	922.63	110.0
39	.308 copper	928.12	110.0
40	.308 copper	928.12	110.0
41	.308 copper	922.63	110.0
42	.308 copper	931.16	110.0
43	.308 copper	926.9	110.0

5.1.2 Camera Selection

The images from shot 30 for each camera are shown below in Figure 36 through Figure 39. For the two USB Grasshopper cameras at camera station 1, both cameras were configured with the same shutter time, camera gain, and f-stop on the lens. The values of the pixels on the white canvas backdrop were compared, and the GS3-U3-28S5M-C had higher values than the GS3-U3-32S4M-C. The gain was increased on the GS3-U3-32S4M-C camera to get usable locations of the bullet and match the white pixel values from the GS3-U3-28S5M-C. This resulted in increased noise throughout the image making it harder to accurately determine the locations of the bullet in each shot. The Grasshopper Express GX-FW-60S6M-C camera had a similar signal when compared with the GS3-U3-32S4M-C when both cameras had the same values for shutter time, gain, and f-stop of the lens. Since both cameras had similar signal, the cost of the camera was the determining factor. The GS3-U3-32S4M-C was twice the cost compared to the FW-60S6M-C, so the GS3-U3-32S4M-C was selected to be used in Test Series 2.

Figure 36: Camera Station 1, GS3-U3-28S5M-C, Shot 30

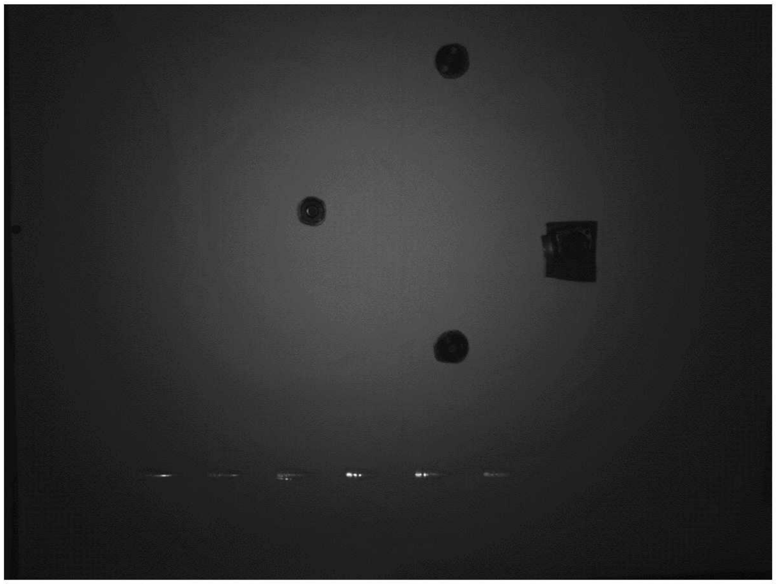

Figure 37: Camera Station 1, GS3-U3-32S4M-C, Shot 30

Figure 38: Camera Station 2, Lower GX-FW-60S6M-C, Shot 30

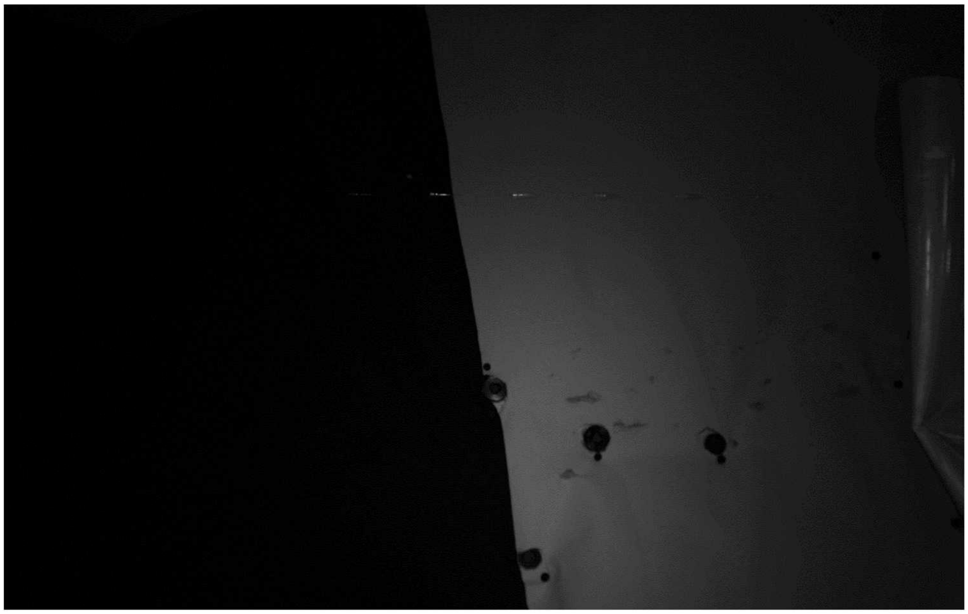

Figure 39: Camera Station 2, Upper GX-FW-60S6M-C, Shot 30

5.1.3 Backdrop Selection

The three different types of backdrop where used, which was a white reflective screen, flat black canvas, and flat white canvas. The reflective screen was only used for the first eight tests, and then was swapped out for flat white canvas. The reflective screen had multiple hotspots that overexposed the camera imager. The hotspots were created from the strobe light reflecting directly into the camera. Occasionally, the position of the projectile would be aligned with one of the hotspots, and part of the position data would be lost. Figure 40 shows a 0.308 transitioning form the black canvas to the white reflective material, and it also shows part of the bullet inside one of the hotspots. During testing, the reflective screen was taken down after eight tests because of these hotspots. It was replaced with flat white canvas instead.

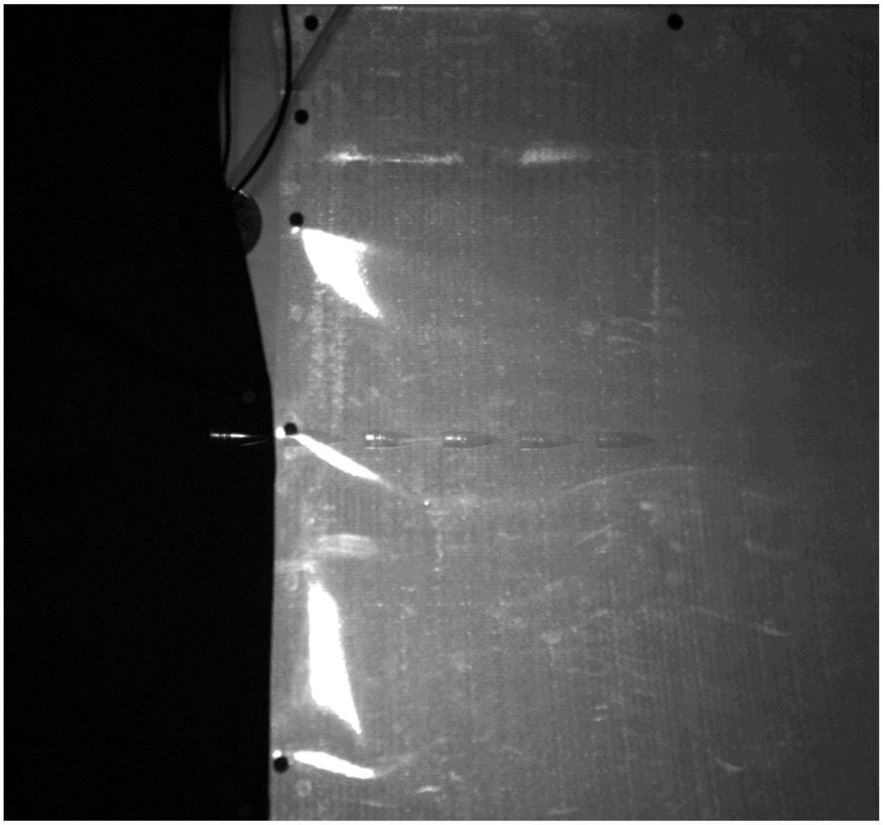

Figure 40: Camera Station 2, Black Canvas and Reflective Screen

For the first eight tests, flat black canvas was used at camera station 1 to ensure that the background would not be overexposed from the strobe light pulses; however, not enough light was reflected from the projectile back into the camera sensor to accurately find any position data. For these tests, the projectile was a cylindrical shape with high reflectivity. Enough light was reflected off the center of projectile to overexpose the camera for a few positions of the projectile. Since the projectile was a cylinder, light was reflected away from the camera the farther away from the center of the cylinder the light hit. Under these circumstances, the edges of the projectile are impossible to detect using a black backdrop. Figure 41 shows camera station 1 with the black canvas backdrop.

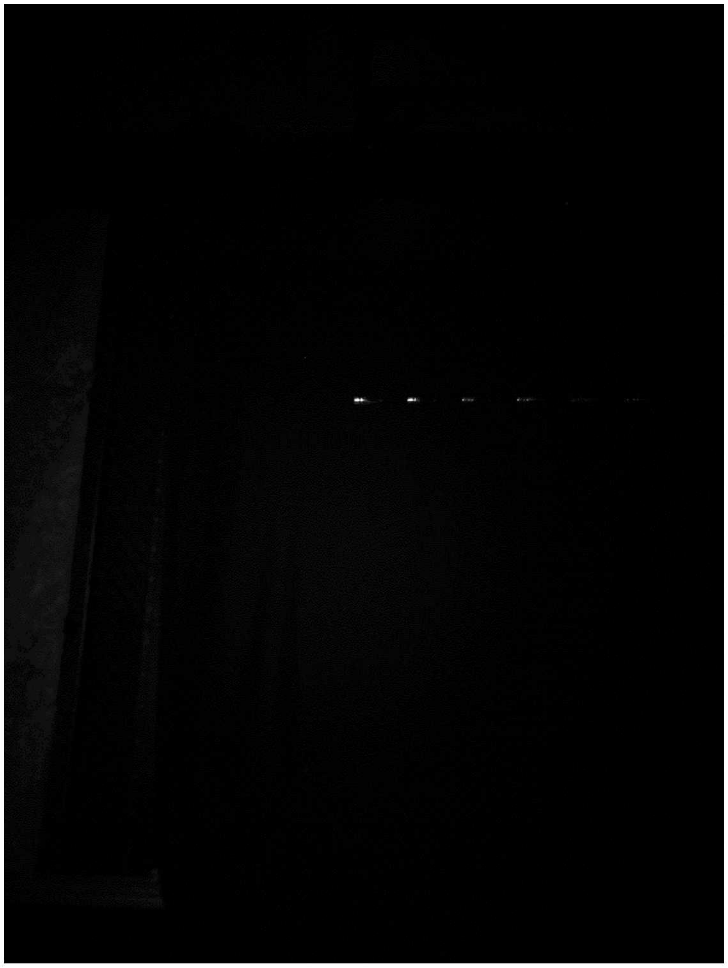

Figure 41: Camera Station 1, Flat Black Canvas Backdrop

After the first eight tests, a flat white canvas backdrop replaced the black canvas at camera station 1 and the reflective screen at camera station 2. With a white backdrop, the effect of the stroboscopic imaging changed. Instead of the light reflecting off the object as it moved to different positions when the strobe light pulsed, now the object was blocking the light reflecting from the white backdrop when the strobe light pulsed. This created a darker area that defined the edges of the projectile, and the center of the projectile still overexposed some pixels when the light reflected off the center of the cylinder.

Figure 42 shows the data collected from camera station 1 on test 33. All six outlines of the projectile are visible unlike the data gathered when using the black canvas, and the last two positions of the projectile have overexposed pixels at the center of the projectile. Figure 43 shows the images from camera station 2 on test 33. The black canvas was used for the first half of the image, and white canvas was used in the second half. The same results were seen where the outline of the projectile could not be found for positions in front of the black canvas, but they could be found when located in front of the white canvas. For these reasons, flat white canvas was chosen to be used for Test Series 2.

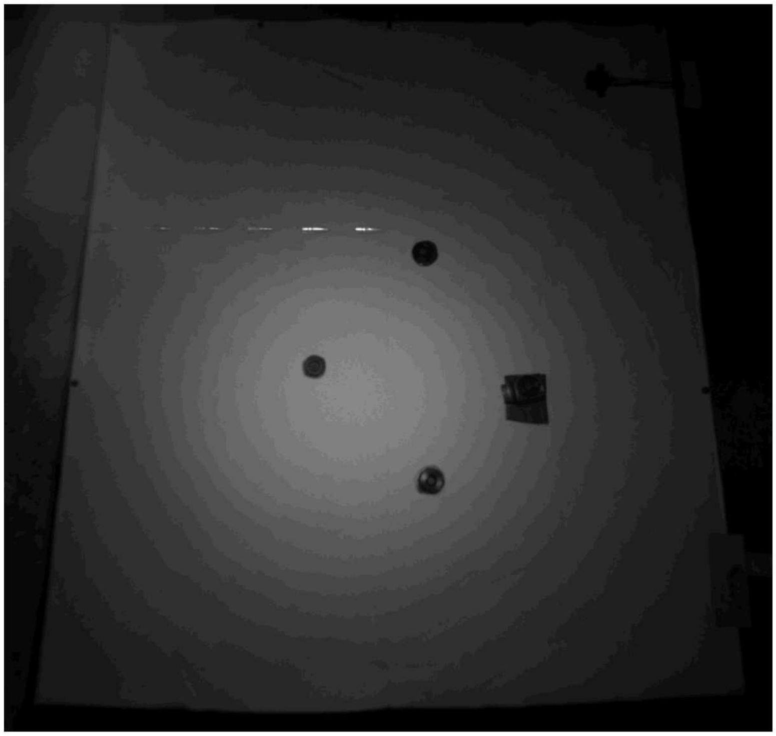

Figure 42: Camera Station 1, Flat White Canvas Backdrop

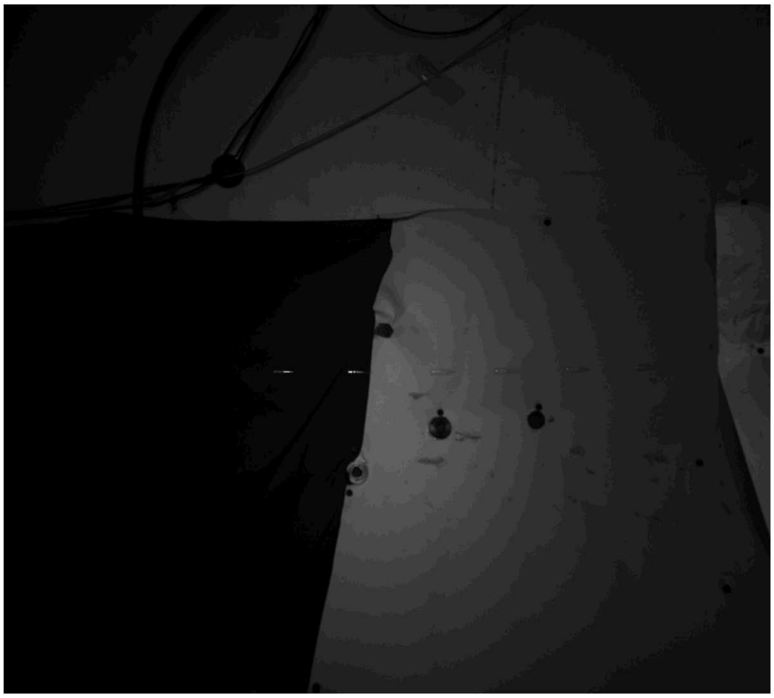

Figure 43: Camera Station 2, Flat Black and White Canvas Backdrop

5.2 Test Series 2

The results from Test Series 2 include the list of projectiles, discussion on sources of error in the results, and the position data and linear velocity for the cylindrical wedge and rectangular brick. Additional images from the testing can be found in APPENDIX C.

5.2.1 List of Projectiles

Table 4 shows the list of projectiles that were recorded for Test Series 2. Since a large portion of this test series was spent ringing out the system, data was only recorded for shot 23 to shot 37. These shots were all taken the morning of September 1, 2017. The mass of each projectile is recorded in grains. The velocity of the projectile seen at the chronograph is recorded in m/s. The chronograph did not record data for three of the rectangular brick projectiles because the chronograph IR sensors did not trigger on those shots. The columns labeled dY and dZ represent the impact location of the projectile. These values were measured from the centerline of the barrel as measured with the bore laser to the center of the impact of the projectile. For some projectiles, the impact location could not be found so information was not recorded.

Table 4: Test Series 2 List of Projectiles

Shot #	Projectile	Mass (grain)	Chronograph (m/s)	Impact Y (mm)	Impact Z (mm)
23	45° Ultem Wedge	87.6	996.09	-54.54	-131.8
24	45° Ultem Wedge	88.5	983.28	-4.364	148.5
25	45° Ultem Wedge	90.7	943.66	No Data	No Data

26	45° Ultem Wedge	86.2	960.12	-143.5	-242.7
27	45° Ultem Wedge	86.2	936.35	-91.4	113.5
28	45° Ultem Wedge	86.1	903.12	204	276
29	45° Ultem Wedge	91.2	908.61	92.3	-24
30	45° Ultem Wedge	90.7	905.87	-170.1	29.9
31	45° Ultem Wedge	94.3	907.08	-272.6	-24.9
32	Ultem Rectangular Block	84.4	729.08	No Data	No Data
33	Ultem Rectangular Block	86.3	869.59	-175.8	144.8
34	Ultem Rectangular Block	78.7	No Data	No Data	No Data
35	Ultem Rectangular Block	77.8	No Data	No Data	No Data
36	Ultem Rectangular Block	78.5	766.57	-215.2	-10.3
37	Ultem Rectangular Block	75.8	No Data	No Data	No Data

5.2.2 Error

A source for error in Test Series 2 was movement in the camera stations after the calibration had been taken. For most of the camera stations, evidence is found in the image produced by the image subtraction process that the cameras moved a small amount. This is seen in the white outline around the neodymium magnets that were holding up the white canvas backdrop. For the background image used in the image subtraction process, multiple background images were averaged, and these background images were all taken after the camera station calibration. The magnets holding the backdrop should have remained stationary during testing, yet the image subtraction highlights those pixels as having changed. Figure 44 shows the product of image subtraction for one of the rectangular brick projectiles. The large white area on the left of the image is from changes to the black curtain that was used protect the IR sensor from the strobe light pulses. On some shots, the curtain was torn down by the projectiles and it was not replaced in the same location each time. The outline of white circles scattered throughout the rest of the image are the outlines of the magnets. In the figure, each of the magnets has three highlighted pixels in the vertical axis with respect to the camera station coordinate system but does not have any highlighted pixels in the horizontal axis. This represents approximately 1.73 mm of error in the vertical axis from this camera view.

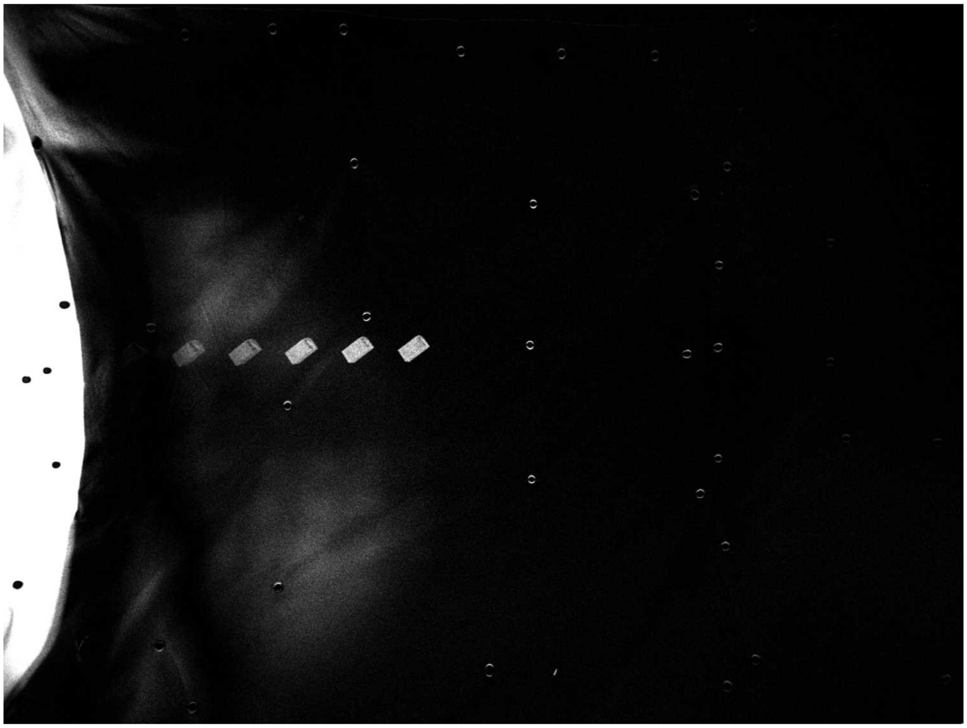

Figure 44: Image Subtraction, Camera Station 5, Lower Camera

Another source of error was noticed in Spatial Analyzer for camera station 7. After each station was registered and brought into Spatial Analyzer, the registration was verified by examining images collected from a ring out shot using a rifled 0.308 round. The assumption was that the 0.308 round would fly along the axis of the barrel without any deviations, though there should be a negative 2 to 3 mm change in the Y direction due to gravity. The tip of the position data of the tip of the bullet was found and then input into Spatial Analyzer. These points were compared to the axis of the barrel. Camera station 7 had a significant deviation from the centerline.

To fix this camera station, a correction was made using VIC-3D. In the images of the DIC tube that were used relate the camera station coordinate system to the coordinate system of the DIC tube, the length of the DIC tube was measured and found to be incorrect. The length was updated in the software which adjusted extrinsic values of the camera station, and then the DIC tube was reanalyzed according to the procedures in 4.1.2. The new camera station coordinate system was input into Spatial Analyzer. Figure 45 shows the XY plane of the original DIC tube, in blue, and the updated DIC tube, in maroon. This correction fixed the data for the 0.308 round.

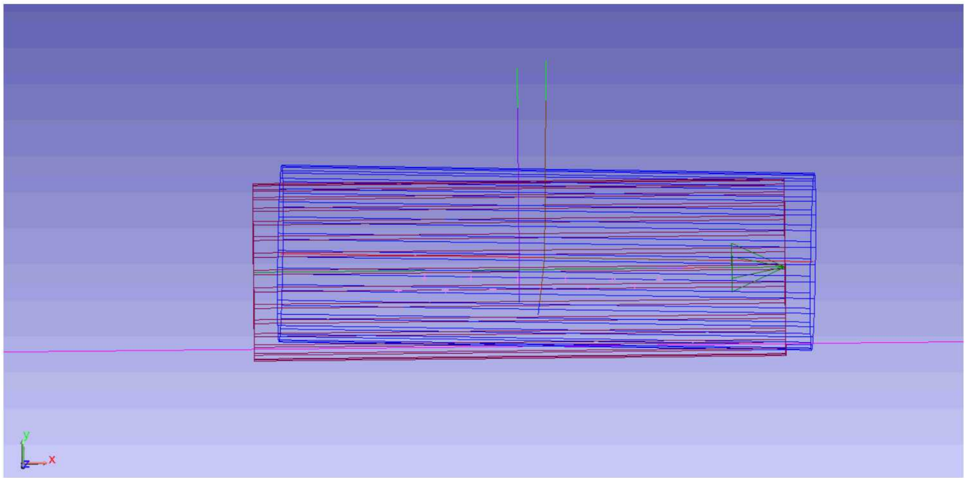

Figure 45: Camera Station 7, Correction in XY plane

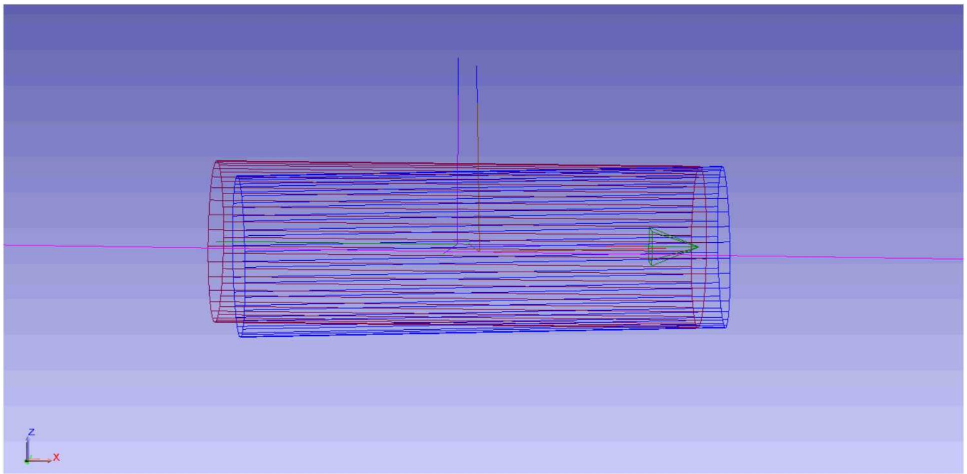

Figure 46: Camera Station 7, Correction in XZ Plane

The source of the registration error is unknown. The most likely explanation is that the camera station was bumped by personnel and therefore it moved more significantly than the other camera stations between tests. Another explanation could be that the registration data for the DIC tube had some inaccuracies. Camera station 7 was located the farthest from the gun barrel where the API laser tracker was set up, and the error of the tracker increases with distance. Since the source of the error is unknown, camera station 7 may have higher error than the other camera stations.

5.2.3 45° Cylindrical Wedge Results

The position data was combined with the timing data to find the velocity and position X, Y, and Z with respect to time. The results from shots 24 to 26, and shots 28 to 31 are present below in Figure 47 through Figure 50. In all but a few cases, second order polynomial best fit trendlines were used to show the trend of each shot. Third order polynomial trendlines were used for shot 26 in Figure 49 and Figure 50 because a second order trendline did not match the data. The velocity that was calculated between each camera station was omitted since it was an average of the velocities between the stations. The first point for the velocity (at approximately .005 seconds) represents the velocity calculated at the chronograph. Shot 27 is not shown in the graphs because global timing data was not recorded for that shot. The timing between strobe pulses was known, so the velocity could be calculated at each station. Table 5 shows the position data and the calculated velocity for shot 27.

There was a significant decrease in velocity for every projectile. As an approximation, each projectile was at 60% of its initial velocity when it reached the 7th camera station. The projectiles had an even spread in the Y direction where half of the projectiles had positive Y values. The projectiles would have a displacement of negative 3 mm in the Y direction from the effects of gravity. The projectiles had a similar magnitude of potential displacement in the Y and Z directions, which was around 200 mm.

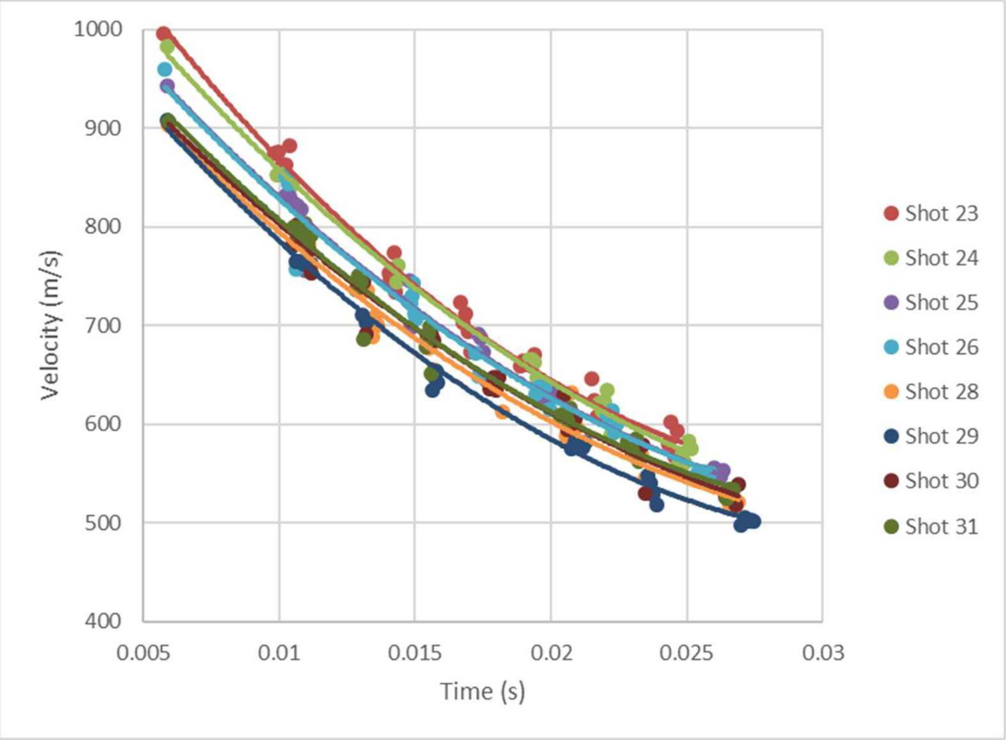

Figure 47: 45° Cylindrical Wedge Velocity Vs. Time

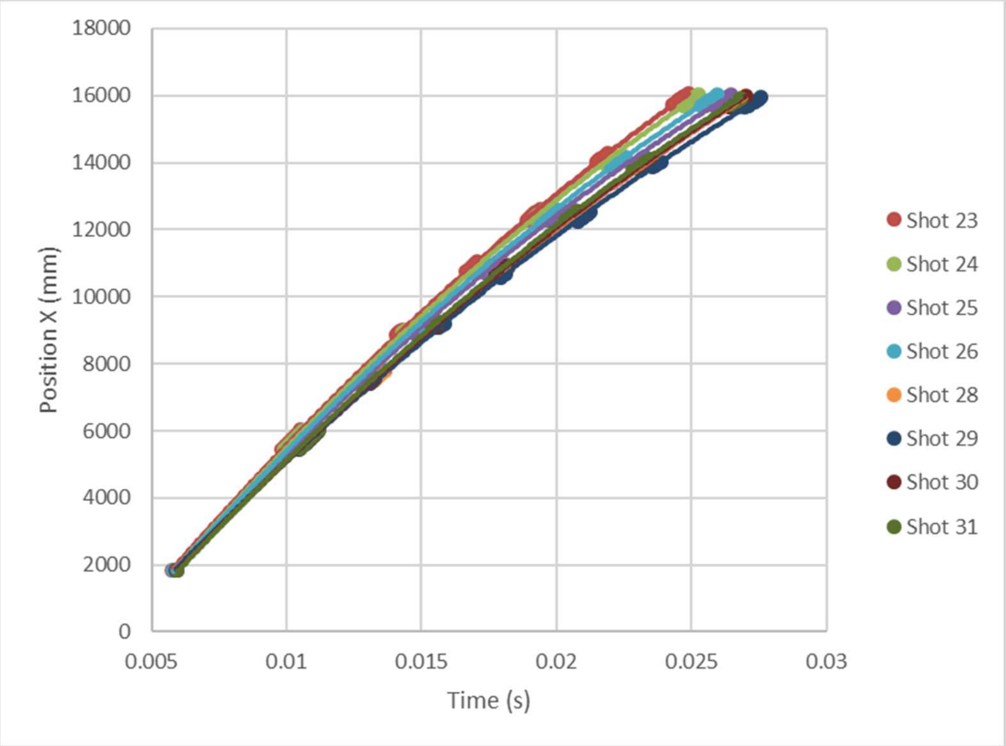

Figure 48: 45° Cylindrical Wedge Position X Vs. Time

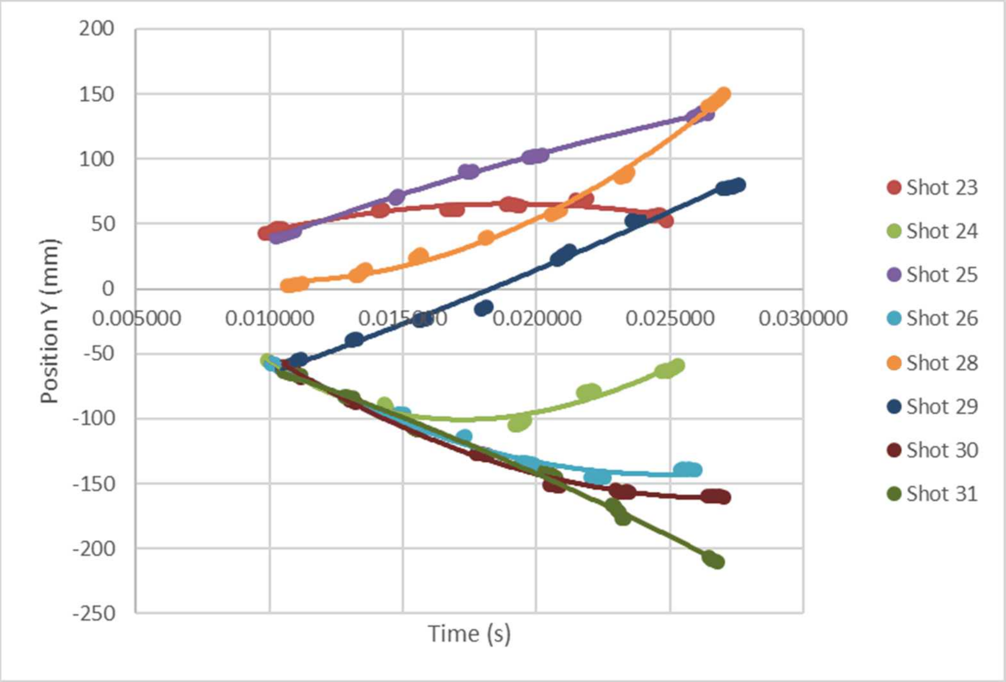

Figure 49: 45° Cylindrical Wedge Position Y Vs. Time

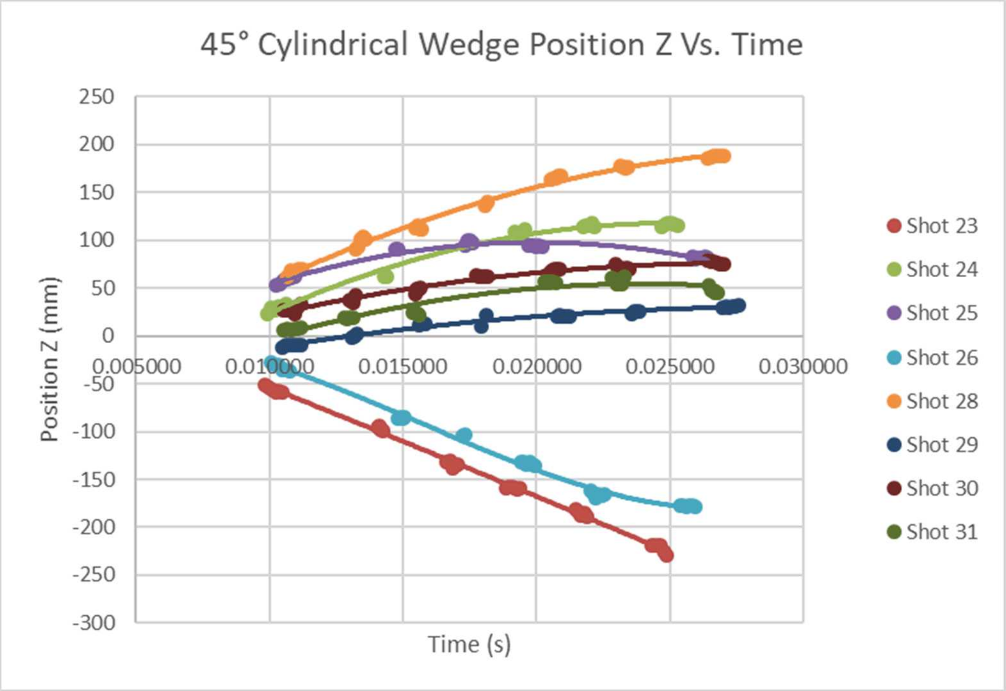

Figure 50: 45° Cylindrical Wedge Position Z Vs. Time

Table 5: Test Series 2, Shot 27, Cylindrical Wedge Data

Camera Station	X (mm)	Y (mm)	Z (mm)	Velocity (m/s)
1	5478.891	-52.403	27.956	803.71
	5588.149	-51.890	24.800	831.79
	5701.215	-52.892	28.253	819.70
	5812.680	-53.576	29.881	815.77
	5923.585	-54.292	32.751	810.54
	6033.816	-54.232	33.407	n/a
3	9119.100	-85.918	65.914	681.17
	9154.454	-86.276	63.769	702.13
	9190.960	-86.845	63.549	713.96
	9228.042	-87.176	61.785	781.46
	9268.672	-87.782	61.418	n/a
4	-3379.215	-501.629	-529.789	670.16
	-3312.334	-502.975	-533.807	662.26
	-3246.188	-504.792	-536.518	662.88
	-3179.941	-507.023	-537.137	n/a
5	12329.446	-121.233	89.919	552.09
	12384.645	-122.272	89.839	620.35
	12446.671	-123.336	90.036	636.51
	12510.277	-122.519	92.275	616.89
	12571.885	-121.388	95.241	n/a
6	-179.607	-582.225	-616.904	594.37
	-120.216	-583.149	-619.064	589.96
	-61.276	-583.926	-621.502	590.06

	-2.323	-584.705	-623.879	599.70
	57.645	-585.104	-623.535	n/a
7	15694.528	-123.906	100.340	545.10
	15758.183	-123.185	99.294	561.91
	15823.801	-123.684	98.059	564.82
	15889.647	-124.108	94.018	554.47
	15954.402	-124.505	94.893	548.84
	16018.502	-124.119	94.228	n/a

5.2.4 Rectangular Brick Results

The results from shot 33 and shot 26 are shown in Figure 51 to Figure 54. A second order polynomial best fit line was used for Figure 51 and Figure 52, and a third order polynomial best fit line was used for Figure 53 Figure 54. For shot 32, the projectile passed through the chronograph and traveled in the negative Y direction and positive Z direction. The IR sensors detected the projectile and triggered the camera stations, but the projectile was not in the FOV of the cameras, so no position data was found. For shot 34, 36, and 37, the chronograph did not work correctly. Since camera stations 1 and 2 were triggered from the chronograph, neither station was triggered for any of these shots. Without the timing data from the chronograph, it was impossible to put the other camera stations into global time. The data from these shots is shown in Table 6 to Table 8.

The trajectory of the rectangular brick had noticeable oscillations in direction between camera stations compared to the cylindrical wedge. A good example of this was the position Z versus time graph for shot 33 where the overall trajectory moved in the positive Z direction, but there appears to be an oscillation in the data between camera stations. There was also a higher amount of unpredictability to the trajectory. In two cases, there were large jumps in the position data between camera stations. The first case was in shot 34 in the Y direction. In camera station 3 and 4, the projectile is moving in the negative Y direction. In camera station 5, there is a small change in the positive Y direction. In camera station 7, there is a significant increase in the value of Y. The other case is shot 37 in the Z direction. At the first recorded station, the projectile is approximately 64 mm right of the centerline. At the next recorded station, the projectile has oscillated to the left and is approximately 55 mm right of the centerline. In camera station 7, the projectile has oscillated back to the right and is 87 mm right of the centerline.

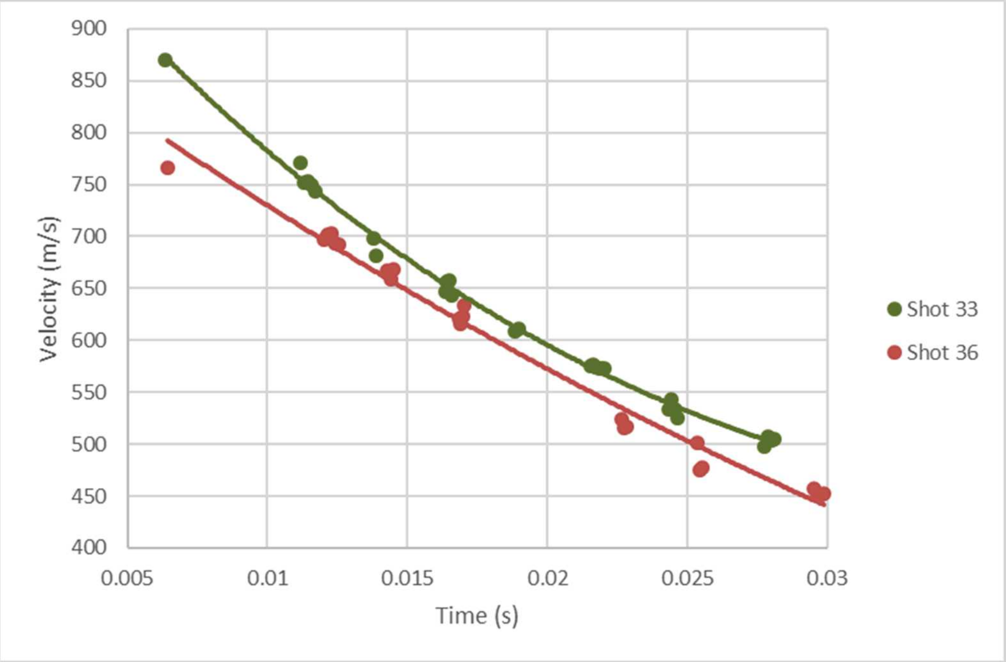

Figure 51: Rectangular Brick Velocity Vs. Time

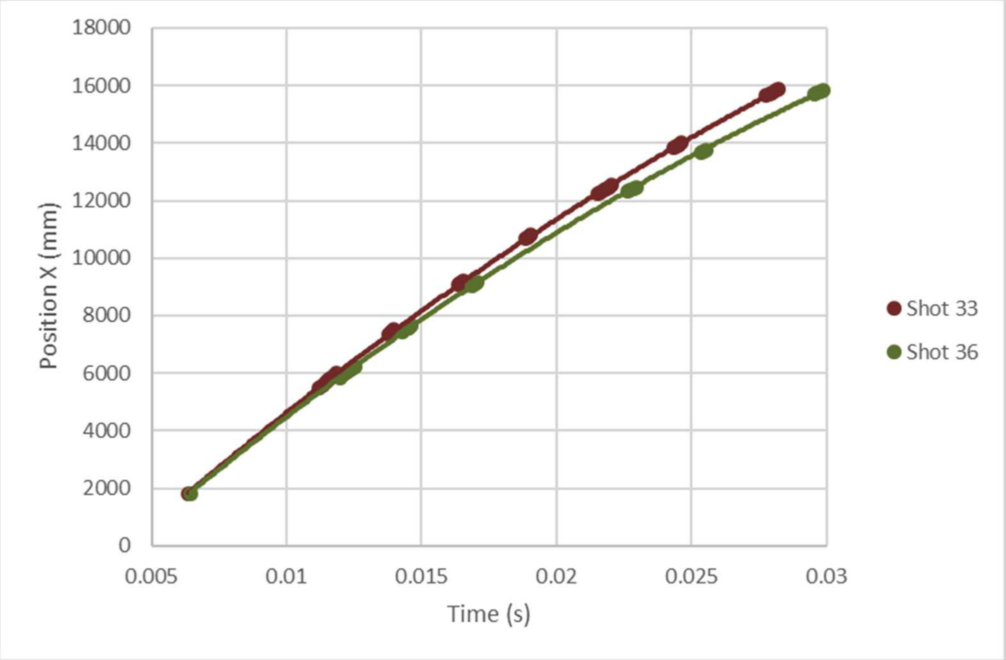

Figure 52: Rectangular Brick Position X Vs. Time

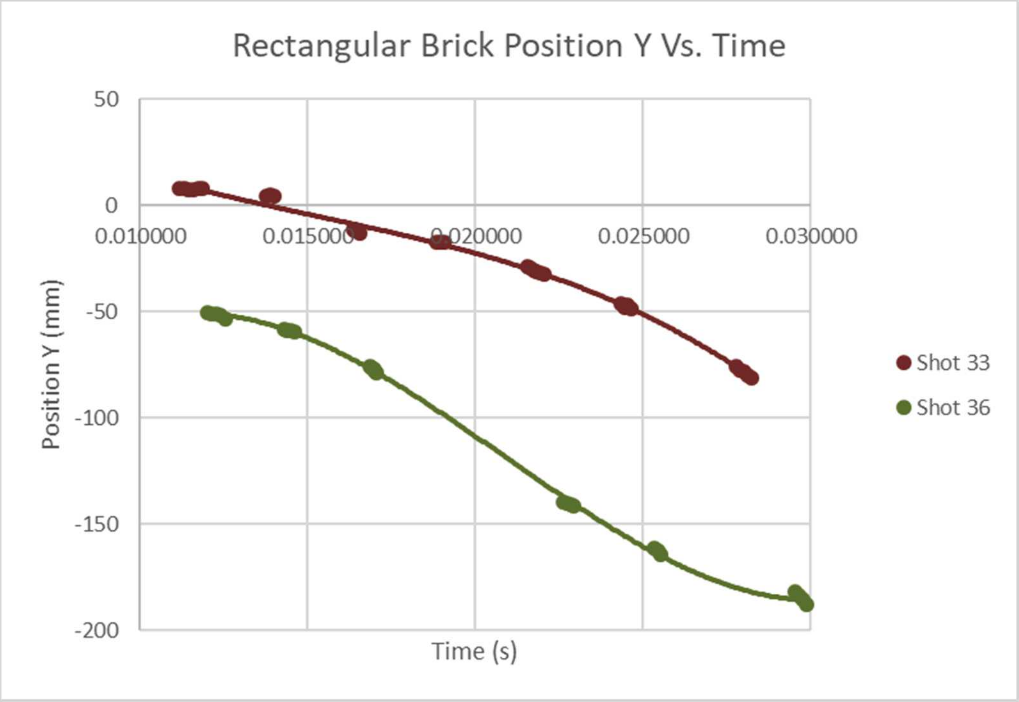

Figure 53: Rectangular Brick Position Y Vs. Time

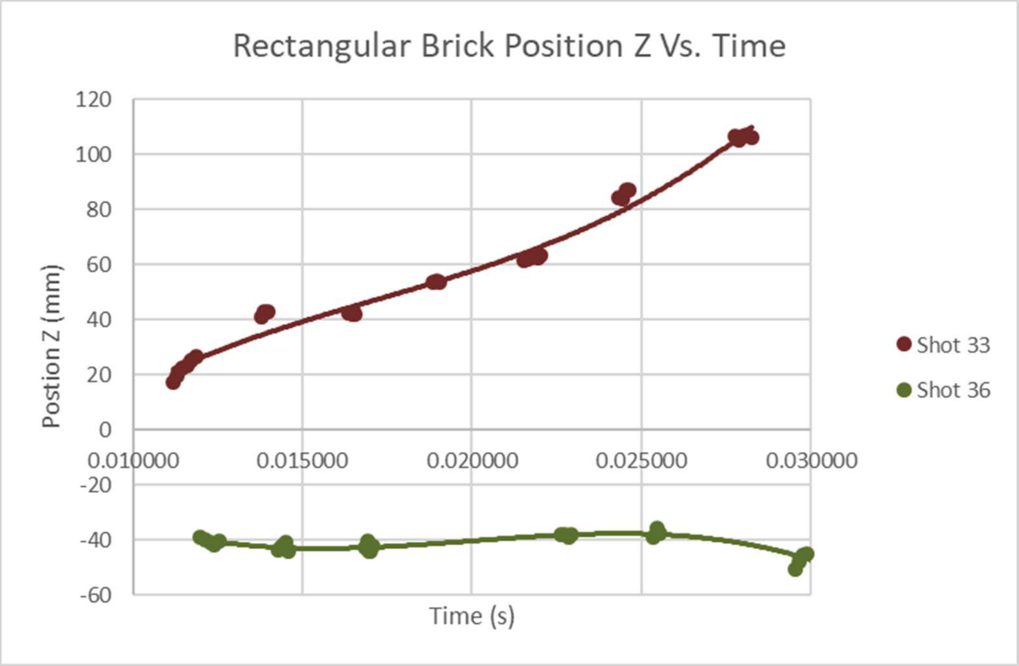

Figure 54: Rectangular Brick Position Z Vs. Time

Table 6: Test Series 2, Shot 34, Rectangular Brick Data

Camera Station	X (mm)	Y (mm)	Z (mm)	Velocity (m/s)
3	9041.368	-75.579	26.007	605.21
	9072.829	-75.634	26.816	612.33
	9104.669	-75.832	26.742	620.29
	9136.921	-75.983	27.202	609.11
	9168.595	-75.973	27.196	n/a
4	10629.130	-82.321	56.691	562.99
	10685.428	-82.635	56.470	n/a
5	12376.498	-76.239	95.493	528.72
	12429.364	-75.556	95.904	527.48
	12482.094	-74.680	96.963	n/a
7	15667.817	1.422	187.040	467.94
	15722.405	3.019	189.223	462.09
	15776.359	4.377	188.955	461.58
	15830.173	6.784	191.156	461.79
	15884.069	8.368	192.532	n/a

Table 7: Test Series 2, Shot 35, Rectangular Brick Data

Camera Station	X (mm)	Y (mm)	Z (mm)	Velocity (m/s)
3	8999.279	-11.950	27.621	545.76
	9027.655	-11.497	27.783	585.66
	9058.108	-11.648	27.943	559.34
	9087.190	-11.307	27.658	568.23
	9116.731	-11.569	28.265	n/a
5	12251.997	-28.683	69.696	498.47
	12301.821	-29.457	71.005	496.45
	12351.463	-29.635	71.582	498.43
	12401.081	-30.652	76.201	493.07
	12450.379	-31.270	76.921	n/a
7	15611.423	-43.395	104.164	403.89
	15658.510	-44.751	106.678	436.37
	15709.394	-45.989	109.332	435.14
	15760.114	-47.514	112.202	433.08
	15810.638	-48.106	114.609	430.56
	15860.832	-49.498	117.374	n /a

Table 8: Test Series 2, Shot 37, Rectangular Brick Data

Camera Station	X (mm)	Y (mm)	Z (mm)	Velocity (m/s)
3	9026.471	49.2577	63.29394	591.93
	9057.215	48.20724	64.35736	636.70
	9090.316	47.83009	64.96643	575.14
	9120.221	48.09736	65.20181	590.72
	9150.923	47.48807	64.42667	n/a
5	12212.5	10.34851	53.9921	514.00
	12263.9	10.14009	54.77157	504.62
	12314.35	9.97922	53.93459	513.10
	12365.64	9.730224	55.2946	512.28
	12416.87	9.745583	55.72785	511.41
	12468	9.628357	56.73573	n/a
7	15592.01	65.95054	87.29795	431.13
	15642.35	67.19523	87.92846	439.87
	15693.7	68.19666	86.84016	442.51
	15745.37	68.51972	88.38689	436.91
	15796.38	69.42923	87.35232	433.41
	15846.97	71.0411	87.75738	n/a

CHAPTER 6 CONCLUSION AND RECOMMENDATIONS

The experiments showed that three-dimensional position data of high-speed projectiles can be captured using off-the-shelf commercial equipment with a quick turnaround between shots. In Test Series 1, the best camera was found to be the camera that could get the highest amount of signal. The best backdrop was the flat white canvas which created a ghost of the projectile for each strobe pulse. The centroid of the projectile was used to calculate the linear velocity, and the centroid was approximated for the cylindrical wedge or in cases of low resolution images. Uniquely identifiable markers are needed on the projectile to find the rotational velocity.

While this study produced reasonable results, a few steps could be taken to yield better results for future tests. First, a more rigid mounting system should be used for the camera stations to ensure there is no motion in the camera station after calibration. The system used for this experiment was intended to be set up in less than a week, but a more permanent system should yield more accurate results. Due to the unpredictable location of the projectile, the strobe light used should have a wide beam angle. The position of some projectiles could not be found in the camera stations using the Constellation 120E strobe light as it had a smaller beam angle than the Vela One. If points on the projectile are uniquely identifiable, the rotational velocity of the projectile can be found, so the shape of the projectile should be carefully chosen. Lastly, multiple background images should be taken before each shot is fired. By having multiple background images, the image subtraction process should produce better results.

REFERENCES

[1] W. C. Nelson, Selected Topics on ballistics. London: Pergamon Pr., 1959.

[2] G. Gubinelli, S. Zanelli, and V. Cozzani, “A simplified model for the assessment of the impact probability of fragments,” *Journal of Hazardous Materials*, pp. 175–187, 2004.

[3] R. H. Fowler, E. G. Gallop, C. N. H. Lock, and H. W. Richmond, “X. The Aerodynamics of a Spinning Shell,” Philos. Trans. R. Soc., London, publication, 1921.

[4] R. L. Mccoy, “The Effect of Yaw Cards on the Pitching and Yawing Motion of Symmetric Projectiles,” Jan. 1992.

[5] T. N. Canning, A. Seiff, and C. S. James, “Ballistic - Range Technology,” National Technical Information Service, Springfield, Va, publication, 1970.

[6] W. C. Lyons, “Capability of NOL Ballistics Ranges for Obtaining Sphere Drag Coefficient Data,” United States, tech., 1969.

[7] F. Seiler and O. Igra, Hypervelocity Launchers. Cham: Springer, 2016.

[8] B. S. Davis, B. J. Guidos, and T. E. Harkins, “Complementary Roles of Spark Range and Onboard Free-Flight Measurements for Projectile Development,” Army Research Laboratory, Aberdeen Proving Ground, MD, tech., 2009.

[9] C. R. Ranawake, “The Automation of the Transonic Experimental Facility (TEF) and the Aerodynamic Experimental Facility (AEF),” Jan. 2015.

[10] C. Theobalt, I. Albrecht, J. Haber, M. Magnor, and H.-P. Seidel, “Pitching a baseball,” *ACM SIGGRAPH 2004 Papers on - SIGGRAPH 04*, 2004.

[11] “How to Evaluate Camera Sensitivity,” *FLIR*. [Online]. Available: https://www.ptgrey.com/white-paper/id/10912. [Accessed: 20-Jul-2018].

[12] B. E. Bayer, “Color Imaging Array,” 20-Jul-1976.

[13] K.-H. Chung and Y.-H. Chan, “Color Demosaicing Using Variance of Color Differences,” *IEEE Transactions on Image Processing*, vol. 15, no. 10, pp. 2944–2955, 2006.

[14] M. Hargather, “Camera Basics,” in *High-Speed Digital Imaging Techniques for Blast and Impact Measurement*, 19-Jun-2017.

[15] W. J. Smith, Modern optical engineering: the design of optical systems. New York: McGraw Hill, 2000.

[16] D. B. Frantz, Depth of Field Illustration. 2010.

[17] Y. Nishiyama, “Mathematics of Fans,” International Joural of Pure and Applied Mathematics, vol. 78, no. 5, pp. 669–678, 2012.

[18] F. V. Veen, Handbook of stroboscopy. Concord, MA: General Radio, 1977.

[19] R. Blanc and E. Giacometti, “Infrared stroboscopy—a method for the study of thermomechanical behaviour of materials and structures at high rates of strain,” International Journal of Solids and Structures, vol. 17, no. 5, pp. 531–540, 1981.

[20] D. J. Finlay and P. C. Dodwell, “Speed of apparent motion and the wagon-wheel effect,” Perception & Psychophysics, vol. 41, no. 1, pp. 29–34, 1987.

[21] “Time Filter Technical Explanation,” Tessive. [Online]. Available: http://tessive.com/time-filter-technical-explanation. [Accessed: 21-Jul-2018].

[22] Ford, T. (2018). How to Shoot Stroboscopic Flash Photos. [online] Tim Ford Photography & Videography. Available at: https://timfordphoto.com/how-to-shoot-stroboscopic-flash-photos/ [Accessed 21 Jul. 2018].

[23] Hartley, Richard, and Andrew Zisserman. Multiple View Geometry in Computer Vision. Cambridge University Press, 2017.

[24] Solem, Jan Erik. Programming Computer Vision with Python. OReilly, 2012.

[25] G. Bradski and A. Kaehler, Learning OpenCV. OReilly Media, 2015.

[26] Schreier, Hubert, et al. Image Correlation for Shape, Motion and Deformation Measurements: Basic Concepts, Theory and Applications. Springer-Verlag US, 2009.

[27] A. Nordmann, Epipolar Geometry. 2007.

[28] Szeliski, Richard. Computer Vision Algorithms and Applications. Springer, 2011.

[29] K. Simek, “Sightations ← A Computer Vision Blog,” Sightations. [Online]. Available: http://ksimek.github.io/2013/08/13/intrinsic/. [Accessed: 22-Jul-2018].

[30] M. Hargather, “Image Processing 2: Image Subtraction and Correlation,” in High-Speed Digital Imaging Techniques for Blast and Impact Measurement, 21-Jun-2017.

APPENDIX A: SAMPLE PYTHON CODE

```
#Subtract data image from background image for 3 camera stations

import cv2
import os

#Bring in background files and normalize

background_file = "path_to_folder_containing_background_images"

files = os.listdir(background_file)

back_cam1l = cv2.imread(background_file + files[0],0)/255.
back_cam1u = cv2.imread(background_file + files[1],0)/255.
back_cam2l = cv2.imread(background_file + files[2],0)/255.
back_cam2u = cv2.imread(background_file + files[3],0)/255.
back_cam3l = cv2.imread(background_file + files[4],0)/255.
back_cam3u = cv2.imread(background_file + files[5],0)/255.

#Bring in data files and normalize

data_file = “path_to_folder_containing_data_images”

folder = os.listdir(data_file)
cam_1 = os.listdir(data_file + folder[0])
cam_2 = os.listdir(data_file + folder[1])
cam_3 = os.listdir(data_file + folder[2])

data_cam10l = cv2.imread(data_file + folder[0] + '/' + cam_1[0],0)/255.
data_cam10u = cv2.imread(data_file + folder[0] + '/' + cam_1[1],0)/255.
data_cam4l = cv2.imread(data_file + folder[1] + '/' + cam_2[0],0)/255.
data_cam4u = cv2.imread(data_file + folder[1] + '/' + cam_2[1],0)/255.
```

```
data_cam5l = cv2.imread(data_file + folder[2] + '/' + cam_3[0],0)/255.
data_cam5u = cv2.imread(data_file + folder[2] + '/' + cam_3[1],0)/255.

#Define Image Subtraction Equation
#data is the variable a, background is the variable b

def cam_dif(a,b):
image = ((a-b)*(a-b))/(((b+a)/2) +1)
image_working = image*255*256
return image_working

#Run Image Subtraction Equation

cam1l = cam_dif(data_cam4l,back_cam4l)
cam1u = cam_dif(data_cam4u,back_cam4u)
cam2l = cam_dif(data_cam5l,back_cam5l)
cam2u = cam_dif(data_cam5u,back_cam5u)
cam3l = cam_dif(data_cam6l,back_cam6l)
cam3u = cam_dif(data_cam6u,back_cam6u)

#Write subtracted images to a saved folder

cv2.imwrite(path_to_save_folder/Cam 1 Lower.png',cam1l)
cv2.imwrite(path_to_save_folder /Cam 1 Upper.png',cam1u)
cv2.imwrite(path_to_save_folder /Cam 2 Lower.png',cam2l)
cv2.imwrite(path_to_save_folder /Cam 2 Upper.png',cam2u)
cv2.imwrite(path_to_save_folder /Cam 3 Lower.png',cam3l)
cv2.imwrite(path_to_save_folder /Cam 3 Upper.png',cam3u)
```

APPENDIX B: IMAGES FROM TEST SERIES 1

Appendix B contains the raw images from each camera station in Test Series 1. Due to the large amount of data collected, only two tests are shown. The first set of four images show the 0.308 projectile for camera stations 1 and 2. The second set of four images show the Ultem plastic projectile for camera stations 1 and 2.

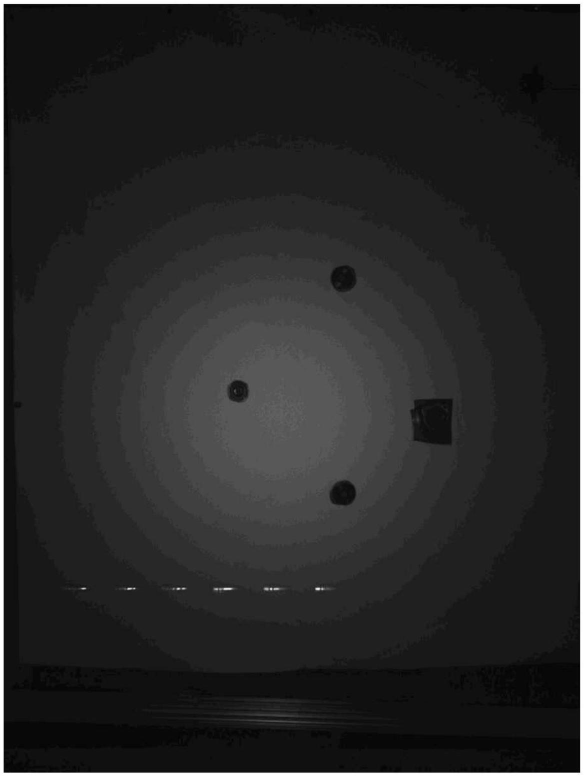

Figure 55: Test Series 1, Camera Station 1, Upper Camera, Copper 0.308 Projectile

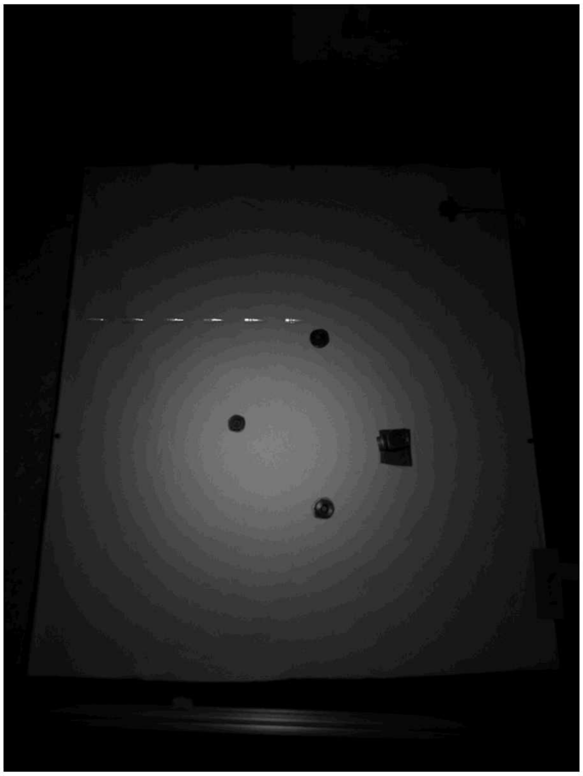

Figure 56: Test Series 1, Camera Station 1, Lower Camera, Copper 0.308 Projectile

Figure 57: Test Series 1, Camera Station 2, Upper Camera, Copper 0.308 Projectile

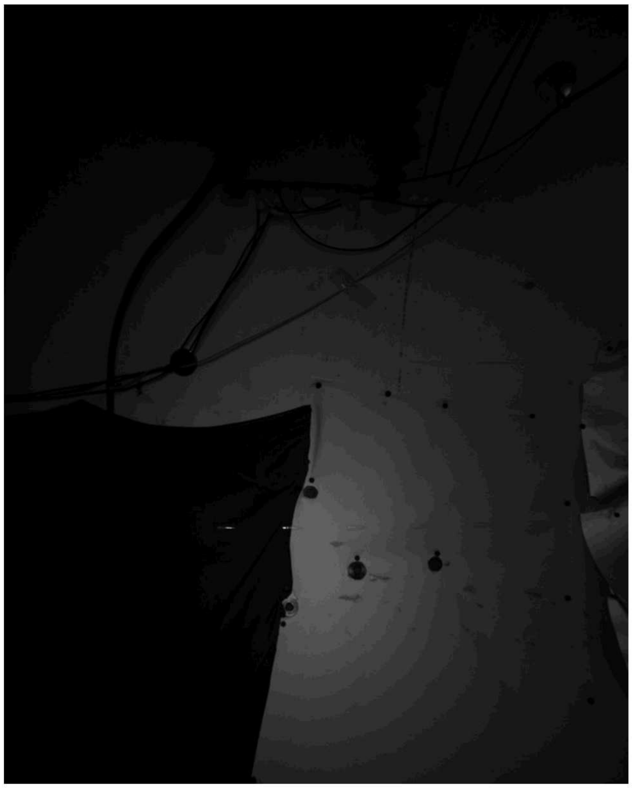

Figure 58: Test Series 1, Camera Station 2, Lower Camera, Copper 0.308 Projectile

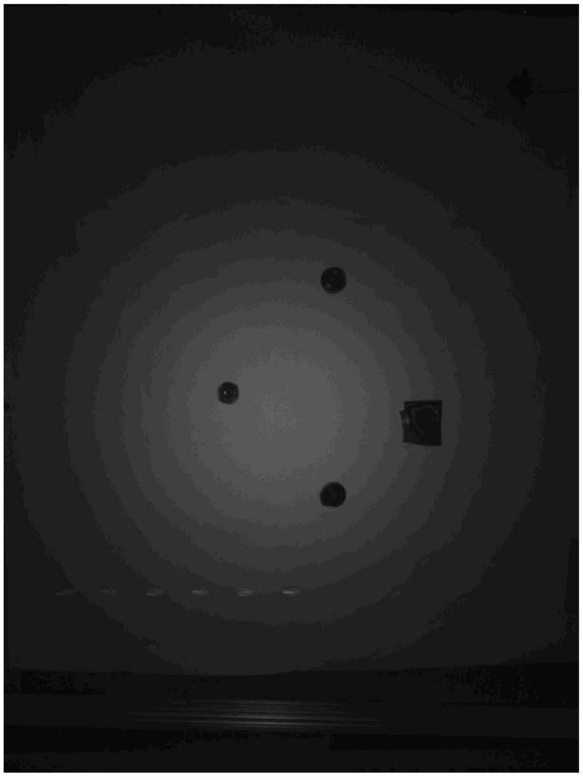

Figure 59: Test Series 1, Camera Station 1, Upper Camera, Ultem Projectile

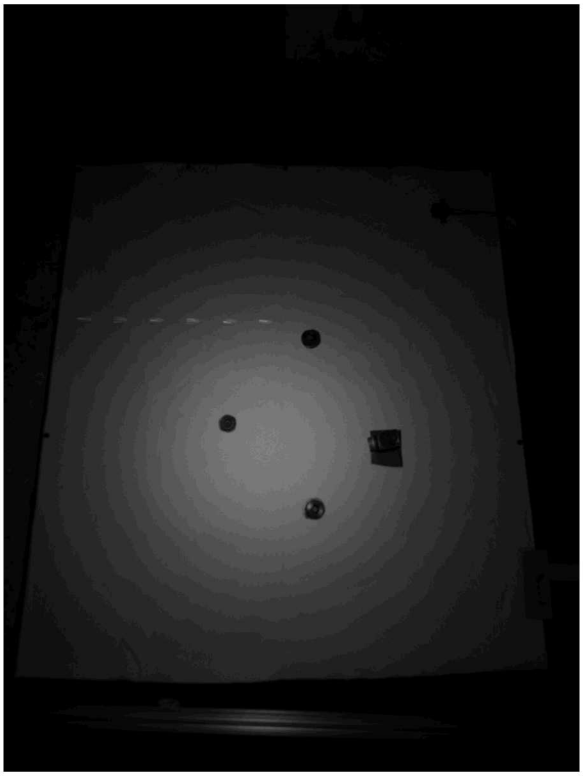

Figure 60: Test Series 1, Camera Station 1, Lower Camera, Ultem Projectile

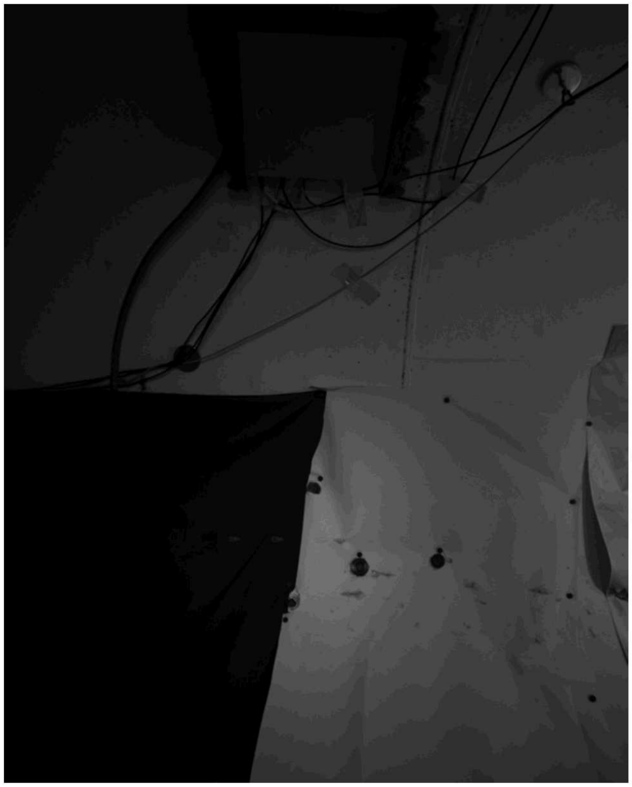

Figure 61: Test Series 2, Camera Station 1, Lower Camera, Ultem Projectile

Figure 62: Test Series 2, Camera Station 1, Upper Camera, Ultem Projectile

APPENDIX C: IMAGES FROM TEST SERIES 2

Appendix C contains the raw images from each camera station in Test Series 2. Due to the large amount of data collected, only two tests are shown. The first set of images was taken on test 29 which was a cylindrical wedge projectile. The second set of images was taken on test 33 which was a rectangular projectile. The images are grouped by camera station where the upper half of each figure is the upper camera’s FOV, and the lower half of the image is the lower camera’s FOV. The projectile was not seen in every image, but this was especially true for the camera stations using the Constellation 120E strobe light.

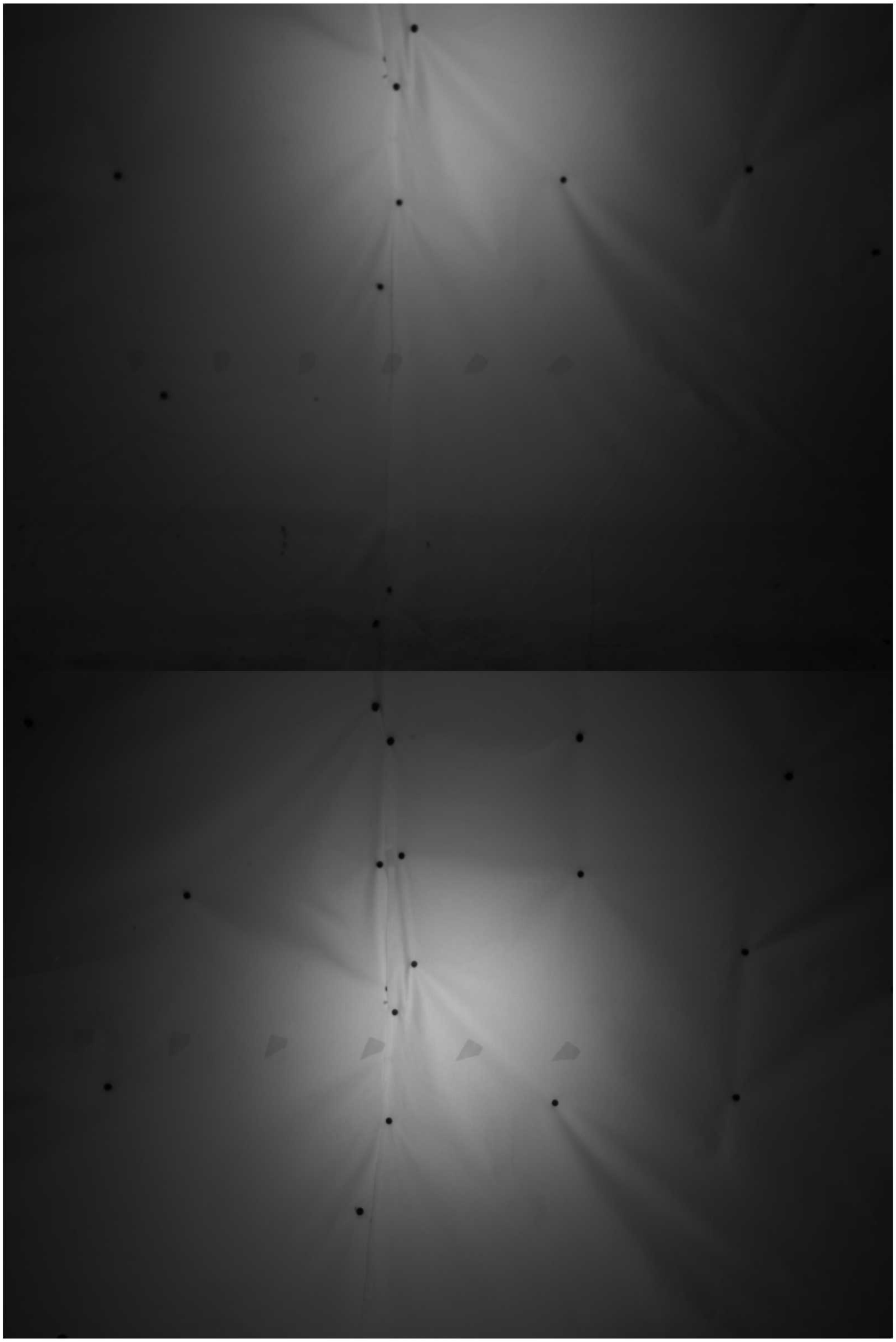

Figure 63: Shot 29, Cylindrical Wedge, Camera Station 1

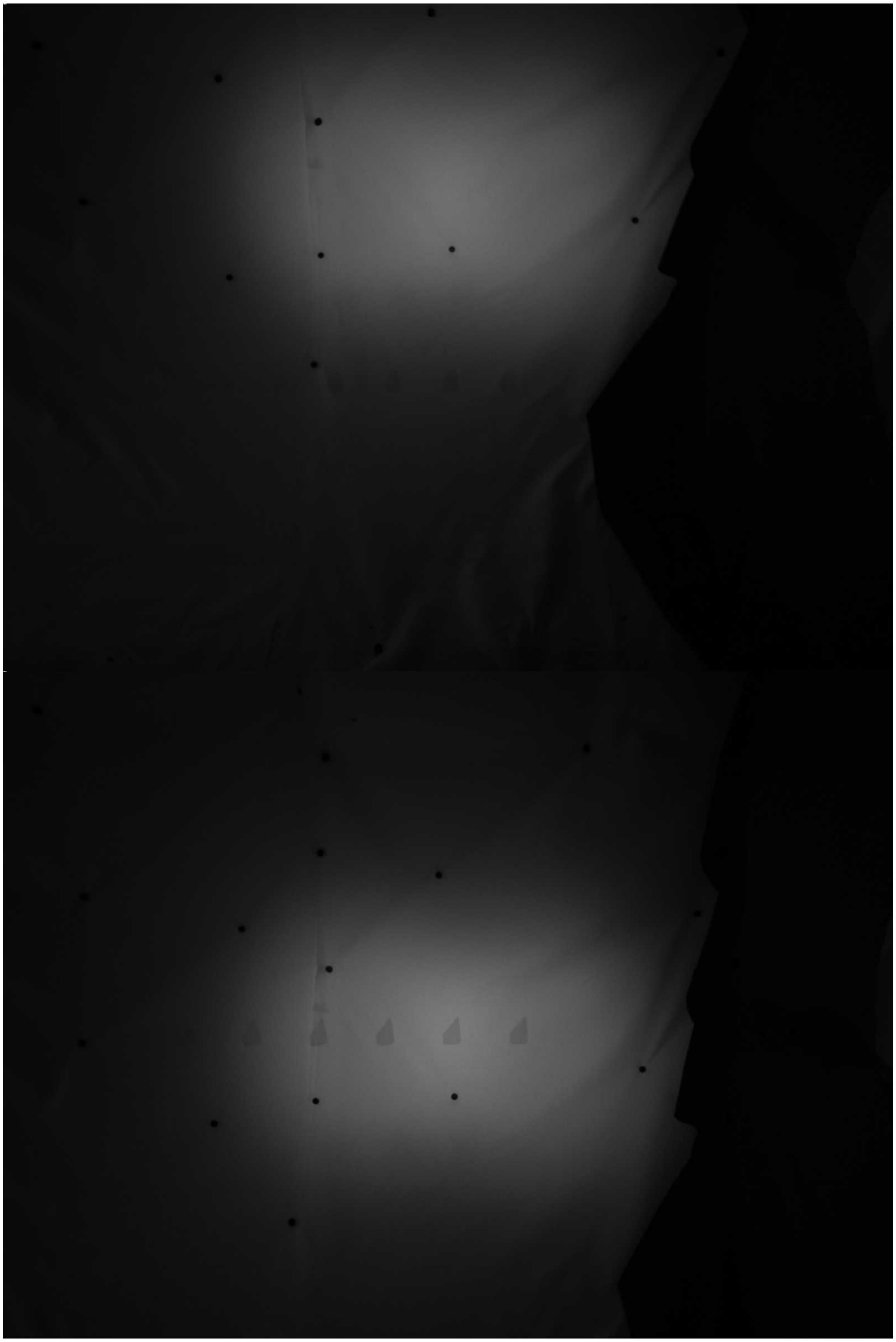

Figure 64: Shot 29, Cylindrical Wedge, Camera Station 2

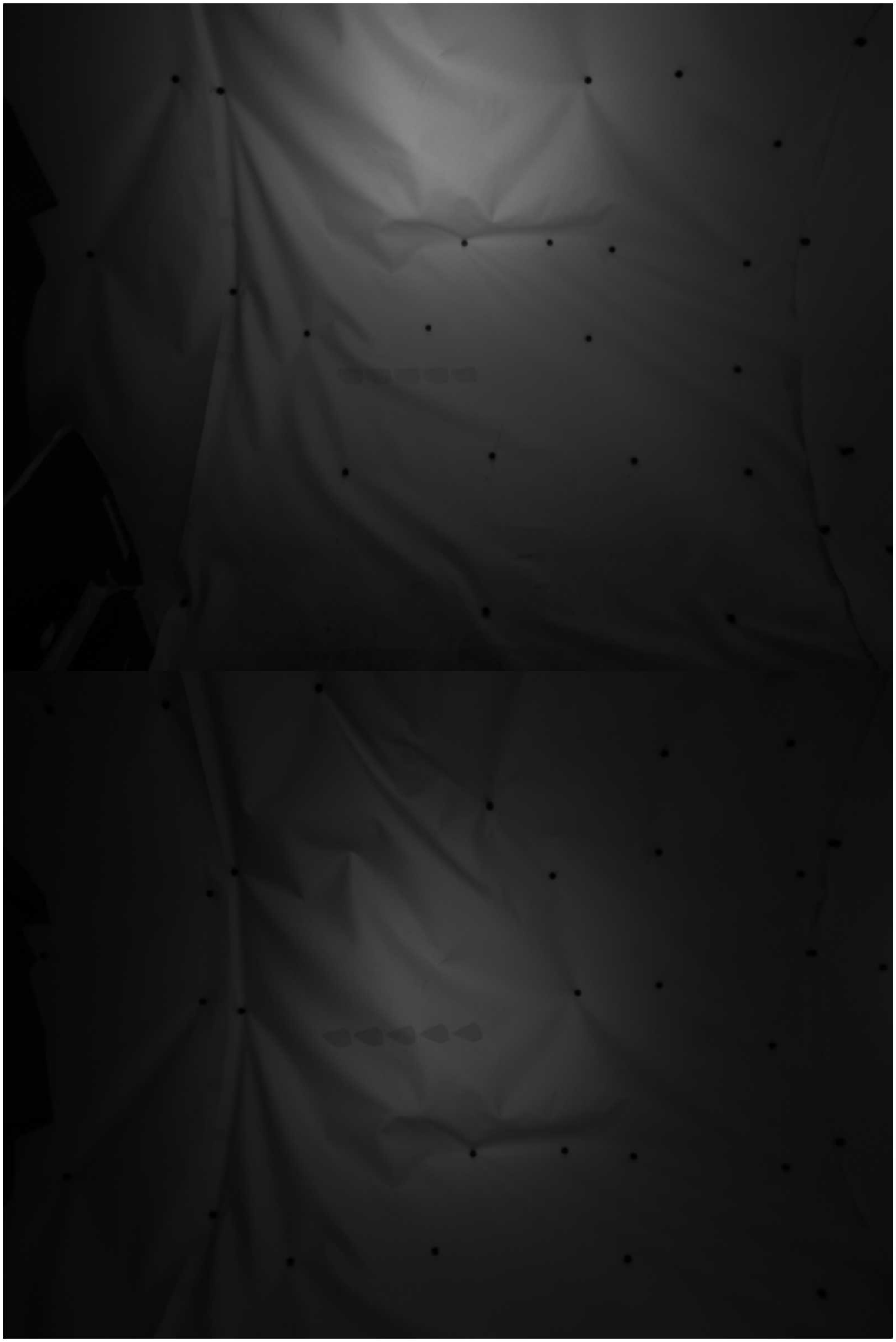

Figure 65: Shot 29, Cylindrical Wedge, Camera Station 3

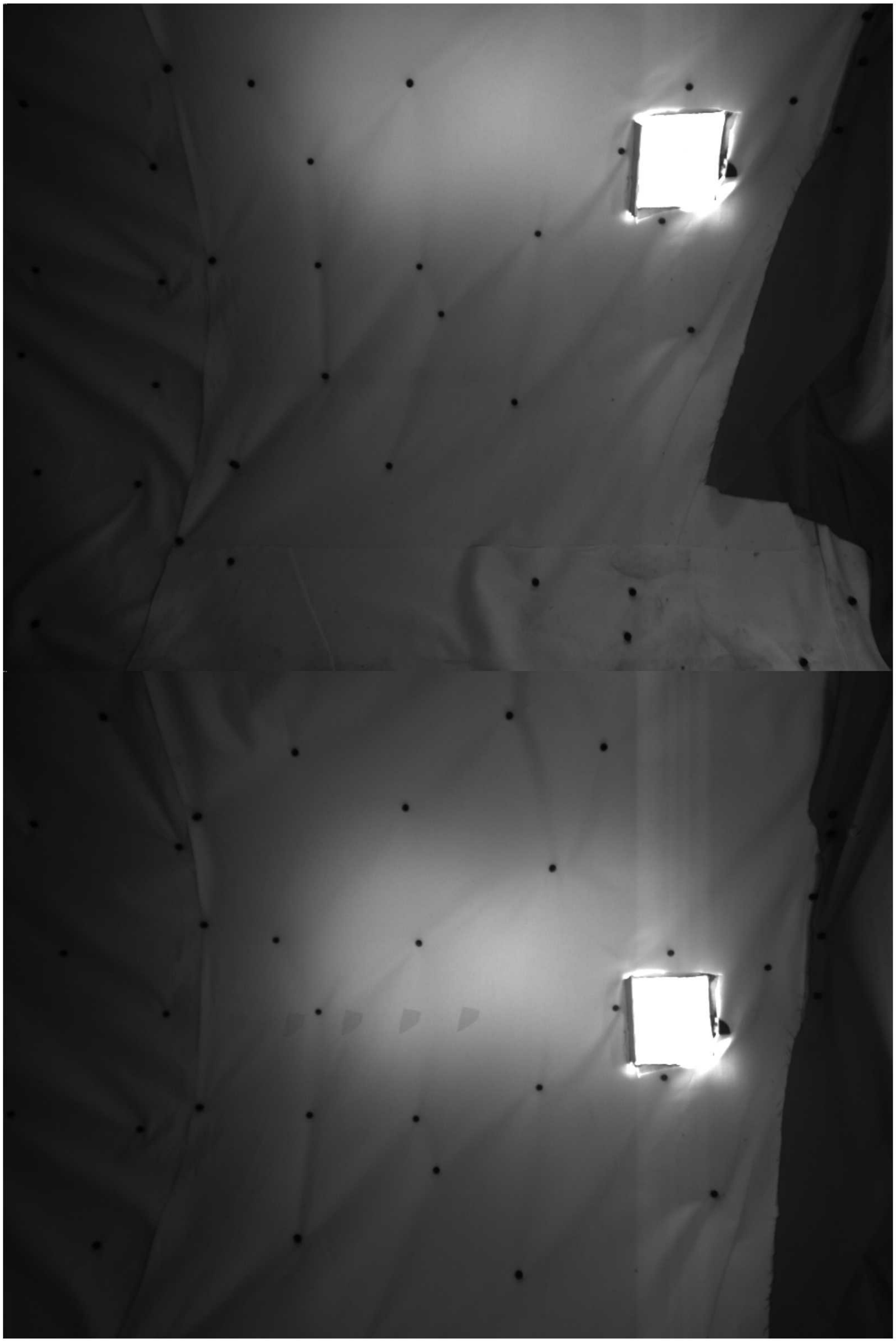

Figure 66: Shot 29, Cylindrical Wedge, Camera Station 4

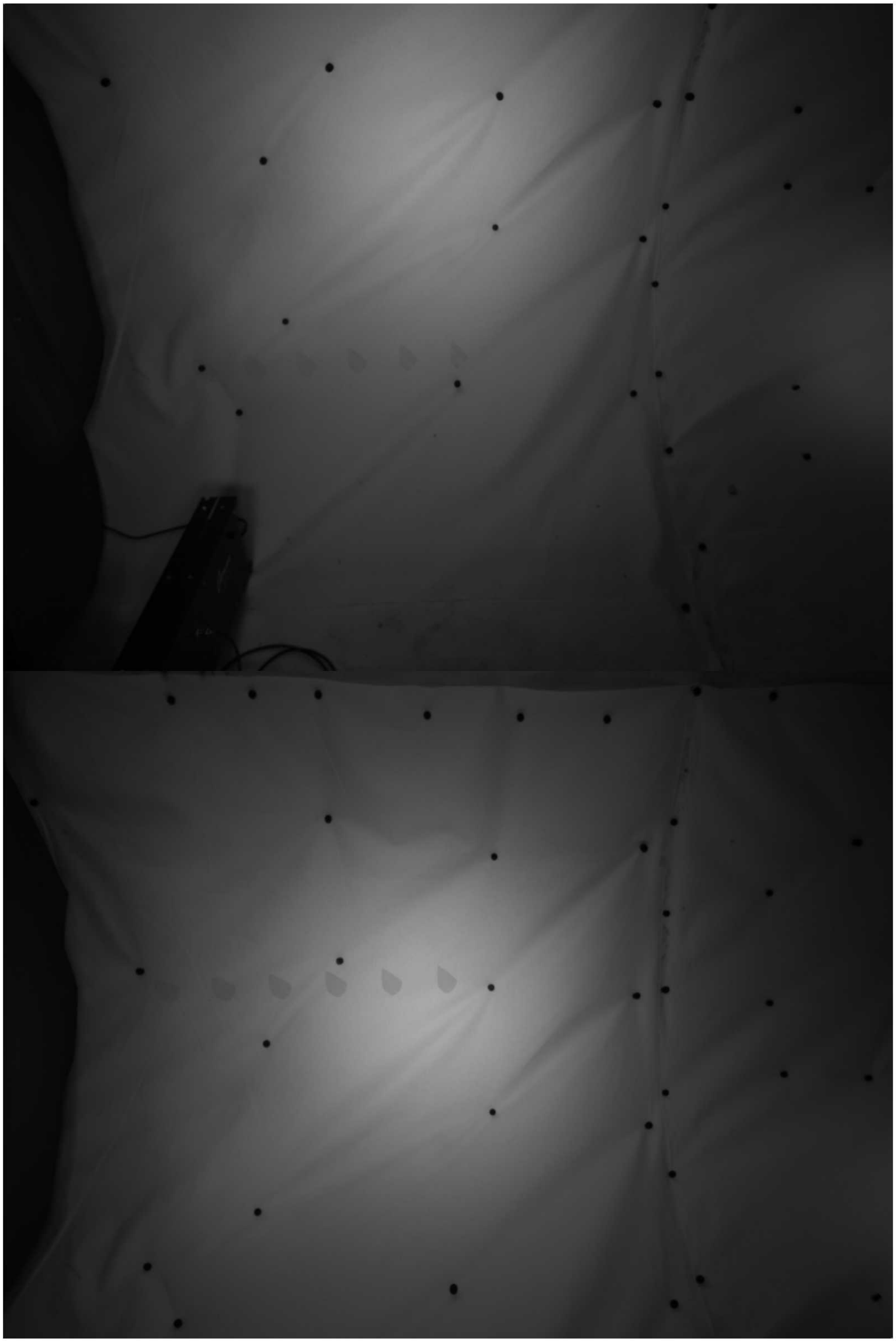

Figure 67: Shot 29, Cylindrical Wedge, Camera Station 5

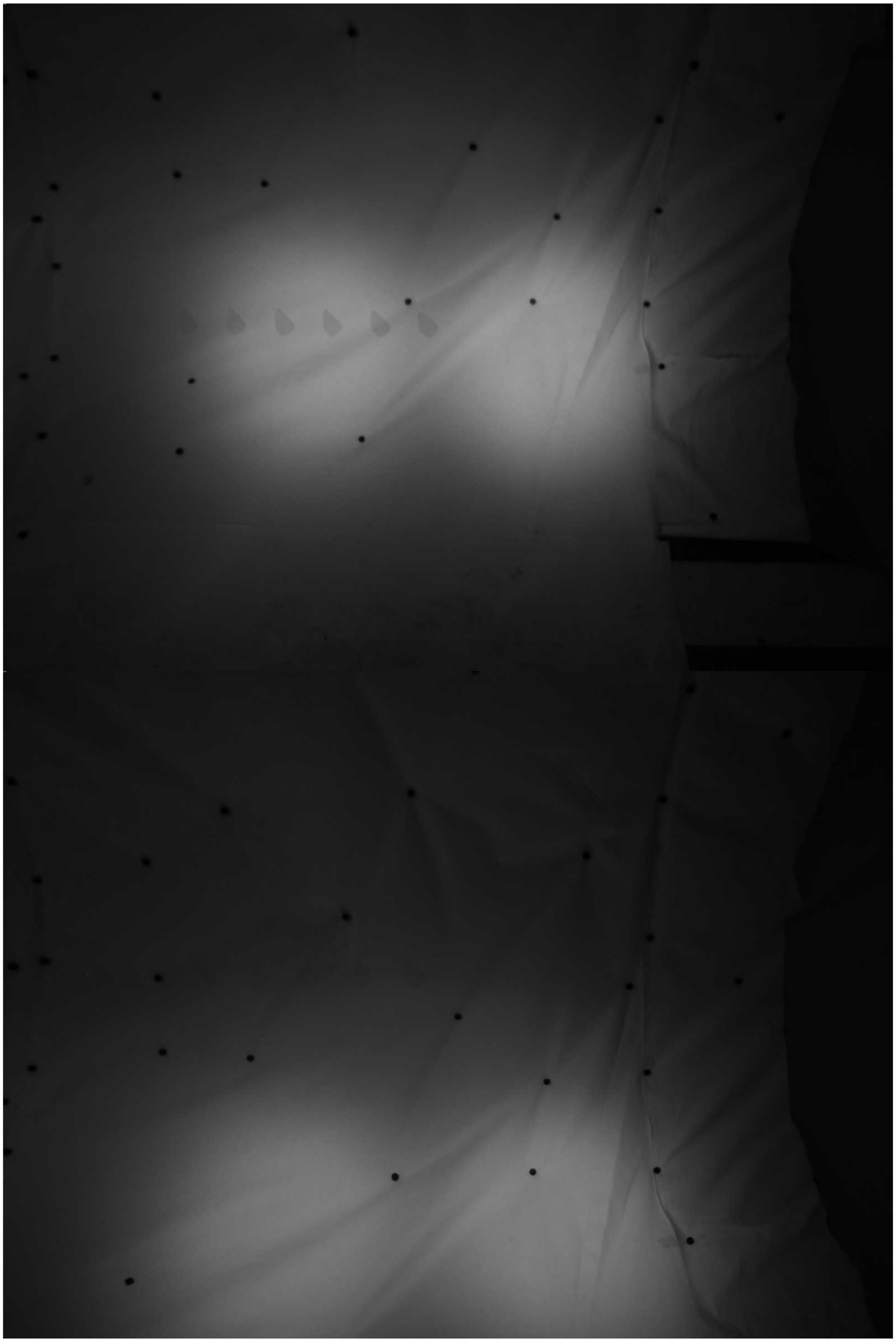

Figure 68: Shot 29, Cylindrical Wedge, Camera Station 6

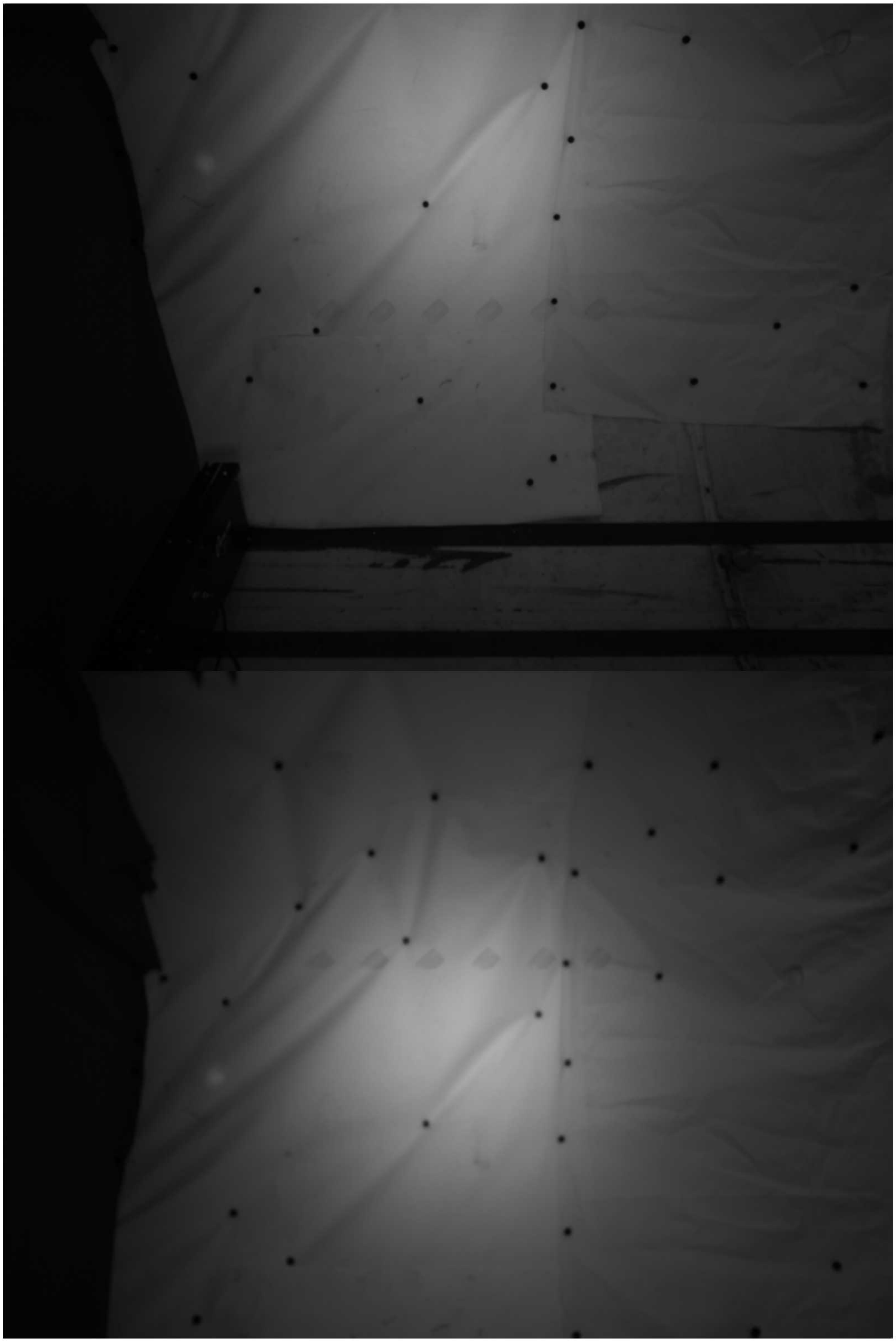

Figure 69: Shot 29, Cylindrical Wedge, Camera Station 7

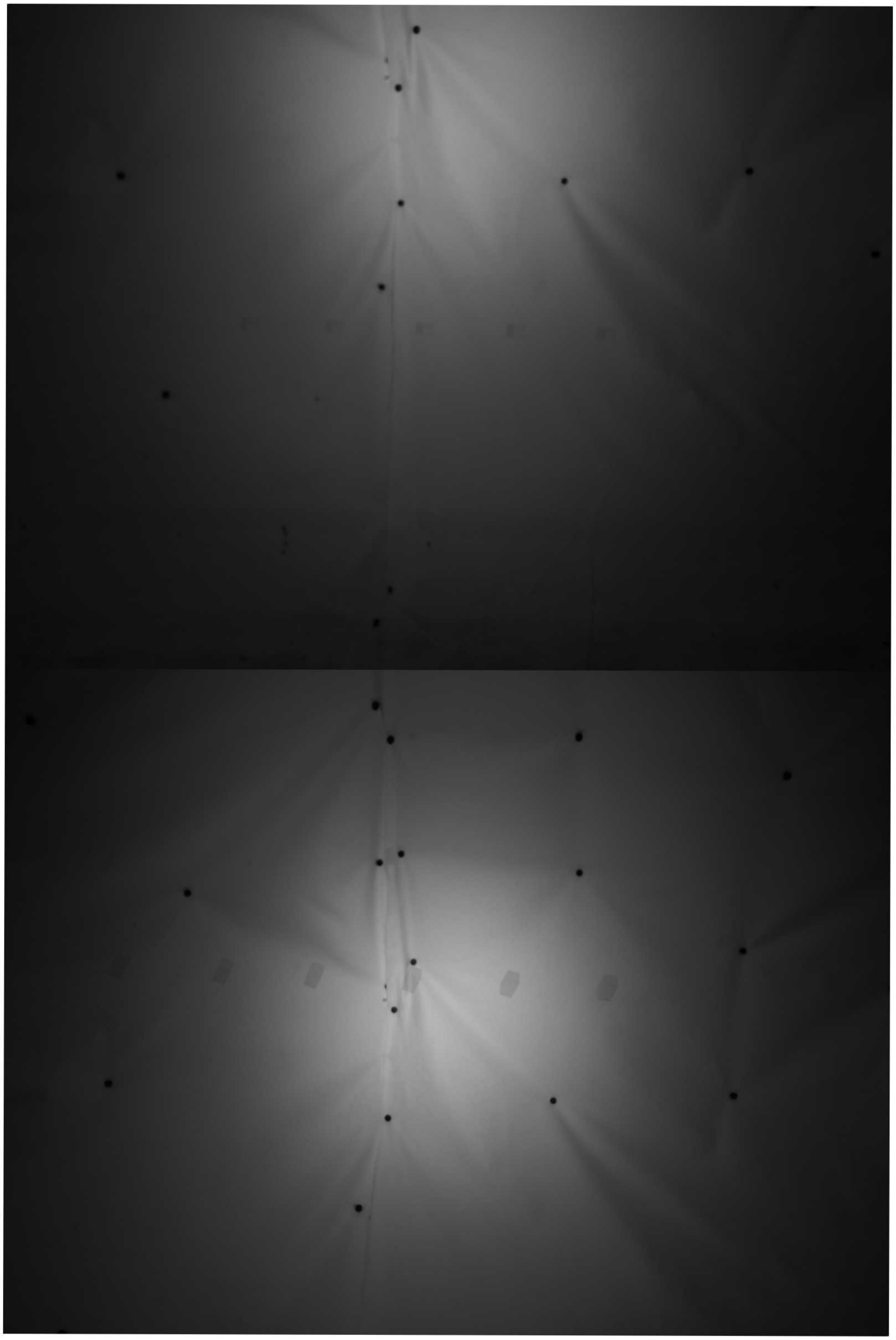

Figure 70: Shot 33, Rectangular Wedge, Camera Station 1

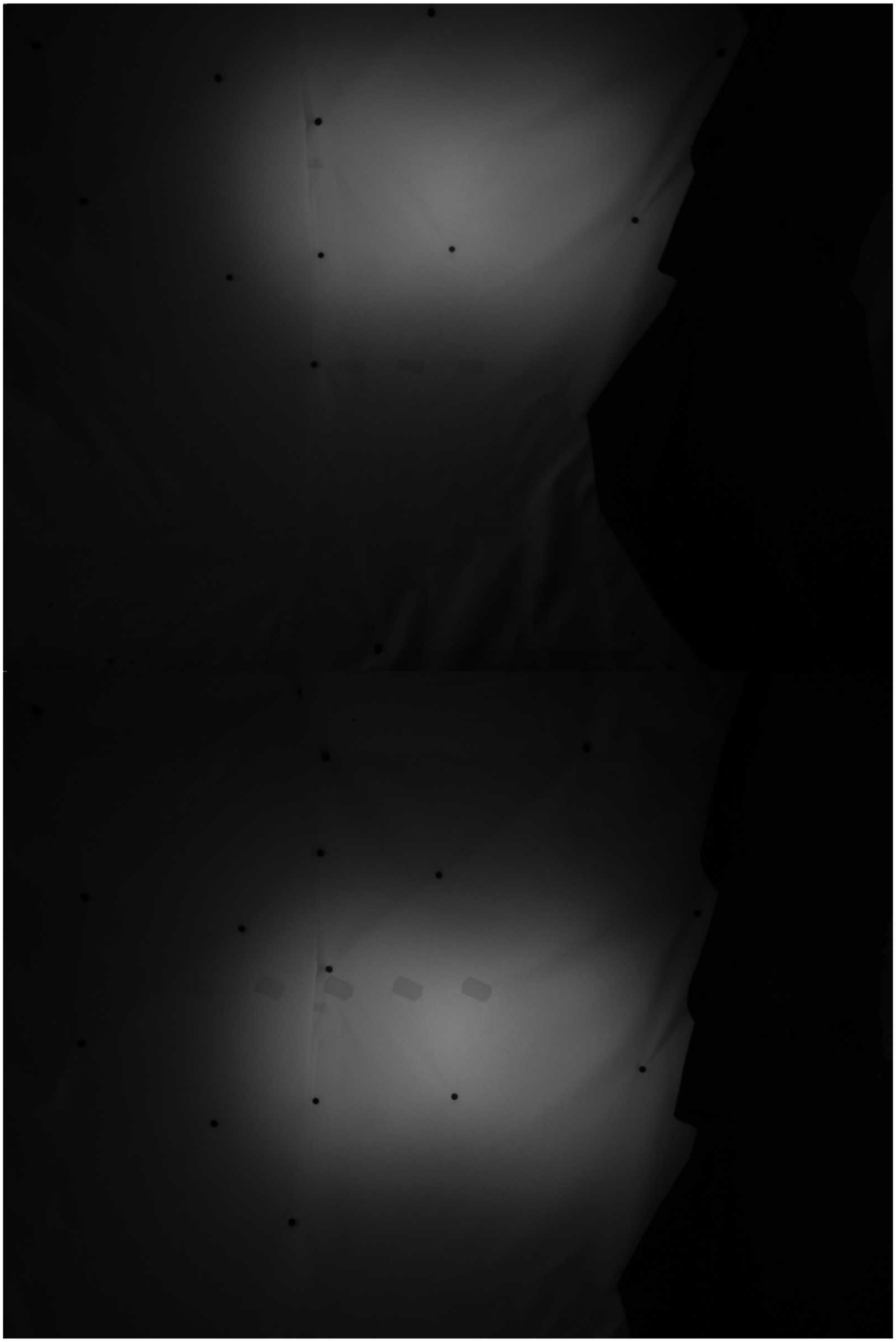

Figure 71: Shot 33, Rectangular Wedge, Camera Station 2

Figure 72: Shot 33, Rectangular Wedge, Camera Station 3

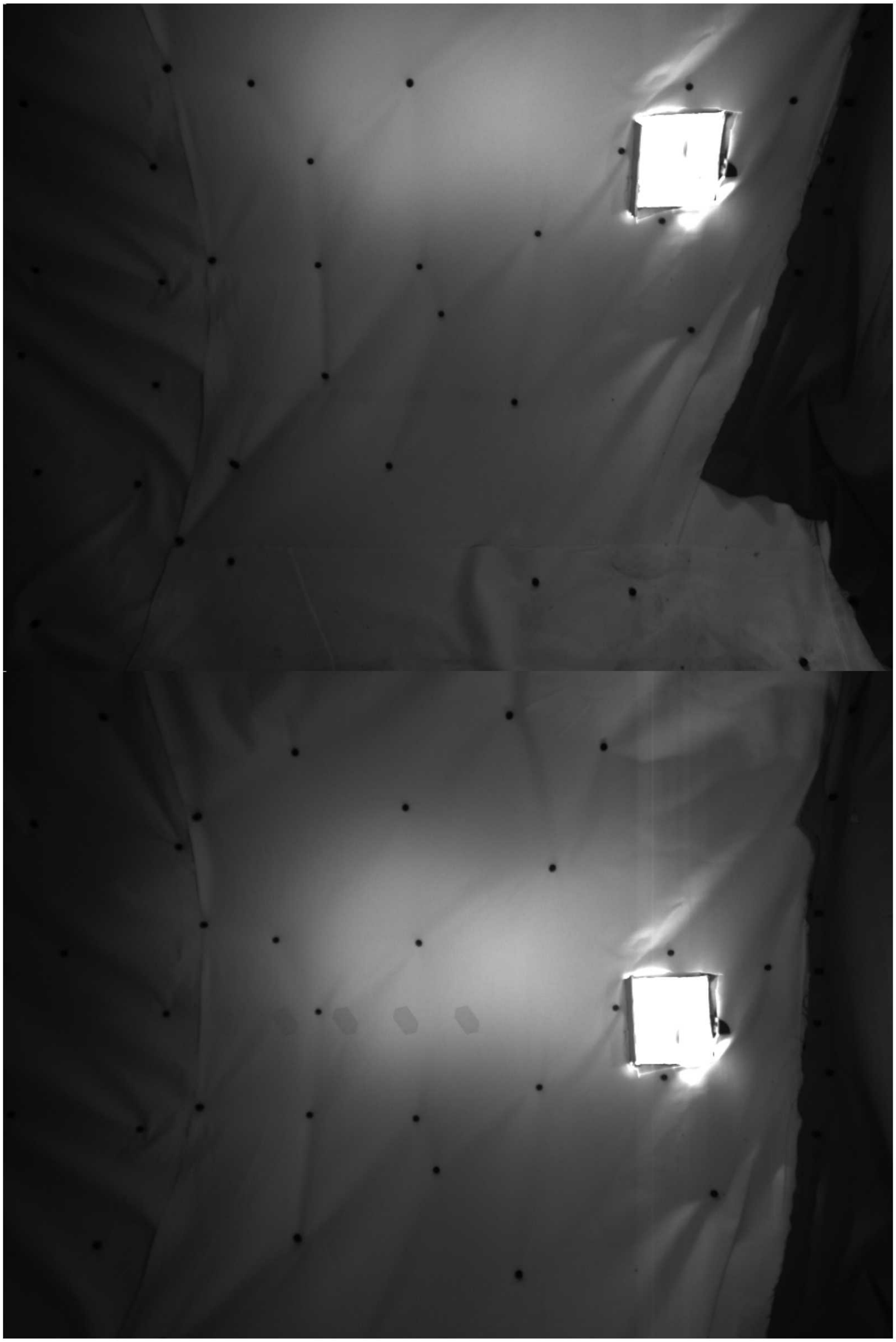

Figure 73: Shot 33, Rectangular Wedge, Camera Station 4

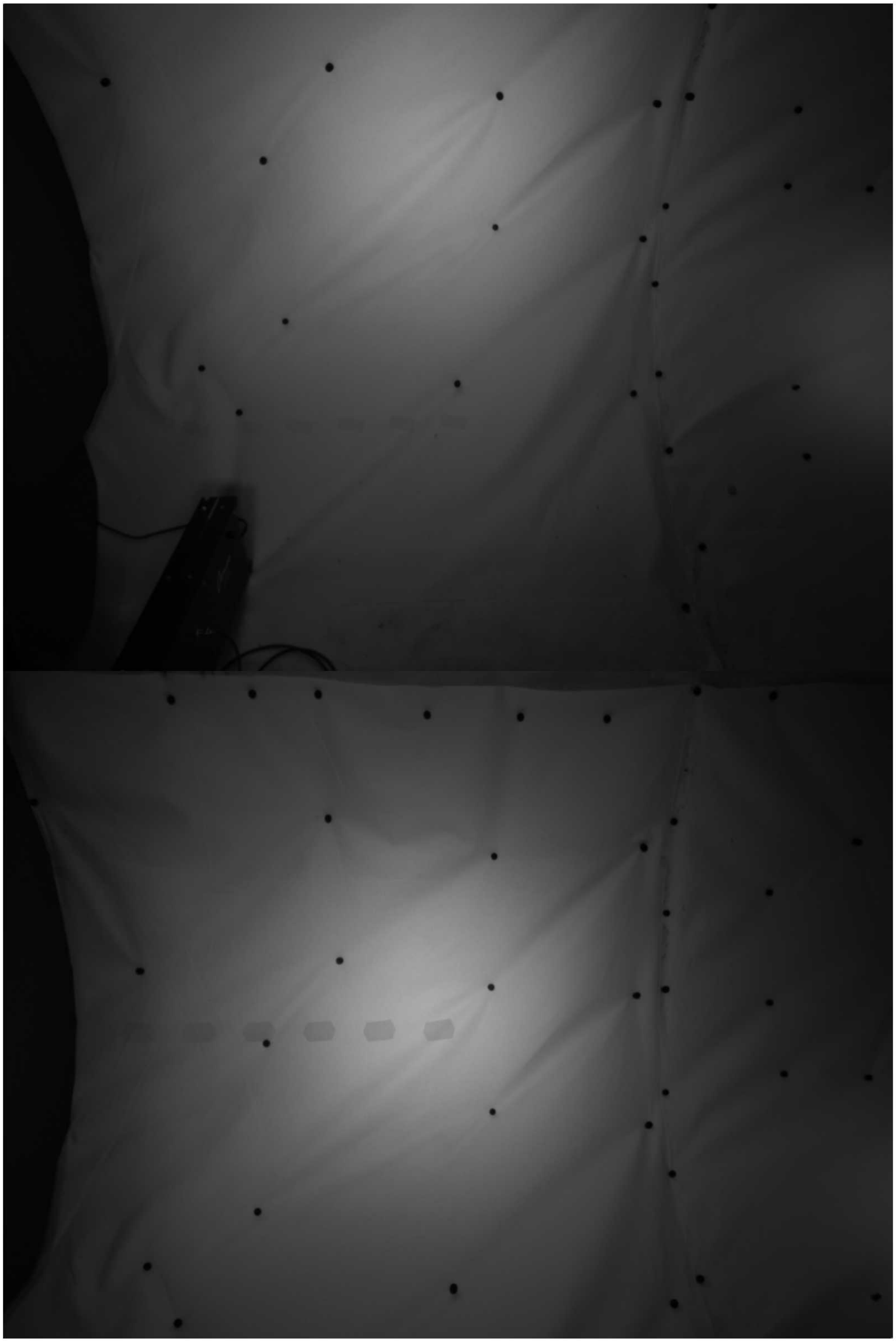

Figure 74: Shot 33, Rectangular Wedge, Camera Station 5

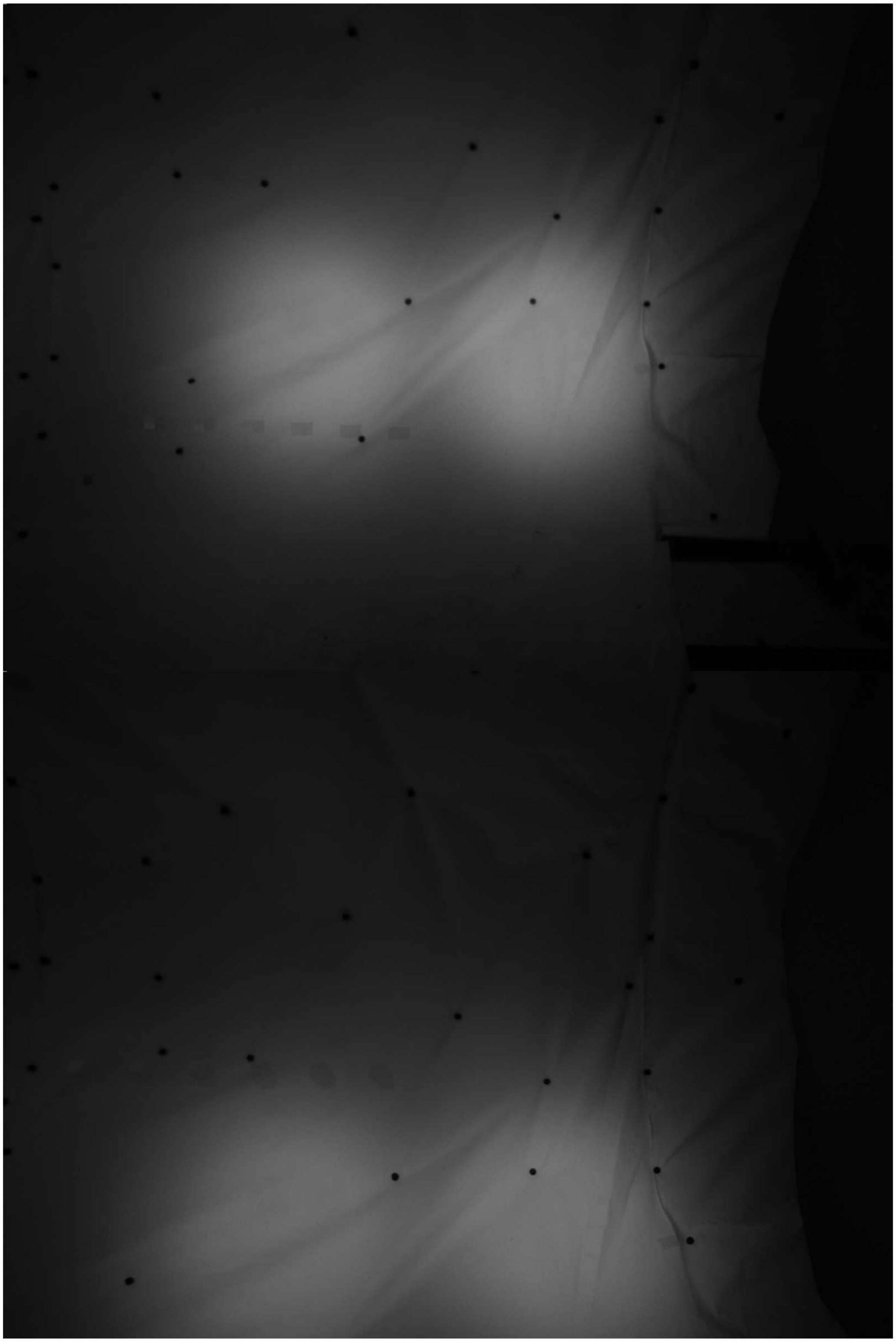

Figure 75: Shot 33, Rectangular Wedge, Camera Station 6

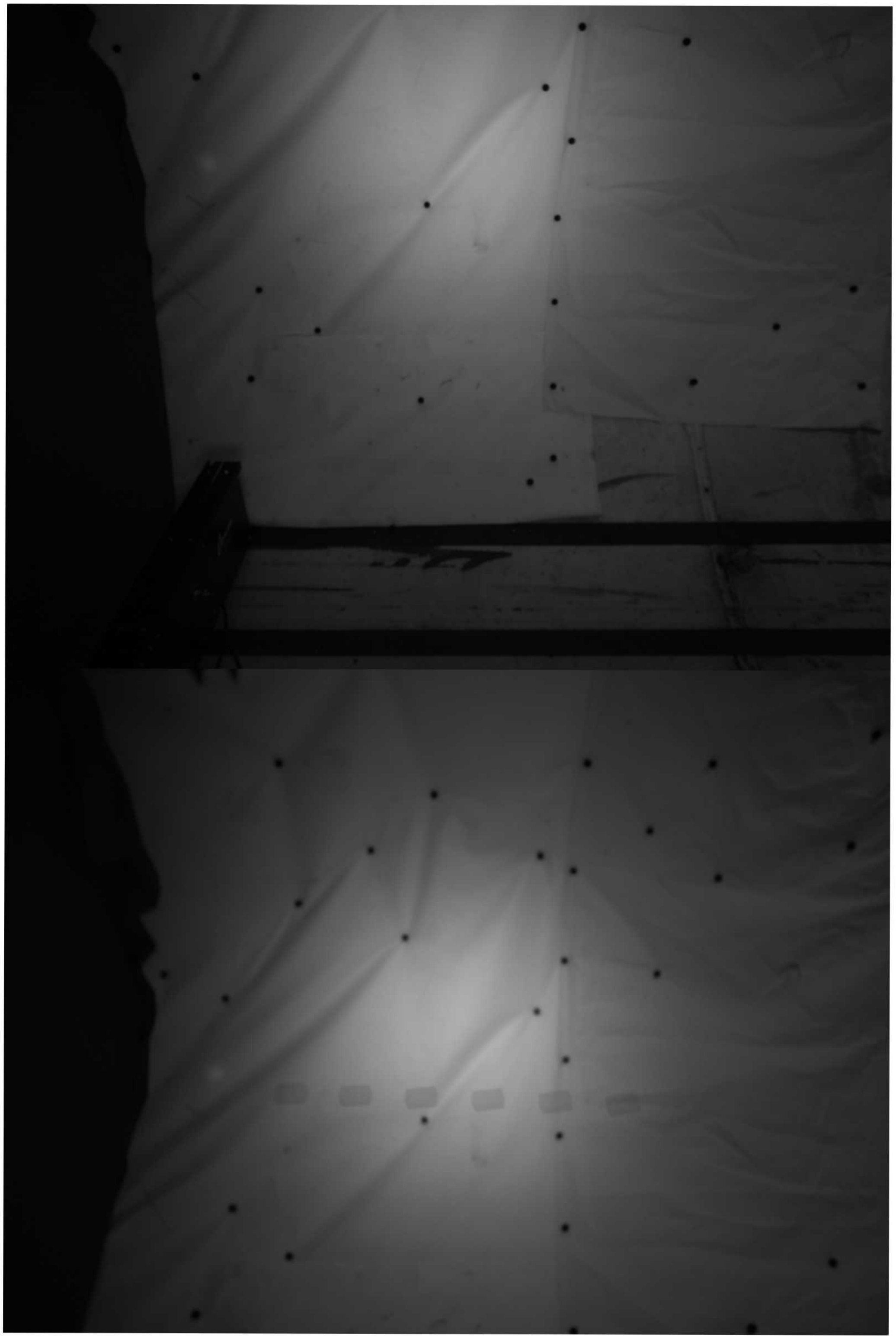

Figure 76: Shot 33, Rectangular Wedge, Camera Station 7

Three-Dimensional Tracking of High-Speed Tumbling Projectiles Using Stroboscopic Imaging

By Daniel James Bixler